



UNIVERSIDAD DE SEVILLA

*GRUPO DE ELASTICIDAD Y RESISTENCIA DE MATERIALES*

**Ph.D. Thesis**

# Modelling the compaction of composite materials with ultrasonic vibrations

Jesús Justo Estebaranz

Advisors:

Dr. Enrique Graciani Díaz  
Dr. Federico París Carballo  
Dr. Francisco Chinesta Soria

Sevilla. 2014



## *Acknowledgements*

I would like to express my gratitude to my advisors, Enrique Graciani, Federico París and Francisco Chinesta for their support throughout these years, their attention and all the opportunities they gave to me along this period, which have enabled my growth as a person and a researcher.

I would like to express my gratitude to all the people that work in the group for their kindness and for their help when it was necessary.

I would also like to thank my wife and my family for celebrating with me the success, for sharing with me the difficulties and for their patience and understanding.



# Contents

<b>List of figures</b>	<b>13</b>
<b>List of tables</b>	<b>19</b>
<b>Chapter 1: Introduction</b>	<b>21</b>
1.1 Manufacturing of composite materials.....	24
1.1.1 Pre-preg lay-up and autoclave curing .....	25
1.2 Out-of-autoclave manufacturing .....	28
1.2.1 Oven .....	29
1.2.2 Hot plates press .....	30
1.2.3 Quickstep.....	32
1.2.4 Hand lay-up.....	34
1.2.5 Filament winding .....	36
1.2.6 Liquid resin infusion (LRI) .....	38
1.2.7 High energy Electron-Beam.....	40
1.2.8 Low energy Electron-Beam .....	41
1.2.9 Pultrusion .....	43
1.2.10 Spray-up .....	45
1.2.11 Compression molding .....	46
1.2.12 Roll wrapping.....	47

1.2.13 Injection molding.....	48
1.3 Prototype under study .....	49
1.3.1 Parts of the prototype.....	49
1.3.2 Movements of the prototype.....	51
1.3.3 Ultrasonic compaction device.....	52
1.4 Scope of the Thesis .....	54
Bibliography .....	58
<b>Chapter 2: Previous analyses</b>	<b>61</b>
2.1 Compaction procedures .....	62
2.1.1 Compaction of one uncured ply.....	62
2.1.2 Compaction of multiple uncured plies.....	64
2.2 Experimental measurements .....	65
2.2.1 Measurement of the evolution of the temperature during a static compaction process .....	66
2.2.2 Measurement of the degree of cure to obtain the curing kinetics of the resin.....	67
2.2.3 Evolution of the viscosity with the temperature .....	72
Bibliography .....	73
<b>Chapter 3: Problems under study</b>	<b>75</b>
3.1 Transient problem.....	76

---

3.1.1 Geometry definition .....	77
3.1.2 Boundary conditions .....	78
3.1.3 Heats involved in the compaction process .....	78
3.2 Stationary problem .....	80
3.2.1 Geometry definition .....	80
3.2.2 Boundary conditions .....	81
3.2.3 Heats involved in the compaction process .....	82
3.3 Conclusions .....	83
Bibliography .....	83
<b>Chapter 4: Initial models</b> .....	<b>85</b>
4.1 Estimation of the temperature in the laminate .....	86
4.1.1 Description, hypotheses and implementation of the thermal model .....	87
4.1.2 Results .....	90
4.1.3 Experimental validation .....	92
4.2 Evaluation of the possible curing of the resin during the compaction process .....	93
4.2.1 Algorithm to calculate the degree of cure .....	93
4.2.2 Curing model .....	95
4.2.3 Results of the curing model .....	100
4.3 Modelling the evolution of the viscosity with the temperature .....	102

4.4 Conclusions.....	104
Bibliography .....	105
<b>Chapter 5: Modelling the heat generation</b>	<b>107</b>
5.1 Preliminary remarks.....	108
5.2 Hypotheses of the model.....	111
5.3 Boundary conditions .....	113
5.3.1 Vertical movement of the sonotrode.....	113
5.3.2 Horizontal movement of the sonotrode .....	114
5.4 Evaluation of the heat generated.....	115
5.4.1 Heat generated by the vertical movement of the sonotrode .....	116
5.4.2 Heat generated by the horizontal movement of the sonotrode .....	122
5.5 Conclusions.....	124
Bibliography .....	125
<b>Chapter 6: Semi-analytical model</b>	<b>127</b>
6.1 Alternatives in the pre-preg modelling .....	128
6.2 Heat generation modelling.....	130
6.3 Heat distribution modelling .....	131
6.4 Algorithm for solving the heat generation-distribution problem.....	133
6.5 Implementation of the algorithm in Matlab.....	135

---

6.6 Results .....	136
6.6.1 Results of the model.....	137
6.6.2 Comparison of the pre-preg models.....	139
6.6.3 Experimental comparison.....	141
6.7 Conclusions .....	142
Bibliography .....	144
<b>Chapter 7: 2D FEM model</b> .....	<b>145</b>
7.1 Heat generation and distribution modelling.....	146
7.2 Algorithm for solving the heat generation-distribution problem .....	147
7.3 Geometry and mesh.....	149
7.4 Results .....	151
7.5 Conclusions .....	156
Bibliography .....	157
<b>Chapter 8: PGD transient model</b> .....	<b>159</b>
8.1 Heat generation and distribution modelling.....	162
8.2 Algorithm for solving the heat generation-distribution problem .....	165
8.3 PGD formulation of the heat distribution in laminates for a transient problem .....	166
8.3.1 Computing $R(x)$ from $W(y)$ and $S(t)$ .....	170
8.3.2 Computing $W(y)$ from $R(x)$ and $S(t)$ .....	173

8.3.3 Computing $S(t)$ from $R(x)$ and $W(y)$ .....	175
8.4 Results.....	177
8.5 Model validation .....	184
8.6 Conclusions.....	186
Bibliography .....	187
<b>Chapter 9: PGD steady-state model</b>	<b>189</b>
9.1 Heat generation and distribution modelling.....	190
9.2 Algorithm for solving the heat generation-distribution problem.....	193
9.3 PGD formulation of the heat distribution in laminates for a transient problem.....	195
9.3.1 Computing $R(x)$ from $W(y)$ .....	198
9.3.2 Computing $W(y)$ from $R(x)$ .....	201
9.4 Results.....	203
9.5 Parametric study of the influence of the compaction parameters .....	208
9.5.1 Horizontal displacement velocity of the sonotrode .....	208
9.5.2 Amplitude of the ultrasonic vibration.....	209
9.5.3 Frequency of the ultrasonic vibration .....	210
9.5.4 Angle of the sonotrode.....	211
9.6 Conclusions.....	213
Bibliography .....	214

<b>Chapter 10: Conclusions and future developments</b>	<b>215</b>
10.1 Conclusions .....	216
10.2 Future developments .....	219
<b>Annex I</b>	<b>221</b>
<b>Annex II</b>	<b>225</b>
<b>Publications</b>	<b>227</b>



# List of figures

1.1. View of a vacuum bag.....	26
1.2. View of an autoclave.....	27
1.3. View of an oven .....	29
1.4. View of a hot plates press .....	31
1.5. View of a Quickstep machine .....	33
1.6. View of a stage of the hand lay-up process.....	35
1.7. View of a filament winding machine .....	37
1.8. Sketch of the LRI processes .....	40
1.9. View of a high energy electron-beam machine.....	41
1.10. Draft of a low energy electron-beam system .....	43
1.11. View of a pultrusion machine .....	44
1.12. View of a spray-up system.....	45
1.13. View of a compression moulding machine .....	46
1.14. View of a the roll wrapping technique .....	48
1.15. View of an injection molding machine .....	49
1.16. View of the prototype under study.....	51
1.17. Possible movements of the prototype.....	52
1.18. View of the ultrasonic compaction device .....	53
1.19. Scheme of the materials located under the sonotrode.....	54

2.1. Schematic view of the typical situation encountered when compaction and curing is carried out ply by ply .....	63
2.2. Schematic view of the typical situation encountered when compaction of the whole laminate is carried out before curing .....	64
2.3. Experimental temperature/time curve at the bottom of the laminate during the ultrasonic compaction process.....	67
2.4. Heat flux/temperature diagram of a resin, obtained with the DSC.....	69
2.5. Absorbance spectrum of a resin, measured with the FTIR.....	71
2.6. Evolution of the viscosity with the time for several values of the heating rates .....	73
3.1. Scheme of the problem for the thermal model .....	77
3.2. Scheme of the problem for the thermal model .....	80
4.1. FEM thermal model .....	87
4.2. Detailed view of the contact zone between the sonotrode and the laminate.....	89
4.3. Temperature evolution imposed to the sonotrode tip to evaluate the temperature field in the thermal model.....	90
4.4. Temperature vs time curve, obtained with the thermal model for a static compaction, at a node situated at $(x=0, y=0)$ .....	91
4.5. Temperature field inside the laminate during the static ultrasonic compaction process (in Kelvin) .....	92
4.6. Comparison of the thermal FEM model results with experimental measurements .....	92

---

4.7. Scheme of the algorithm used to estimate the degree of cure during the compaction process .....	95
4.8. Curve to relate the measurements of the FTIR (horizontal axis) and the DSC (vertical axis).....	96
4.9. Representations of the cure kinetics as degree of cure/variation of the degree of cure with the time for several values of the temperature .....	98
4.10. 3D representation of the cure kinetics.....	99
4.11. Model of the curing kinetics from 0° to 200 °C .....	100
4.12. Time vs Degree of cure curve, obtained with the curing kinetic model for a static compaction process during 10 seconds.....	101
4.13. Approximation of the evolution of the viscosity with the temperature for low temperatures and high temperature rates.....	103
5.1. Scheme of a pre-preg ply .....	109
5.2. Thicknesses in a pre-preg ply.....	109
5.3. Hagen-Poiseuille horizontal velocity profile of the resin originated by the vertical movement of the sonotrode in the $i^{\text{th}}$ -resin layer.....	110
5.4. Couette horizontal velocity profile of the resin originated by the horizontal movement of the sonotrode in the $i^{\text{th}}$ -resin layer .....	111
5.5. Balance of flow rate in a control volume .....	117
5.6. Balance at the $i^{\text{th}}$ layer .....	121
6.1. First hypothesis considered for the pre-preg modelling.....	129
6.2. Second hypothesis considered for the pre-preg modelling .....	129
6.3. Scheme of the resin layers for the 1D model .....	136

6.4. Evolution of the temperature with the time at the bottom layer in the 1D semi-analytical model .....	137
6.5. Evolution of the heat generated during the compaction process in one layer, presented dimensionless .....	138
6.6. Enlarged view of the evolution of the heat generated during the compaction process in one layer, presented dimensionless, from 7 to 10 seconds of the process .....	139
6.7. Evolution of the temperature with the time at the bottom layer in the 1D semi-analytical model .....	140
6.8. Evolution of the temperature with the time at the bottom layer in the 1D semi-analytical model .....	141
6.9. Comparison between the time/temperature experimental and semi-analytical curves .....	142
7.1. View of the mesh used for the laminate and the sonotrode in the 2D FEM resolution of the compaction problem.....	149
7.2. Detail of the mesh used for the laminate and the sonotrode in the 2D FEM resolution of the compaction problem.....	150
7.3. Evolution of the temperature with the time at the middle of the bottom layer in the 2D FEM model for several number of elements along the x direction under the sonotrode .....	152
7.4. Evolution of the temperature with the time at the middle of the bottom layer in the 2D FEM model for several values of the time increment limit.....	153
7.5. Enlarged view of the evolution of the temperature with the time at the middle of the bottom layer in the 2D FEM model for several values of the time increment limit.....	154
7.6. Enlarged view of the evolution of the temperature with the time when using the time increment limit presented in.....	154

---

7.7. Comparison of experimental and numerical 2D FEM temperature/time curve at the bottom of the laminate for a long process time .....	155
7.8. Comparison of experimental and numerical 2D FEM temperature/time curve at the bottom of the laminate for a short process time .....	156
8.1. Evolution of the temperature along the $x$ axis for $t=1.5$ seconds and $y=0$ , from $M=1$ to $M=24$ .....	178
8.2. Enlarged view of the evolution of the temperature along the $x$ axis for $t=1.5$ seconds and $y=0$ , from $M=3$ to $M=24$ .....	179
8.3. Evolution of the temperature along the $y$ axis for $t=1.5$ seconds and $x=0$ , from $M=1$ to $M=24$ .....	180
8.4. Enlarged view of the evolution of the temperature along the $y$ axis for $t=1.5$ seconds and $x=0$ , from $M=3$ to $M=24$ .....	181
8.5. Evolution of the temperature along the time axis for $x=0$ and $y=0$ , from $M=1$ to $M=24$ .....	181
8.6. Enlarged view of the evolution of the temperature along the time axis for $x=0$ and $y=0$ , from $M=1$ to $M=24$ .....	182
8.7. 3D View of the temperature distribution inside the laminate during compaction process ( $t=1.5$ seconds) .....	183
8.8. Evolution of the temperature along time during the compaction process at ( $x=0$ , $y=0$ ) .....	184
8.9. Comparison of experimental and numerical temperature/time curve at the bottom of the laminate.....	185
9.1. Evolution of the temperature along the $x$ axis for $y=0$ , from $M=1$ to $M=11$ .....	204

9.2. Extended view of the evolution of the temperature along the $x$ axis for $y=0$ , from $M=1$ to $M=11$ .....	205
9.3. Evolution of the temperature along the $y$ axis at $x = L_c - \frac{1}{2}L_s$ from $M=1$ to $M=11$ .....	206
9.4. Enlarged view of the evolution of the temperature along the $y$ axis at $x = L_c - \frac{1}{2}L_s$ from $M=1$ to $M=11$ .....	207
9.5. Temperature field inside the laminate during a pass of the sonotrode .....	207
9.6. Evolution of the temperature inside the laminate along the $x$ axis at $y=0$ during a pass of the sonotrode for several velocities .....	209
9.7. Evolution of the temperature inside the laminate along the $x$ axis at $y=0$ during a pass of the sonotrode for several amplitudes of the vibration.....	210
9.8. Evolution of the temperature inside the laminate along the $x$ axis at $y=0$ during a pass of the sonotrode for several frequencies of the vibration.....	211
9.9. Angle of the sonotrode.....	212
9.10. Evolution of the temperature inside the laminate along the $x$ axis at $y=0$ for several angles of the sonotrode.....	212
AI.1. Evolution of the $X_l(x)$ functions along the $x$ axis .....	222
AI.2. Evolution of the $Y_l(y)$ functions along the $y$ axis .....	222
AI.3. Evolution of the $\Theta_l(t)$ functions along the $t$ axis.....	223
AII.1. Evolution of the $X_l(x)$ functions along the $x$ axis.....	226
AII.2. Evolution of the $Y_l(y)$ functions along the $y$ axis.....	226

# List of tables

1.1. Comparison between several mechanical properties obtained with the Quickstep methods and the autoclave .....	34
2.1. Equations of the curing model obtained from the experiments .....	72
4.1. Thermal properties of the materials .....	89
4.2. Equations of the curing model in terms of $\alpha$ .....	97



# *Chapter 1*

## *Introduction*

The manufacturing of composite laminates needs two basic processes: one in which the raw material is stacked following a certain sequence (giving the fibres an adequate orientation) and other in which the resin that conforms the matrix of the composite is polymerized.

The polymerization reaction consists on the generation of bonds between the monomers of the resin (in the case of thermoset resins) to form chains and in the crossing of these chains to form solid structures. For this reaction to occur, in principle, only a heat supply is necessary. However, if only an increase in

temperature is provided during the curing, the plies will not be well compacted (i.e. no air trapped in the laminate is removed) and the final part will present defects. To help to achieve the desired compaction and final shape of the part during curing, pressure and/or vacuum are typically applied during manufacturing.

The autoclave is the most used composite manufacturing system in the production of many components in aeronautical and aerospace industry, but it is typically the bottleneck of the process, because of its long processing times and elevated costs. Thus, manufacturing techniques that do not require the use of the autoclave while maintaining the excellent mechanical properties of the product are sought.

This work is framed in the E-BEAM project, developed by AIRBUS. In this project, an out-of-autoclave manufacturing system is being developed. The system has to be able to lay-up, compact and cure a laminate automatically and layer-by-layer, i.e., in a first step each layer is placed, compacted and partially cured and, in a second step, the layer is completely cured, when the next layer is placed, compacted and partially cured. In this way, the equipment would be able to manufacture composite parts at a low price, without the use of almost any auxiliary material, automatically and in a short time (at least, compared with the autoclave processing). Three main systems conform the prototype: an automatic tape lay-up head (its function is the placement of the pre-preg tape), an ultrasonic compaction device (its function is the in-line compaction of the layers), and a radiation-curing device (its function is the curing of the resin of the laminate). The first system is very common in the industry and its functioning is well known. In the case of the curing device, a low energy electron-beam has been tried, this technology still being very immature. The compaction system which is now being investigated constitutes the focus of this work.

To achieve a good quality in the final parts, the compaction phase subsequent to the placement of the composite plies, and previous to the curing phase, is needed, in order to substitute the vacuum bag used in the autoclave

manufacturing. To solve the problem of the compaction just after the composite ply is placed, an ultrasonic compactor has been implemented in the prototype. The ultrasonic compactor consists of a metallic horn connected to a pressure cylinder that generates an ultrasonic vibration movement in it. When the compactor is placed over the composite layers, it transmits the vibration to the preimpregnated layers, generating heat inside the laminate. This heat contributes to the compaction and debulking of the layers liquefying the resin and letting the air bubbles to escape outside. The evolution of the temperature inside the laminate is a very important parameter in order to understand and optimize the compaction process. To obtain this evolution, the heat generated inside the resin has to be known. The main parameters that can be modified on the compaction device are the amplitude of the vibration of the sonotrode and the horizontal velocity of the table where the laminate is placed.

In this chapter, in order to frame the prototype that is being developed, the description of the most common composite materials manufacturing processes will be done first. In Section 1.1, the autoclave, as the most used manufacturing system, will be explained in depth. Then, in Section 1.2 several out-of-autoclave manufacturing systems will be presented.

In Section 1.3, the prototype that is under study in the E-BEAM project will be commented. The subsystems that conform the prototype will also be described. Then, the possible movements of the prototype, which describe the possible laminates it can manufacture, will be shown. Finally, the ultrasonic compaction device and its functioning will be detailed.

At the end of this chapter, in Section 1.4, the scope of this Thesis and the chapters that form this Thesis will be explained.

## 1.1. Manufacturing of composite materials

The following descriptions are only related with the manufacturing of thermoset resins. In the case of the thermoplastic resins, other procedures are used.

As mentioned before, the manufacturing of composite materials requires several main phases to obtain the final solid part from the raw material. These main phases are:

- The preparation of the raw material in order to later obtain certain properties and a certain shape. It entails the cutting of the material following designated patterns.
- The placement of the material over a mould to obtain the desired shape. The lay-up of the plies can be done manually, automatically, injecting the raw material in a mould,...
- The application of pressure to compact the material that will be manufactured. This pressure can be applied mechanically to the material, through the contraction of a material that surrounds the laminate, applying pressure to a fluid that surrounds the laminate,...
- The polymerization of the resin. Depending on the resin, it can be done applying heat to the mold or to the air that surrounds the laminate, impacting the laminate with electrons,...

Depending on the implementation of conditions of temperature, pressure, vacuum and/or the raw material used, several systems of manufacturing composites have been obtained. The pre-preg lay-up and autoclave curing of laminates is the most common manufacturing system of composite materials in the industry and will be described next. Then, in next section, several out-of-autoclave manufacturing systems are discussed and compared qualitatively with the autoclave (in systems

where comparable parts are made). The following descriptions are made in accordance with [1.1], [1.2], [1.3], [1.4], [1.5] and [1.6].

### **1.1.1 Pre-preg lay-up and autoclave curing**

In this manufacturing system, pre-preg plies are used. These materials are unrolled and cut according to certain lengths. From the cut plies, patterns are obtained with the desired fiber orientation for each layer, which will shape the final form of the piece. It is necessary to keep in mind when cutting the plies that the edges of the piece must be discarded (because do not comply with the terms of fiber orientation, fiber volume fraction and thickness required of the entire piece). For that reason, patterns must always be oversized. Such patterns are placed over the appropriate mold, which previously has been protected with release agent, either solid (nylon sheets) or liquid (Frekote<sup>®</sup>), helping to the compaction of the pre-preg plies with a nylon spatula. In the case of complex geometries, the shaping of the plies can be helped by means of a small increase in temperature (it is important to avoid an overheating to prevent the starting of the polymerization reaction), either externally (using a heater) or by heating the mold (this technique is known as hot forming). In order to improve compaction, every several layers (not more than 5) an intermediate vacuum bag (similar to the final vacuum bag, described below) is used, which will act about 10 minutes.

Once all the sheets have been compacted, the vacuum bag is formed. The vacuum bag is important in the manufacturing process because it helps to compact the laminate and protects the resin to be burned during the curing process (if the bag breaks during the curing process, the molecules of the resin react with oxygen of the surrounding air, obtaining non-desired species). During the vacuum bag forming, the first step is to close the perimeter of the piece with cork. Thus, the excess of resin is absorbed, preventing the flow of the resin out of the mould. This step is very important because if the cork is not well placed, bad results shall be obtained after

the curing due to the flow of the resin. The laminate is then covered by a Nylon sheet (in order to help the demoulding of the laminate) and an airweave<sup>®</sup> ply (that helps to distribute the vacuum inside the bag). The perimeter of the part is sealed with a sealant tape. Then, a bag closing plastic is placed over the part. Finally the vacuum intakes are placed and the vacuum is done. Two vacuum intakes are placed, one to extract the air and the other to measure the vacuum inside the bag. To verify that the laminate has the correct temperature during the curing process, at least two thermocouples (one connected to the laminate to be cured and another connected to the mould) have to be placed. A view of a vacuum bag is shown in Figure 1.1.

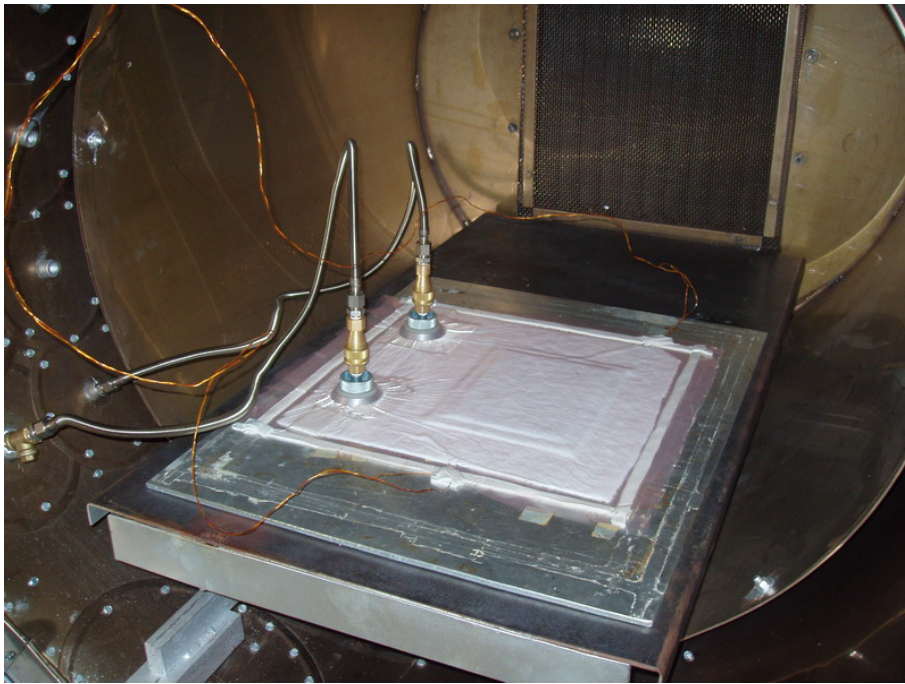


**Figure 1.1. View of a vacuum bag**

Once the vacuum has been done and it has been checked that there are no vacuum leakages, the vacuum bag is put into the autoclave. In the case of large autoclaves, "trains" which contain many pieces are introduced, so that the capacity of the apparatus is optimized by minimizing the timeout of the parts to be cured.

The autoclave comprises a sealed chamber in which a gas is introduced under certain conditions of temperature and pressure. At the same time, the vacuum

and the temperature within the bag are controlled. Although it is common to use air as heat and pressure transmitter, it is also usual to use argon, especially for high temperature curing cycles. The reason is that argon is an inert gas, that no burns, as would happen with the air at high pressure. A complete view of an autoclave is shown in Figure 1.2.

Once cured, the parts present different finishes on their faces, having a smooth and glossy finish on the side facing the tool and a rough matte finish on the side facing the mould. A smooth finish on the entire part can be obtained using special tools.



**Figure 1.2. View of an autoclave**

Due to the way of transmitting the pressure, the autoclave can produce parts of almost any geometry. Depending on the part to manufacture and the laminate stacking sequence, the lay-up stage and the preparation of the vacuum bag can take several days, the process being very expensive.

The processing time of the autoclave is usually around 4 hours for thin laminates (0 to about 10 mm) up to 8 hours for large thicknesses (from 10 mm). In both cases the polymerization time is between 2 and 3 hours, the difference being that for thick layers a step of temperature stabilization (at the point of lowest viscosity of the resin) is required before reaching the curing temperature.

Due to the use of prepregs in this type of manufacture, very high volume fractions of fibers (> 60%) may be achieved, obtaining parts with very high mechanical properties. In turn, good dimensional tolerances in terms of thickness are obtained. To reach the desired external dimensions the edges have to be machined.

The major drawbacks of this system are the processing time, the final cost of the parts and that is not the most suitable technique for high production volumes.

## **1.2 Out-of-autoclave manufacturing**

The autoclave has been used to manufacture composite parts since the beginning of the composite materials. However, its use entails high production costs and large process times. Furthermore, not all the composite parts need the characteristics obtained with the autoclave. These are the reasons by which the industry has searched several alternatives to the autoclave; in one hand systems capable to obtain parts with the quality of the autoclave but reducing the costs and process times and, on the other hand, to manufacture low quality parts at low cost. All these systems have been included in the out-of-autoclave name.

Several of the out-of-autoclave systems used to manufacture composite parts will be shown next.

## 1.2.1 Oven

This curing system consists of a sealed chamber in which air is introduced by convection at a certain temperature. Due to the absence of pressure and vacuum, the compaction of the laminates is usually very poor. A vacuum bag can be used to improve the compaction, but controlling it with an external equipment.

Due to the lack of pressure, the system is usually combined with other manufacturing methods in which the material is compacted sufficiently well during the stacking process, as the LIR or the roll wrapping methods. It is commonly used in the pot-curing of manufactured parts.

In the curing of the parts, if a vacuum bag is used, the procedure is similar to that described in the autoclave. In case of not applying vacuum, the bag consists of wrapping the part in a sheet mold release film, avoiding the appearance of air bubbles in the folds. Once wrapped the part, the bag is closed with high temperature tape to seal the edges, thus preventing resin leakages.

Figure 1.3 shows a picture of a commercial oven for the aeronautic industry.



**Figure 1.3. View of an oven<sup>1</sup>**

---

<sup>1</sup> Taken from <http://www.dycometal.com/>

Compared to the autoclave:

- The cost of the equipment is low.
- The auxiliary materials cost is low.
- The Compaction of the parts is very poor.

## 1.2.2 Hot plates press

The system comprises two opposing pistons to apply pressure to the laminates. Two flat plates at the end of the pistons apply the pressure. The plates are also heated to achieve the curing of the resin. If a better compaction of the parts is needed, vacuum controlled with external equipment can be applied.

This procedure mainly uses pre-pregs. The lamination of the layers is performed in a similar way as in the autoclave. The type of bag used is similar to that described for the oven (it is only a demoulding bag), taking into account the need to protect both all edges and corners with high temperature tape to prevent the breakage of the bag due to the pressure of the plates.

Once the bag has been prepared, it is inserted in the center of the plates, in order to apply the load as homogeneous as possible.

The quality of the parts obtained by this procedure can be very close to the ones obtained with the autoclave. However, their small size and the method of introducing the load, restricts their use to laboratory test pieces and small flat panels for low production volumes.

A view of a hot plate press is shown in Figure 1.4.



**Figure 1.4. View of a hot plates press<sup>2</sup>**

Compared to the autoclave:

- The cost of the equipment is low.
- The cost of the auxiliary materials is low.
- Only allows flat parts to be manufactured.

The parts obtained need to be machined because the edges undergo a reduction in thickness due to the presence of the high temperature tape.

---

<sup>2</sup> Taken from [www.fontijnegrotnes.com/](http://www.fontijnegrotnes.com/)

### 1.2.3 Quickstep

The system [1.4] consists of two vessels enclosed by membranes containing a liquid with a very high thermal conductivity. Once the part is placed between the membranes, temperature and pressure is applied to the liquid contained therein. Due to the high thermal conductivity of the fluid it is possible to minimize the heating time of the parts manufactured.

The pressurization through two flexible membranes requires a very fine control to avoid undesired surface undulations of the laminates.

This method can be used both with pre-pregs or with the fibers and the resin separately. In the first case the parts are laminated in a similar way as with the autoclave. In the second case it is necessary to laminate and compact with another manufacturing system, such as the liquid resin infusion processes (described in Section 1.2.6), the Quickstep being used in the curing or post-curing stage.

The laminate has to be wrapped in a mold release film before being placed in the equipment.

Compared to the autoclave:

- The cost of the equipment is high.
- The auxiliary materials cost is low.
- Only allows to manufacture flat or slightly curved parts.

The parts obtained are very close to the desired final shape, minimizing (or even eliminating) the machining operations.

A view of a Quickstep machine is shown in Figure 1.5.



**Figure 1.5. View of a Quickstep machine<sup>3</sup>**

In order to compare the possible benefits of the Quickstep with the autoclave, several mechanical properties obtained in laminates manufactured with both systems are shown in Table 1.1 (taken from [1.7]). The difference between the three Quickstep present methods is in the heating and cooling ramps applied in the curing cycle. It can be noticed that the Quickstep methods are much faster than the autoclave (because heat transfer is carried out with liquid and not with gas), but the final properties of the parts are worse.

---

<sup>3</sup> Taken from <http://www.quickstep.com.au/>

	Quickstep			Autoclave	Oven
	QSpoke	QSDwell	QSstraight		
Bending strength (MPa)	1755	1477	1322	1923	1505
Interlaminar shear strength (MPa)	115	84	71	111	84
Voids content (%)	1.8	8.1	12.3	0.6	8.9
Fibre volume fraction (%)	60.2	55	49	64.1	54.2
Mean thickness of the panel (mm)	2	2.12	2.25	1.97	2.1
Time (min)	~180	~170	~160	~270	~270

**Table 1.1. Comparison between several mechanical properties obtained with the Quickstep methods and the autoclave**

## 1.2.4 Hand lay-up

In this system the raw materials are fibers and resin separately.

First, the resin is mixed with an activating agent. Then, a layer of resin is spread over the mold. Next, a layer of fibre is placed. This fibre layer is impregnated with a new layer of resin with a roller. The same process is continued until completing the desired number of layers.

Once laminated, the part is cured at room temperature or is cured in an oven, depending on the type of resin used.

Compared to the autoclave:

- The equipment cost is very low.
- The auxiliary materials cost is low.
- The process allows parts of virtually any shape and any size to be manufactured.

A stage of the procedure can be seen in Figure 1.6.



**Figure 1.6. View of a stage of the hand lay-up process<sup>4</sup>**

---

<sup>4</sup> Taken from <http://www.smechapter5.org/>

It has to be taken into account that the finishing of the final part depends heavily on the good work of the operator, so it is very difficult to obtain specific fibre orientations and thicknesses and uniform fiber volume fractions. For all these reasons, the dimensional tolerances in this manufacturing system must be very high.

This system is used in aerospace manufacturing for parts with low structural responsibility.

As the system uses an open mold, it has the environmental problem of emission of styrene.

### **1.2.5 Filament winding**

This system uses non-impregnated fibers. First they are passed through a bath of resin and then they are wound around a rotating mandrel, giving thickness to the part. Once finished the process, the piece is cured by entering in an oven.

The compaction pressure during winding is given by the own traction with which the fibers are pulled. To improve the finishing of the parts manufactured, an external compaction system can be used, as for example the ultrasonic compaction system, explained along this work.

Compared to the autoclave:

- The cost of the equipment is medium.
- The auxiliary materials cost is low.
- It permits to manufacture cylindrical parts automatically for large production volumes. Moreover, the parts manufactured present the desired final shape and practically do not require to be machined.

- Due to the placement and compaction system, the system can reach a maximum of 60% fibre volume fraction.

This method has the drawback of the difficulty of obtaining fiber orientations lower than  $15^\circ$  with respect to the revolution axis of the part. This fact induces that the manufactured parts do not support well the loads in the longitudinal direction. Thus, their use is being restricted to the manufacture of gas tanks and similar structures, in which the main loads are radial and circumferential.

A view of a filament winding machine can be seen in Figure 1.7.

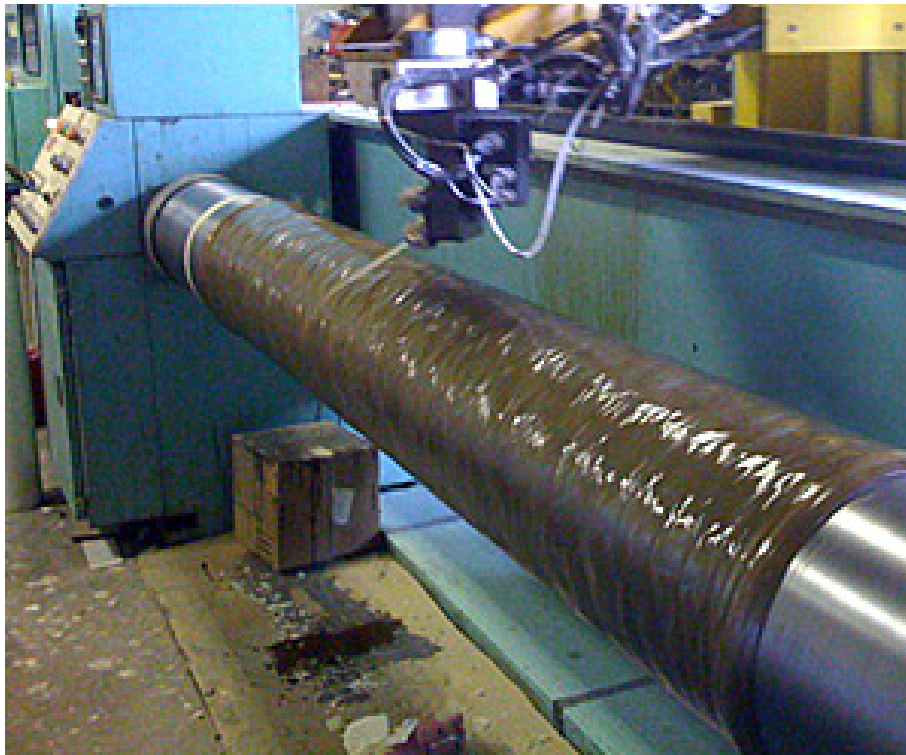


**Figure 1.7. View of a filament winding machine<sup>5</sup>**

---

<sup>5</sup> Taken from <http://www.indiamart.com/valeth-hightech-composites/>

## 1.2.6 Liquid resin infusion (LRI)

This name refers to a large family of manufacturing systems.

These systems are booming nowadays and let be modified in many ways, so many companies have developed their own methods, the differences not being very significant among many of them [1.8]. Some of the variations on this procedure are listed in what follows:

CIRTM: co-injection RTM

MVI: modified vacuum infusion

RFI: resin film infusion

RIFT: resin infusion under flexible tooling

RIRM: resin injection recirculation moulding

RTM: resin transfer moulding

VAIM: vacuum-assisted injection moulding

VAP: vacuum assisted processing

VARI: vacuum assisted resin injection system

VARIM: vacuum assisted resin injection moulding

V(A)RTM: vacuum (-assisted) resin transfer moulding

VIM: vacuum infusion moulding

VIMP: vacuum infusion moulding process

The process, trying to generalize the set of methods, is as follows:

- The fibers are placed (without resin) on the mold.
- A vacuum bag is made or a countermould is placed over them.
- The fibers are impregnated with resin by one of the following procedures:
  - \* Application of pressure in the resin tank.
  - \* Application of vacuum in an area of the mould opposing to the resin tank.
  - \* Application of a combination of the abovementioned methods.
- The part is cured by heating the mold and/or the air surrounding it.

In systems similar to RTM, in which the mold is rigid (both mold and countermould are metallic) the pressure for the compaction is given only by the pressure at which the resin is injected, then becoming a critical parameter in the process. In the systems with flexible mold, the pressure can be applied from outside the mold.

Compared to the autoclave:

- The cost of the process is low.
- Processing times are short.
- Allows almost any geometry to be manufactured and parts obtained are very close to the final shape, saving costs and time in machining processes.

The main drawback of these methods is that, before being put into operation for each part, it requires many trials or accurate models to ensure the appropriate

flow of the resin. Otherwise, zones in which the fiber is not impregnated with resin or areas with high accumulations of resin may appear. Because of this, it is difficult to achieve homogeneous values of the thickness in the parts.

These methods can be combined with autoclave curing, controlling the outer pressure and temperature of the part, as is done in the case of the SLI (Single Line Injection) system.

These methods can be also combined with the Quickstep system to make post-curing stages.

Figure 1.8 shows a sketch that represents, in a general way, a summary of the operation of the LRI processes.

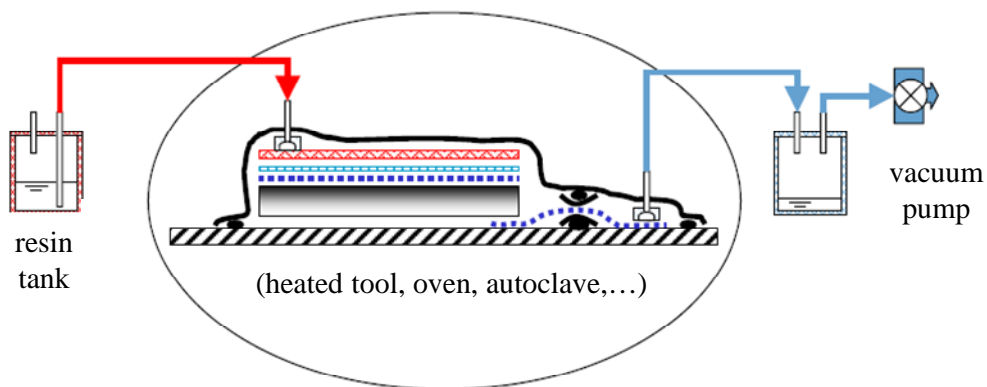


**Figure 1.8. Sketch of the LRI processes**

### 1.2.7 High energy Electron-Beam

In this manufacturing system [1.9], the curing of composite parts is performed by a high power electron gun. The raw material consists of pre-pregs conformed by special resins. These resins do not cure with the temperature but with the destruction of double bonds they have in their internal structure by the impact with the electron beam. The stacking of the layers is performed in the same manner

as when the pre-pregs are manufactured in autoclave. Once stacked and compacted the part, the electron gun is used, thus achieving the cure of the resin.

Compared to the autoclave:

- This system is expensive, not only because of the inherent cost of the equipment, but by the need to strongly isolate the working area from radiation.
- Curing time is minimal because the entire part is cured almost instantaneously.

A view of the high energy electron-beam can be seen in Figure 1.9.



**Figure 1.9. View of a high energy electron-beam machine**

### **1.2.8 Low energy Electron-Beam**

This system [1.9] is similar to the abovementioned high energy electron-beam but, in this case, the electron gun is a low power one, thereby achieving cost

savings. As low power, the electron gun cannot penetrate very deep in the material, so it is only able to cure few plies (no more than two plies at a time). The equipment incorporates an automatic lay-up system (ATL), which places the sheets on the way they are cured.

The equipment operation is as follows:

- A pre-preg ply is placed on the first pass.
- In the next pass the radiation partially cures the placed ply and the next ply is placed (the ATL system is located behind the electron gun).
- Then the upper ply is partially cured and the following ply is completely cured.
- Next a new ply is placed and the process continues until laying-up and curing the top ply of the laminate.

The placing of the plies with the ATL system does not ensure a good compaction of the laminate, so that the equipment requires a compaction system prior the curing of the plies.

Compared to the high energy electron-beam:

- This equipment is cheaper and the isolation required for the facility is low.
- In the current prototypes only flat parts are manufactured.

As an alternative to the electron beam, other possibilities to cure the resin of the laminates with radiation can be done, as plasma beams or microwaves.

A scheme of the low energy electron-beam attached to an automatic tape lay-up equipment can be seen in Figure 1.10.

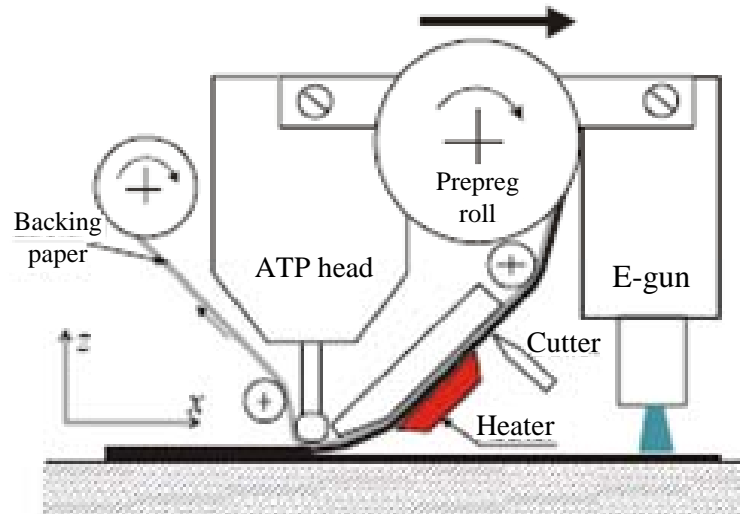


**Figure 1.10. Draft of a low energy electron-beam system**

Compared to the autoclave:

- This system is cheap.
- The curing time is very low, because it lasts the double of the time the ATL needs, more or less.
- The system needs a huge set-up to obtain parts with high mechanical properties.

### 1.2.9 Pultrusion

The conception of this system is similar to the metal extrusion process, in which the material is passed through a preform, pressing against it, to obtain profiles with sections of almost any geometry. In the case of the composites pultrusion, instead of pressing, the fibers are pulled.

The raw material is a non-impregnated bundle of fibers. The bundle is pulled, passing it through a resin bath. The impregnated bundle is passed through a

heated preform, giving the part its final shape and curing it (totally or partially, in this latter case to post-cure the parts in an oven being necessary). Finally, the profile is cut to the desired length using a cutting saw.

The main advantages of this system are that parts with constant length and section are automatically produced with a low cost, therefore allowing to manufacture large production volumes.

The main disadvantages of this system are that the maximum fiber volume fractions that can be obtained are not very high and that the fibers can only be inserted in the direction of the pulling, then resulting in structures which can only support axial loads properly. In the case to need profiles with strength and stiffness in the direction perpendicular to the axial, woven fabric can be used, though the production process is greatly complicated.

A view of the pultrusion process is shown in Figure 1.11.



**Figure 1.11. View of a pultrusion machine<sup>6</sup>**

---

<sup>6</sup> Taken from [www.strongwell.com/](http://www.strongwell.com/)

## 1.2.10 Spray-up

In this system the fiber and resin are sprayed over a mold. To be sprayed, the fibers must be in the form of whiskers (short fibers). The raw material is a roll of unidirectional fiber and the ejector cuts it into short fibers. After cutting, the fiber is mixed with the resin and the mixture is sprayed over a mold. The curing of the part is usually at room temperature, although, depending on the type of resin, it may need to be cured in an oven.

The process can be carried out both manually, consisting of a spray handled by the operator, or automatically, consisting of a mechanical arm that can be moved in the plane of the part and perpendicularly to it, attached to a head (that handles the spray gun) which is rotated by having at least one rotation axis. The automatic system, besides the movement of the gun, controls the amount of material to be spread over the mold, obtaining values of the thickness much more homogeneous than in the case of performing it manually.

A view of the spray-up system can be appreciated in Figure 1.12.



**Figure 1.12. View of a spray-up system<sup>7</sup>**

It is a quick and inexpensive system to produce parts of little structural responsibility. In addition, it allows large volume of parts to be manufactured.

<sup>7</sup> Taken from <http://performancepolytek.com/>

As the operation is carried out in an open mold, the system has the environmental drawback of styrene vapor emissions.

### 1.2.11 Compression molding

This system resembles the metal stamping. In the compression molding a block of composite material (in this case a mix of resin and short fibers in a fibre volume fraction less than 30%, in order to allow an appropriate flow of the matrix to be maintained) is put on a preheated mold (usually about 140 °C). Then the material is pressed with an upper mold reaching the filling of the entire cavity by the material. After this process, the molds are heated until achieving the complete curing of the part. The mold used is usually closed. Thus, a good estimation of the amount of material that must be present in the starting block is required.

A view of the compression moulding machine is shown in Figure 1.13.



**Figure 1.13. View of a compression moulding machine<sup>8</sup>**

---

<sup>8</sup> Taken from <http://clearcarbon.com/>

The equipment, and especially the molds (because they have to be manufactured very precisely to fit) are expensive, but the raw material is cheap. The processing time is short and this system is used in the production of large quantities of non-structural parts.

The process can be used with pre-pregs as raw materials.

### **1.2.12 Roll wrapping**

This procedure is used in the manufacturing of cylindrical tubes. The raw materials are prepregs. The material is cut according to a certain pattern and is wound around a cylindrical mandrel. Once the wrapping operation is finished, a tape that shrinks when heated is placed around the pre-preg. This tape will be responsible for transmitting the pressure to the laminate during the polymerization phase. The part is cured in an oven. Once the process is finished, the tape is removed and the mandrel is extracted from the tube.

The process is inexpensive and produces large volumes of parts but it requires considerable expertise in the work of the operator. It has the great advantage that, as the raw materials are prepregs, it is possible to obtain higher fiber volume fraction than in the case of other manufacturing systems that can generate tubes as the pultrusion and filament winding, obtaining parts of better mechanical properties.

It has the great disadvantage that, for orientations different of  $0^\circ$  and  $90^\circ$  (and also for these orientations), it is difficult to get a correct orientation of the fibers, causing distortions in the expected final properties of the tubes.

In order to automate and increment the process speed, the rolling of the layers and of the pressure tape can be done by automatic wrapping machines.

An image of the roll wrapping technique is shown in Figure 1.14.



**Figure 1.14. View of a the roll wrapping technique [1.2]**

### **1.2.13 Injection molding**

The raw material is similar to the compression molding process, consisting of little blocks of resin and short fibers. These blocks are liquefied and pressed into a heated mold that gives the shape and cures the part.

The process is expensive because of the precision required in manufacturing the molds.

The great advantage of this system is that it is very fast, being then possible to obtain pieces in less than 1 minute and without subsequent machining processes.

This process is used for producing small parts of no structural responsibility, such as head connectors for cable bundles.

A view of an injection molding machine can be seen in Figure 1.15.



**Figure 1.15. View of an injection molding machine<sup>9</sup>**

## 1.3 Prototype under study

As mentioned before, on the way of searching a valid alternative (in terms of mechanical properties obtained in the final parts) to the autoclave manufacturing, a prototype is being developed by AIRBUS. The parts of the prototype will be described next. Then, the possible movements the prototype can do are commented. Finally, the ultrasonic compaction system will be described in depth.

### 1.3.1 Parts of the prototype

The prototype consists on three main systems [1.9]:

#### *Automatic tape lay-up system (ATL):*

This system is used to lay-up and cut the composite plies over the mould. It has a measuring system that assures that the cut of the plies is made at the correct length. The system consists on:

---

<sup>9</sup> Taken from <http://spanish.molding-machinery.com/>

- An unrolling system to lay-up the composite pre-preg.
- A roll used to collect the pre-preg polyethylene protection tape.
- A system to control the length of the ply cuts.
- A cutting blade.

The width of the pre-preg composite tape that this system is capable to lay-up is 8 cm.

***Ultrasonic compaction system (USC):***

This system is used to compact the plies on the way the ATL lays them up. This system consists on:

- An ultrasonic device, which vibrates and transmits this movement to the composite laminate through its titanium tip.
- Two compaction rolls that can be used to help the ultrasonic compactor during the compaction. The rolls are located before and after the ultrasonic compactor, in the compaction direction.

***Composites curing device:***

This system is used to polymerize the resin of the pre-preg layers, after they are placed and compacted. Several curing systems (that will work separately) have been implemented, depending upon the resin to cure.

- Electron beam curing device
- Plasma beam curing device

The system also includes an infrared heating system, for helping the mentioned devices in the pre- and post-curing processes.

The whole system is shown in Figure 1.16.

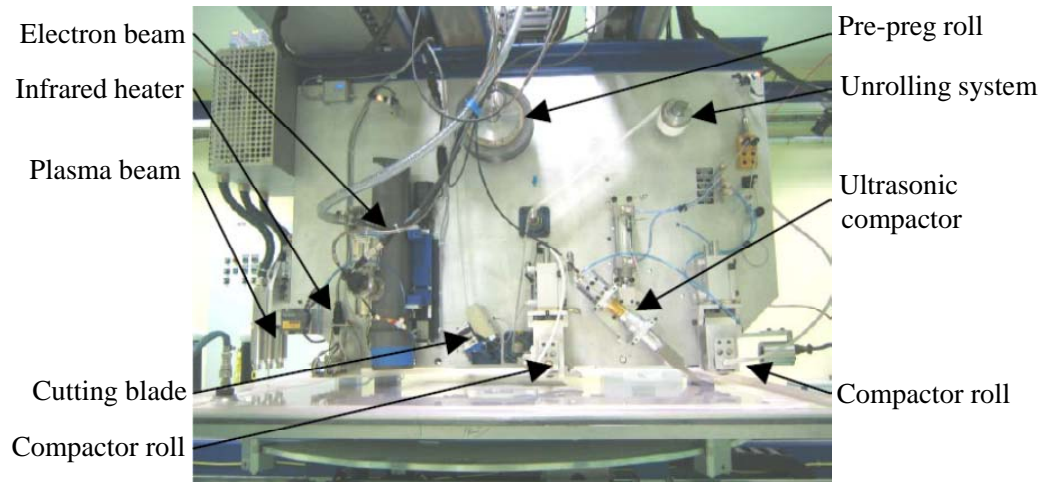


**Figure 1.16. View of the prototype under study [1.9]**

### 1.3.2 Movements of the prototype

The movements the prototype can develop determine the type of laminates that can be manufactured by the prototype. These movements are:

- Rotation around the  $y$  axis (vertical axis on picture shown in Figure 1.16). The equipment allows several ply orientation angles to be obtained. The different angles are obtained turning the table that supports the mould where the laminate is laid-up. The ply angle can be modified from  $0^\circ$  to  $90^\circ$ .
- Displacement along the  $x$  axis (horizontal axis in the picture shown in Figure 1.16). With this displacement, the pre-preg tape is stacked over the mould, along the lay-up direction.
- Displacement along the  $z$  axis (this axis is perpendicular to the picture shown in Figure 1.16). This displacement allows parallel pre-preg tapes

to be laid-up, giving width to the panels. This movement is achieved moving the part where the ATL machine is placed along the  $z$  axis.

The equipment, the table and the possible movements of the prototype are shown in Figure 1.17.

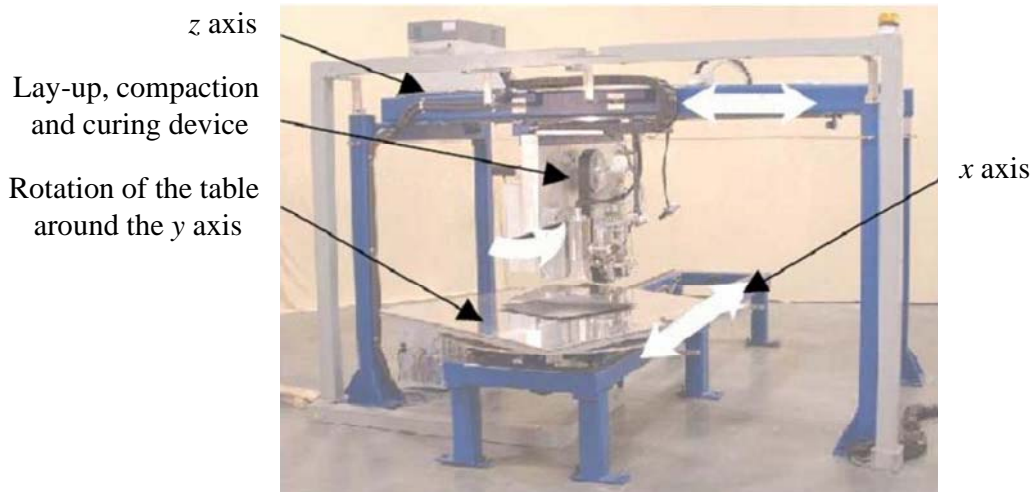


**Figure 1.17. Possible movements of the prototype [1.9]**

With the movements described, the prototype can lay-up flat, square or rectangular, panels, with  $0^\circ$ ,  $90^\circ$ ,  $+45^\circ$  and  $-45^\circ$  orientation angles. The maximum possible dimension of the panel to manufacture is  $1 \times 1 \text{ m}^2$ .

The panels are manufactured oversized and cut to the right dimensions after curing, in order to avoid the possible border defects that usually appear in these manufacturing processes.

### 1.3.3 Ultrasonic compaction device

A view of the ultrasonic compaction device [1.6, 1.9, 1.10, 1.11, 1.12, 1.13] is shown in Figure 1.18.

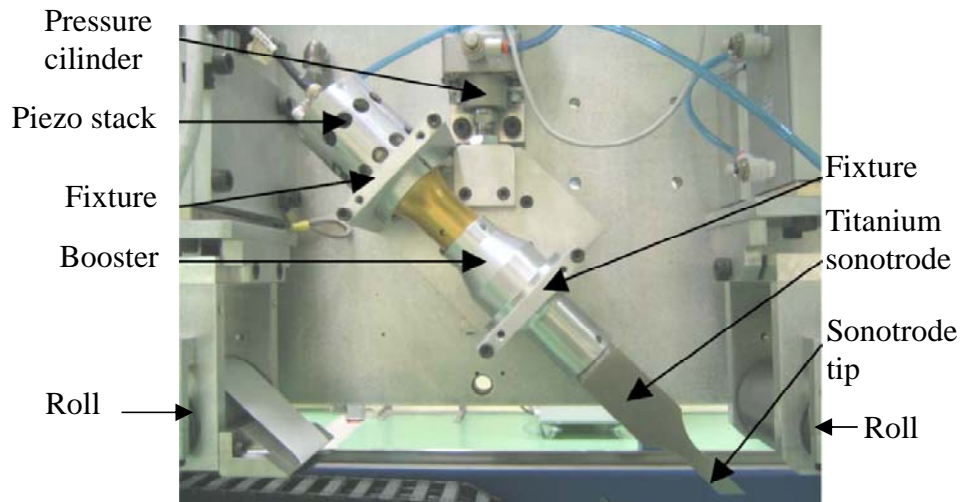


**Figure 1.18. View of the ultrasonic compaction device [1.9]**

The material to compact is placed under the titanium tip of the sonotrode, at the bottom of Figure 1.18. The laminate is placed over an aluminum table, which makes the function of a mould, in order to obtain flat panels. Over the mould, several materials are placed:

- A peel ply layer: used to avoid the sliding of the first layer when it is laid-up. This layer remains joined to the composite and is removed after the curing of the part.
- A nylon antiadherent film: used to protect the mould and to avoid the adherence between the composite and the mould.

The system has two rolls for helping in the compaction procedure. One roll is located before the sonotrode and the other is located after the sonotrode. Both rolls can be heated and the pressure transmitted to them can be modified. The influence of the rolls has not been proved, not then being used at this time.

In principle, the angle that the ultrasonic compactor forms with the laminate is fixed, it being  $45^\circ$  from the vertical axis.

A scheme of the materials that can be found under the sonotrode is shown in Figure 1.19.

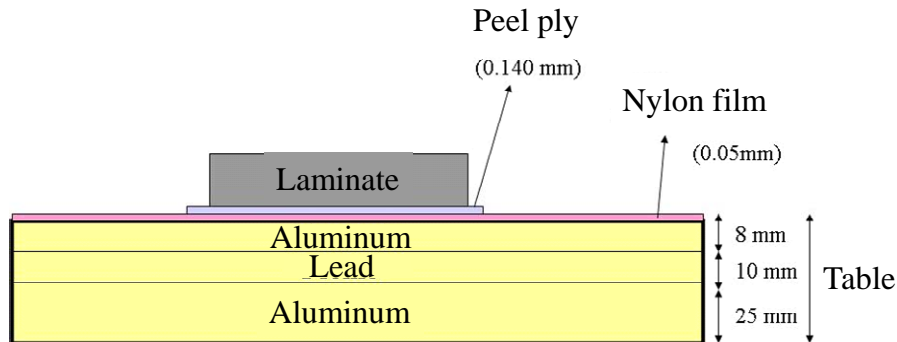


**Figure 1.19. Scheme of the materials located under the sonotrode**

## 1.4 Scope of the Thesis

The main objective of this Thesis is the modelling of the heat generation and distribution inside the resin of a composite laminate that is submitted to ultrasonic vibrations. Thus, the ultrasonic compaction process can be understood properly and the process may be optimized. An appropriate modelling of the thermal field in the laminate will avoid the use of a huge number of experiments to calibrate the best combination of parameters (amplitude of the ultrasounds, horizontal displacement velocity of the sonotrode...) to define the optimal functioning of the equipment.

Several secondary objectives have also guided the present work:

- The understanding of the compaction process.
- The study of how the ultrasonic vibration induces the heating of the resin.
- The study of the possibility of curing the resin (even partially) during the compaction process due to the temperature raised inside the resin.

The Thesis has been structured in 10 Chapters, whose content is described in what follows:

- In Chapter 2, some previous analyses will be commented. First, the main ways the prototype can operate to compact the composite layers will be remarked.

Then, several experiments concerning the ultrasonic compaction and the materials involved will be shown. The results given by these experiments will be used in the following chapters to complete or validate the models developed.

- In Chapter 3, the main problems that will be studied in this work will be posed. These problems are the static compaction, in which the sonotrode is not moving along the laminate, and the dynamic compaction, in which the sonotrode is moving along the laminate.

For each of the problems, the geometry, the boundary conditions and the heats involved in the processes will be commented.

- In Chapter 4, several analyses prior to study the heat generation will be presented.

First, a thermal model used to study the temperature evolution during the compaction process will be presented. In this model, the heat generated will be an input, so is only valid when the heat generated or part of the temperature field is known a priori. This model will be used to validate the thermal properties given in the literature.

Second, a curing model has been developed. The equations that describe the cure kinetics will be shown, obtained from the experimental results presented in Chapter 1. This curing model will be implemented in a thermal one, in order to obtain the evolution of the degree of cure during the ultrasonic compaction process.

Finally, a model that describes the evolution of the viscosity of the resin with the temperature will be presented. This model will be used in the next chapters in conjunction with the heat generation model.

- In Chapter 5, the modelling of the heat generation will be studied.

First, several considerations about the constitution of the pre-preg and its implications on the transmission of the ultrasonic movement will be done.

Second, the boundary conditions of the resin layers will be posed.

Finally, the equations that govern the heat generation inside the laminate under ultrasonic vibrations will be established.

- In Chapter 6, a semi-analytical model developed to solve the heat generation and distribution during the static ultrasonic compaction is shown. This model will also be used to verify the validity of the heat generation model presented in Chapter 5.

First, several considerations about the possibilities and differences of implementing two possible pre-preg models will be presented.

Second, the equations and hypotheses used to model the heat distribution and the heat generation will be posed.

Third, an incremental algorithm to solve the problem and its implementation in a commercial mathematical program will be commented.

Finally, the results obtained with the model and its comparison with experimental results will be shown. The validity of the pre-preg models will be checked also.

- In Chapter 7, a 2D FEM model that to improves the solution obtained with the semi-analytical model, presented in Chapter 6, will be developed.

First, the equations and hypotheses used to model the heat distribution and the heat generation will be posed. An algorithm to solve these equations will also be presented.

Second, several considerations about the geometry and the mesh used in the model will be illustrated.

Finally, the results obtained with the model will be shown and compared with experimental results.

- In Chapter 8, the static compaction process will be reformulated, in order to solve it with the Proper Generalized Decomposition, a numerical technique capable to solve the problem in a reasonable time using very fine meshes.

First, a way of solving the problem will be presented.

Second, the formulation of the equations that solve the problem with the Proper Generalized Decomposition will be developed.

Finally, the results obtained with this model and an experimental validation will be shown.

- In Chapter 9, the dynamic ultrasonic compaction process will be solved, the Proper Generalized Decomposition being the numerical solving technique chosen to this end.

As done in Chapter 8, a way of solving the problem and the formulation of the equations that solve the problem with the Proper Generalized Decomposition will be presented first.

Then, the results obtained will be shown.

As no experimental data are available to validate the results obtained with this model, a parametrical study will be carried out with the variables that can be modified in the ultrasonic compaction prototype.

- In Chapter 10, the conclusions of this work and several possible future developments will be posed.

## Bibliography

- [1.1] Bader, M.G., Smith, W., Isham, A.B., Rolston, J.A., Metzner, A.B.: *Processing and Fabrication Technology*. Technomic Publishing Co., Inc., Lancaster Basel, Vol. 3, 1990.
- [1.2] Campbell, F.C.: *Manufacturing Processes for Advanced Composites*. ELSEVIER, 2003.
- [1.3] Díaz, M.: *Fabricación y Mecanizado de Materiales Compuestos*. Fundación General U.P.M., Madrid, 2002.
- [1.4] Mazumdar, S.K.: *Composites Manufacturing. Materials, Product, and Process Engineering*. CRC Press, 2002.
- [1.5] Fernández, I., Blas, F., Frövel, M.: *Autoclave forming of thermoplastic composite parts*. Journal of Materials Processing Technology, 143-144, pp. 266-269, 2003.
- [1.6] Leemon, V., Bullock, D., Roylance, M.E., Woods, J.E., Boyce, J.S., Player, J.: *Ultrasonically method of fabricating a thermosetting matrix fiber-reinforced composite structure and the product thereof*. WO02/32664A1, Patent, 2002.
- [1.7] Davies, L.W., Day, R.J., Bond, D., Nesbitt, A., Ellis, J., Gardon, E.: *Effect of cure cycle heat transfer rates on the physical and mechanical properties of an epoxy matrix composite*. Composites Science and Technology, 67, pp.1892-1897, 2007.

- 
- [1.8] Beckwith, S.W.: *Resin Infusion, Liquid Molding, Vacuum Infusion Processing, and Numerous Other Names. An Alphabet Soup of Expanding Technologies*. SAMPE Journal, 42, 1, 2006.
- [1.9] Seebacher, S.: *Contributions to the investigation of in-situ ultrasonic tape lamination of composite thermoset prepregs*. Master thesis at the Private fachhochschule Göttingen, 2008.
- [1.10] Player, J., Roylance, M.E., Roylance D.K.: *UTLTM consolidation and out-of-autoclave curing of thick composite structures*. SAMPE 2000, Proceeding, 2000.
- [1.11] Player, J., Roylance, M., Zukas, W., Roylance D.: *Modeling of Ultrasonic Processing*. JAPS, Article, 2004.
- [1.12] Roylance, M., Roylance D., Nasmith K.: *Use of ultrasonic tape lamination of in-process debulking of thick composite structures*. Naval Air Warfare Center Aircraft Division, Report, 1998.
- [1.13] Thomson, D.T., Roylance, M.E.: *Ultrasonically tape lamination for net thickness composites processing*. SAMPE, Proceeding, 2000.



# *Chapter 2*

## *Previous analyses*

After having described the objective of the Thesis and having framed the prototype that is being studied, several previous analyses, that help to understand the models that will be developed in the following chapters, are going to be presented in this chapter.

In Section 1.1, two possible compaction procedures that can be carried out with the ultrasonic compactor will be shown. The models presented in next chapters will focus on the second of these compaction procedures.

In Section 2.2, several experiments carried out related with the ultrasonic compaction and the pre-preg materials studied in this work will be posed. The data obtained with these experiments will be used in the models that will be presented in the following chapters of this work, either to validate the models or to provide some input data needed in them.

## **2.1 Compaction procedures**

Two possible compaction procedures of the prototype will be described in this section: compaction of one uncured ply after having cured the precedent plies and compaction of several uncured plies. Depending on the compaction procedure, different states of the resin can be found in the laminates. The election of the compaction procedure will condition the curing technology used, a layer-by-layer radiation curing technique in the first case being needed and a traditional oven or autoclave curing technique being required in the second case.

### **2.1.1 Compaction of one uncured ply**

In this case, in a single pass of the prototype one layer is placed, compacted and partially cured. In the following pass the next layer is laid-up, compacted and partially cured, the previous layer being completely cured.

As the compaction and curing is carried out ply by ply, different states of the resin can be found in different resin layers during the compaction process. Each state will have different contributions to the heating of the lay-up. A typical situation in this compaction procedure can be seen in Figure 2.1, with the top ply having two layers of uncured resin separated by a fibre layer (this supposition about the modelling of the pre-preg will be commented and analyzed in Chapters 5 and 6,

respectively), the composite ply below it being formed by well distributed fibres in partially cured resin and the following composite plies being completely cured.

As will be assumed in Chapter 5, the contribution of the uncured resin layers to the heating process can be modelled as that corresponding to a viscous fluid. For the case of the semi-cured ply, considering the slight influence of this ply to the heating process, its contribution will not be taken into account in this study. However, in the case of modelling it, it is unsuitable to consider it as a viscous fluid, a viscoelastic model being more appropriate. Finally, the completely cured plies will not contribute to the heating since they can be considered as fully elastic and thus they do not dissipate energy.

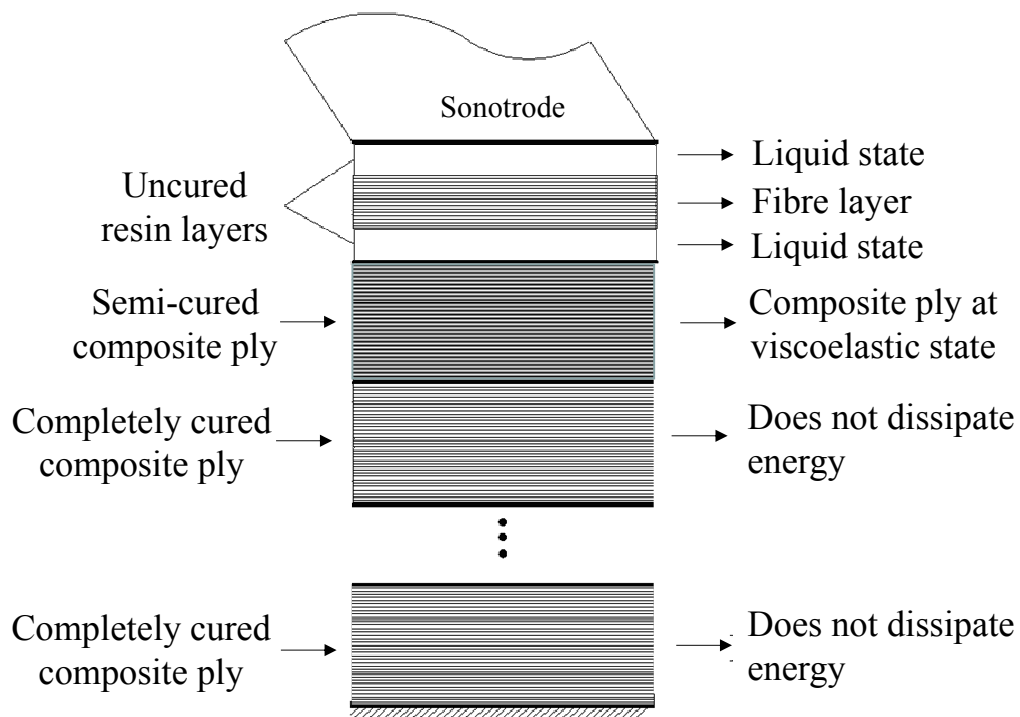


**Figure 2.1. Schematic view of the typical situation encountered when compaction and curing is carried out ply by ply**

## 2.1.2 Compaction of multiple uncured plies

In this case, all the plies are laid-up, then they are compacted at the same time and, finally, they are cured.

When the curing process is going to be applied, once the ultrasonic compaction process has been carried out in the whole laminate, the situation will be like the one shown in Figure 2.2, in which some uncured plies are laid up to form the full laminate.

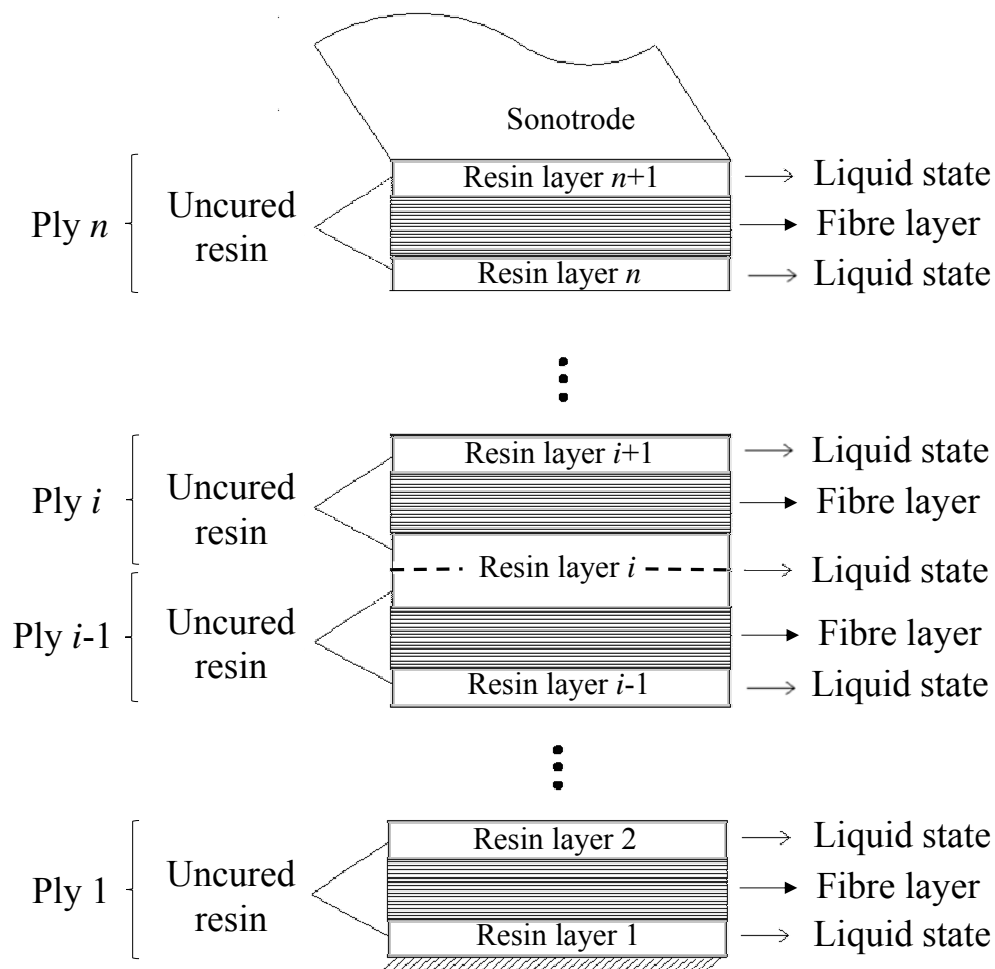


**Figure 2.2. Schematic view of the typical situation encountered when compaction of the whole laminate is carried out before curing**

Note that, as will be analyzed in Chapter 5, the pressure will be transmitted vertically, so the oscillatory movement will be transmitted to all resin layers (this movement will be muffled from the top to the bottom layer).

The terminology and notation that will be used for the pre-preg can be seen in Figure 2.2:

- Ply: refers to each one of the pre-preg cuts that come from a roll.
- Layer: refers to either set of fibre or uncured resin that conforms a pre-preg ply.

In this way, each ply has been considered to be composed by one fibre layer and two resin layers. This pre-preg model will be discussed in Chapter 6, along with an alternative model in which fibres and resin are considered well distributed during the whole compaction process.

## **2.2 Experimental measurements**

Several experiments related with the ultrasonic compaction and the materials used in the prototype will be presented next: First, the evolution of the temperature of the laminate during the compaction process; second, the cure kinetics of the resin of the laminate and; finally, the evolution of the viscosity with the temperature.

The results of the experiments presented in this section will be used in the next chapters to complete and/or validate the models developed.

## **2.2.1 Measurement of the evolution of the temperature during a static compaction process**

In order to validate the heat generation model and the thermomechanical solutions presented in next Chapters, an experiment done by AIRBUS [2.1] to measure the evolution of the temperature during the compaction process at a certain point in the laminate has been employed.

The experiment was designed to measure the temperature at a point of the laminate during a “static” process, i.e., the sonotrode only vibrates over the laminate but it is not moved along it.

In this case, the whole laminate is uncured and no previous compactions have been carried out during lamination. In this way, all resin layers will contribute to the heat generation. The experiment follows the compaction procedure described in Section 2.1.2 and the scheme shown in Figure 2.2.

The procedure by which the experiment has been carried out is the following:

- At first, after protecting the mould (in this case a flat metallic tool) with a demoulding layer, a peel-ply layer is placed over the mould to ensure that the laminate will be fixed to it during the lay-up forming process and during the ultrasonic compaction process.
- Secondly, 8 composite pre-preg plies are placed over the mould with an automatic tape lay-up (ATL) machine. The plies are placed one by one with the same fibre orientation.
- After the lay-up has been formed, the sonotrode is placed over the laminate and is turned on, inducing the ultrasonic vibration inside the resin of the composite plies.
- Finally, after 10 seconds of operation, the sonotrode is lifted.

In order to measure the temperature of the laminate during the compaction phase, a thermocouple was placed below the first composite ply, a time/temperature curve being obtained during the process.

The experimental curve given by the measurements of the thermocouple is shown in Figure 2.3.

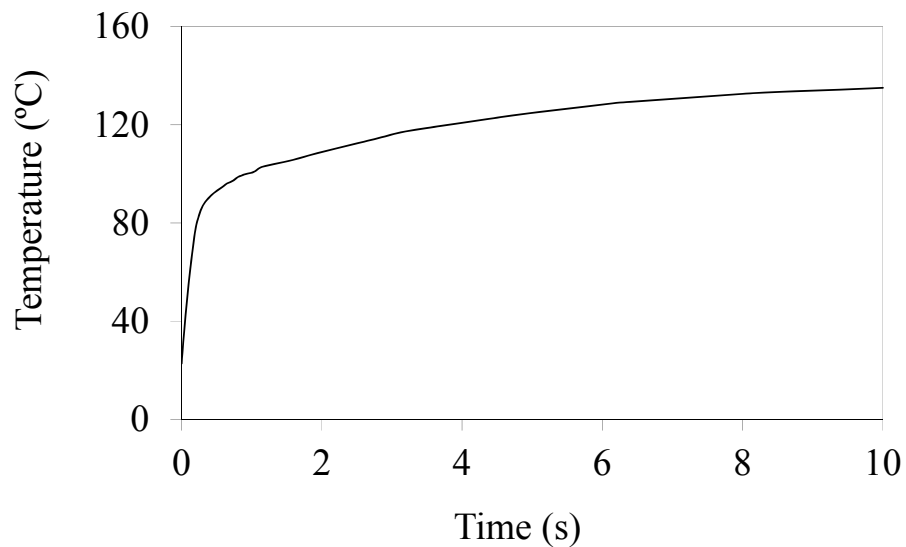


**Figure 2.3. Experimental temperature/time curve at the bottom of the laminate during the ultrasonic compaction process**

### **2.2.2 Measurement of the degree of cure to obtain the curing kinetics of the resin**

As the compaction process entails the heating of the resin, the possibility of partially curing the resin exists. This fact has to be controlled, because, in principle, it should be a negative effect. A model of the curing kinetic will be implemented in Chapter 4 in a thermal model to study the behavior of the material. In this way, the

evolution of the curing reaction of the resin has to be measured and will be presented next.

In order to describe the evolution of the polymerization of a resin, the most common parameter is the degree of cure. The way of obtaining experimentally this parameter is to measure the disappearance of the epoxy groups present in the resin (that allow the crosslink of the molecules). This disappearance of groups is commonly measured indirectly, using either thermal (through the heat flux needed to reach a certain temperature in the resin, in the differential scanning calorimetry technique) or optical properties (through the absorbance by the resin of certain wavelengths of an infrared light beam, in the Fourier transform infrared spectroscopy technique). The results of both techniques will be used in the curing model presented in Chapter 4, so they will be explained next.

#### Differential Scanning Calorimetry (DSC):

This technique is based on the measurement of the heat flux of a resin (that has been previously maintained at the polymerization temperature during a certain time) when a temperature increment is applied on it. This temperature increment is increased linearly with time. In this way, a curve heat flux/temperature or heat flux/time is obtained for the resin.

The process is repeated for several polymerization times of the resin and for a reference-uncured sample.

The principle of this method is that, to reach the same temperature, a cured sample needs less heat flux than the reference sample, due to the exothermicity of the curing process. Thus, the higher the degree of cure of the resin, the lower the heat flux needed and, in this way, the residual enthalpy (the area under the heat flux/temperature curve).

Once the curves heat flux/temperature for different stabilization times of the resin at the polymerization temperature are obtained, the degree of cure is measured comparing the residual enthalpy at each level with the total enthalpy of the reference sample.

A heat flux/temperature diagram is shown in Figure 2.4 [2.2, 2.3]. Three curves are shown, for resin samples exposed to the polymerization temperature during 0, 30 and 60 minutes, from top to bottom, respectively. It can be appreciated how the area under the curve is reduced on the way the samples have been exposed to the curing temperature during more time.

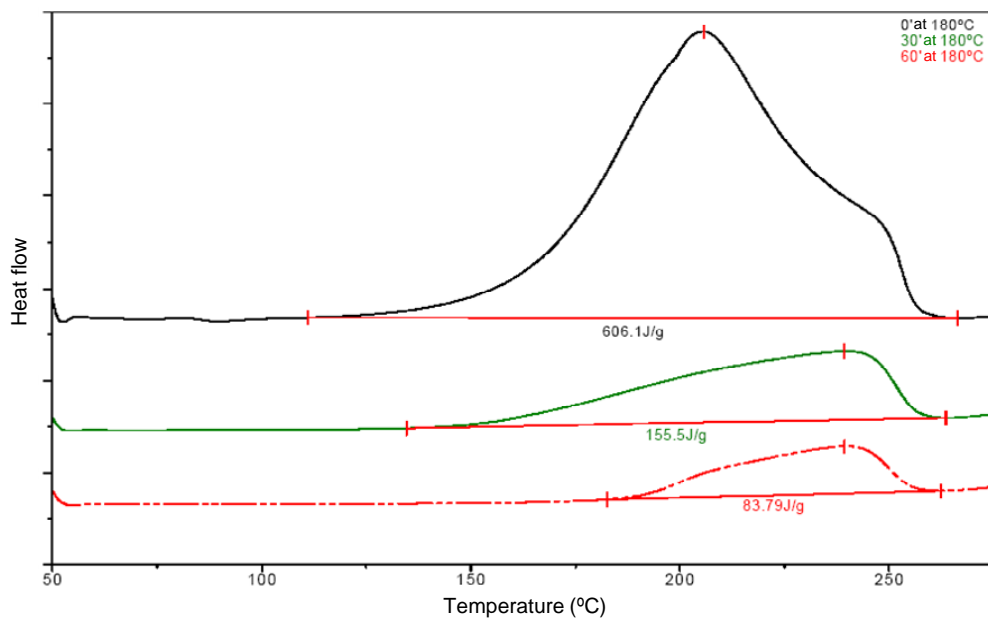


**Figure 2.4. Heat flux/temperature diagram of a resin, obtained with the DSC**

### Fourier transform infrared spectroscopy (FTIR):

In this system, the absorption of infrared light by the resin at a certain state of curing is evaluated for several wavelengths. The equipment plots an absorbance spectrum (a diagram wavelength/absorbance) in which the absorbance level of the infrared light corresponding to each wavelength are shown. These wavelengths correspond to the different components of the resin. In this way, studying the energy absorbed by each component for several cure states of the resin, it can be evaluated if the components are reacting and wasting or forming new components. An example of an absorbance spectrum of a resin for several cure cycles is shown in Figure 2.5, obtained from [2.4]. The  $x$  axis represents the wavelengths and the  $y$  axis the absorbance levels. The curves, from top to bottom, have been obtained for a resin that has been cured for 5 minutes, 30 minutes and 2 hours at 180 °C, respectively.

The most important band is the one located at  $4525\text{ cm}^{-1}$ , that corresponds to the epoxy group of the resin. This band presents great intensity, allowing its evolution to be studied even at high degrees of cure, where the curing is less reactive.

In order to normalize the results, the  $6005\text{ cm}^{-1}$  band is used, due to the fact that it remains constant during all the polymerization reaction. This band corresponds to the link C-H of the aromatic ring of the resin.

In the graph depicted in Figure 2.5, it can be appreciated how the peak of the  $4525\text{ cm}^{-1}$  band is reduced when the curing time evolves (from the top curve to the bottom one). At the same time, the peak that corresponds to the absorbance of the  $6005\text{ cm}^{-1}$  band remains unaltered in the different curves.

A kinetic model that allows the evolution of the degree of cure with temperature and time to be studied has been obtained in [2.5] for the resin analyzed in Figure 2.5, that will be the resin used in the present work. The variable used in the kinetic equations is  $R$  (absorbance ratio), defined as the quotient between the

absorbance of the band at  $6005\text{ cm}^{-1}$  ( $A_{6005}$ ) and the absorbance of the band at  $4525\text{ cm}^{-1}$  ( $A_{4525}$ ), measured with the FTIR. The equations that define this kinetic model are presented in Table 2.1. The variable  $R$  and, in this way, the kinetic model, will be related with the degree of cure in Chapter 4, using values measured with the DSC.

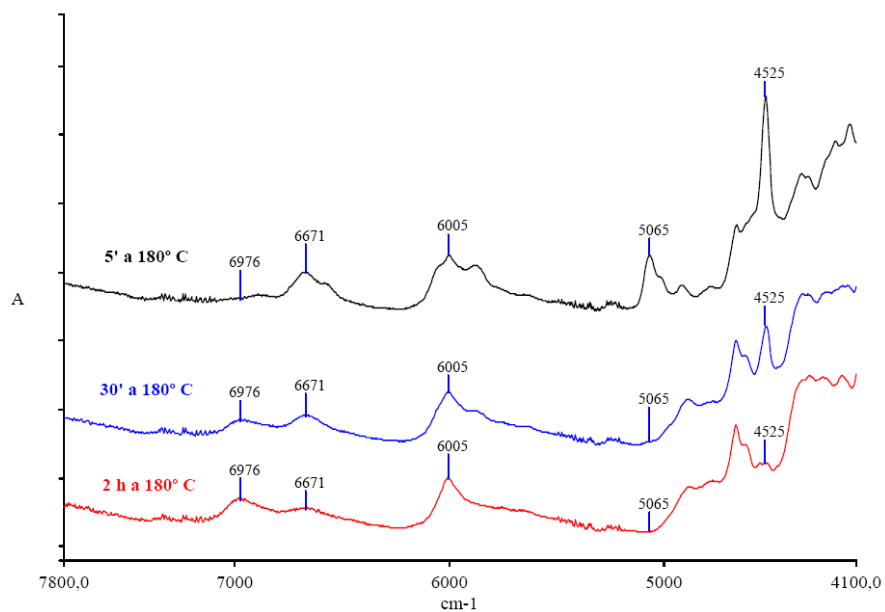


**Figure 2.5. Absorbance spectrum of a resin, measured with the FTIR**

The kinetic model consists on two different equations for each temperature, depending on the value of the variable  $R$ . An autocatalytic model has been assumed for low values of  $R$  and a controlled diffusion model is used for high values of  $R$ . These evolutions of the curing kinetic are similar to those used in other usual curing models, as the Scout model or the Lee, Chun and Lin model, as can be seen in [2.6].

Temperature	$R \leq 2$	$R \geq 2$
160 °C	$\frac{dR}{dt} = -0.029 + 0.105R - 0.063R^2 + 0.012R^3$	$\frac{dR}{dt} = 0.1884R^{-3}$
170 °C	$\frac{dR}{dt} = -0.048 + 0.157R - 0.095R^2 + 0.019R^3$	$\frac{dR}{dt} = 0.2508R^{-2.49}$
180 °C	$\frac{dR}{dt} = -0.086 + 0.261R - 0.151R^2 + 0.031R^3$	$\frac{dR}{dt} = 0.2809R^{-0.96}$
190 °C	$\frac{dR}{dt} = -0.126 + 0.411R - 0.281R^2 + 0.067R^3$	$\frac{dR}{dt} = 0.4851R^{-0.38}$
200 °C	$\frac{dR}{dt} = -0.093 + 0.278R - 0.119R^2 + 0.019R^3$	$\frac{dR}{dt} = 5.1059R^{-0.98}$

**Table 2.1. Equations of the curing model obtained from the experiments**

### 2.2.3 Evolution of the viscosity with the temperature

The evolution of the viscosity with the temperature is a key parameter in order to model the heat generation properly. The viscosity will vary during the process due to the variation of the temperature inside the resin. For this reason, it is important to obtain the evolution of the viscosity with the temperature.

This evolution has been obtained by AIRBUS experimentally using a viscosimeter. In this experiment, a bar is rotated inside the resin and the torque needed to achieve the rotation movement is measured. During the rotation, the temperature of the resin is raised with a certain heating rate (measured in °C/min). In this way, the torque is related with the viscosity of the resin and a curve viscosity/temperature is obtained.

The experiment has been done for several heating rates and the resulting curves are presented in Figure 2.6.

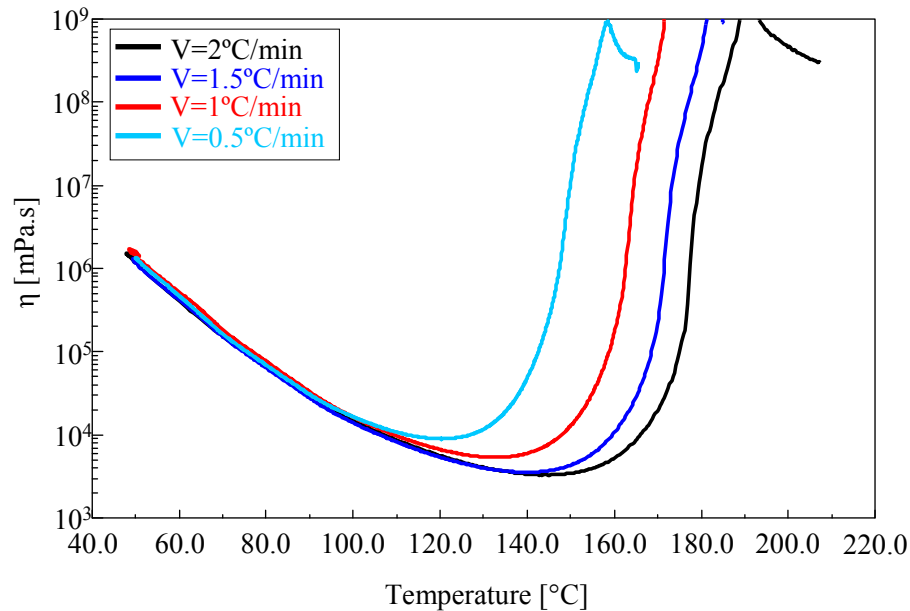


**Figure 2.6. Evolution of the viscosity with the time for several values of the heating rates**

It is important to note that the heating rates that can be applied in the viscosimeter are much lower than those the ultrasonic compactor can induce in the resin. Thus, an approximation will be done in Chapter 4, in the section concerning the modelling of the viscosity as a function of the temperature.

## Bibliography

- [2.1] Seebacher, S., *Contributions to the investigation of in-situ ultrasonic tape lamination of composite thermoset prepregs*. Master thesis at the Private fachhochschule Göttingen, 2008.

- [2.2] Um, M.-K., Isaac M. Daniel, I.M., Hwang, B.-S., *A study of cure kinetics by the use of dynamic differential scanning calorimetry*. Composites Science and Technology, Vol. 62, pp. 29–40, 2002.
- [2.3] Lisperguer, J., Droguett, C., *Caracterización del curado de resinas urea formaldehído por calorimetría diferencial de barrido (DSC)*. Boletín de la Sociedad Chilena de Química, Vol.47, No.1, 2002.
- [2.4] *FTIR modeling on MIHEXCEL 8552*. EADS-CASA, Report, 1999.
- [2.5] Sánchez-Blázquez, A., *Aplicación de la espectroscopía infrarroja y el análisis térmico en la monitorización de la polimerización de resinas termoestables utilizadas en la industria aeronáutica*. EADS-CASA, Report.
- [2.6] *MSC.MARC/MENTAT product documentation*. MSC.Software Documentation, 2006.

# *Chapter 3*

## *Problems under study*

To study the problem of the heat generation and the temperature distribution in the composite laminate subjected to ultrasonic vibrations two models are necessary: one thermomechanical and one thermal. The thermomechanical model is needed to estimate the heat generated due to the internal viscosity of the resin when an ultrasonic vibration is applied on it and will be developed in Chapter 5. The thermal model is needed to obtain the heat distribution within the laminate. A general description of the geometry and heats that are involved in the thermal model will be presented next, being extended and particularized in next Chapters.

The general parameters that define the problems studied in next Chapters will be posed in the following sections.

Two main problems are studied:

- The compaction of a composite laminate when the sonotrode is not moved along it. In this case, the sonotrode only vibrates over the laminate.
- The compaction of a composite laminate when the sonotrode is moved along it. In this case, the sonotrode vibrates and is displaced along the laminate at a certain velocity.

It is important to remark that, for both problems, all the composite plies are considered uncured.

The following descriptions of the problems will be similar for both compaction procedures. Firstly, a definition of the geometry of the problems will be done. Secondly, the boundary conditions concerning each problem are going to be posed. Finally, the heats involved in the process will be described.

The coordinate system for both problems is defined by: The mould where the laminate is laid-up is content in the  $x$ - $z$  plane. The composite plies are placed along the  $x$  direction,  $y$  being the direction of the thickness. It is supposed in the models that the problem is uniform along the  $z$  direction, the plane  $x$ - $y$  being the plane of study.

### 3.1 Transient problem

The problem of the compaction of a composite laminate when the sonotrode is not moved along it will be described in this section. The problem is studied since the sonotrode begins to actuate until reaching a certain process time. In these

conditions, the temperature evolves in time, so this compaction process will be treated as a transient problem.

### 3.1.1 Geometry definition

The scheme of Figure 3.1 shows the geometry of the problem under study [3.1]. The first, 1, and the last,  $n$ , plies and an intermediate ply,  $i$ , have been depicted. The central zone,  $L_s$ , is where the sonotrode actuates over the laminate (Note that the sketch is not at scale,  $H \approx 1$  mm,  $L_s \approx 20$  mm,  $L \approx 60$  mm).

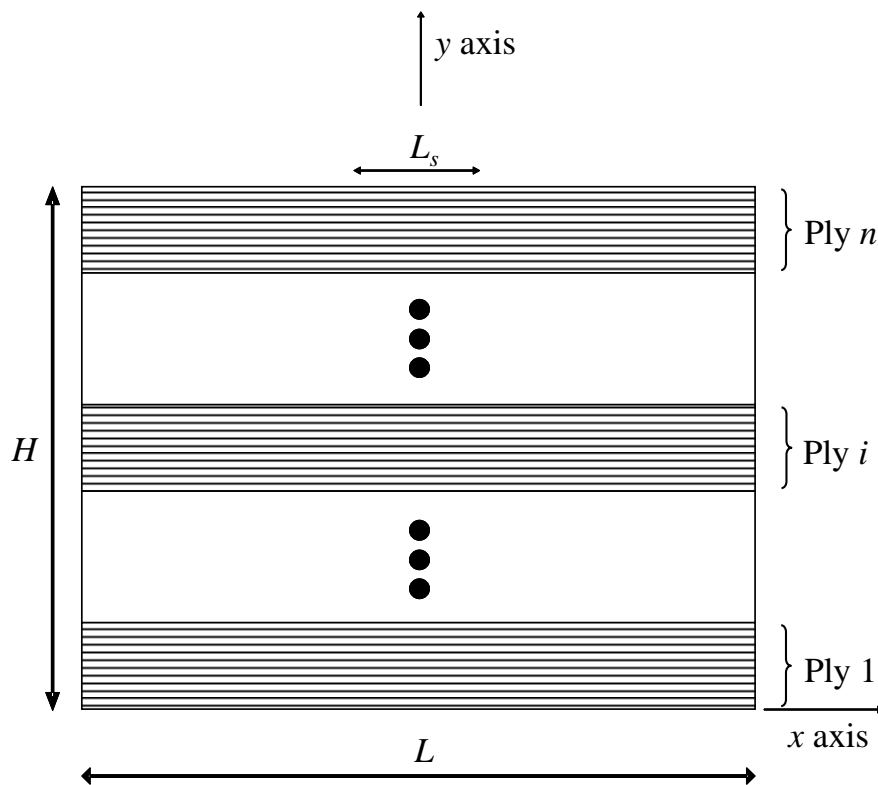


Figure 3.1. Scheme of the problem for the thermal model

### 3.1.2 Boundary conditions

The general boundary conditions of the problem are described next:

- For the left boundary of the laminate ( $x = -\frac{1}{2}L$ ,  $0 < y < H$ ): The laminate is free, in contact with the air.
- For the right boundary of the laminate ( $x = \frac{1}{2}L$ ,  $0 < y < H$ ): The laminate is free, in contact with the air.
- For the bottom boundary of the laminate ( $-\frac{1}{2}L < x < \frac{1}{2}L$ ,  $y = 0$ ): A peel ply layer is located under the laminate [3.1, 3.2], this peel ply layer having a very low conduction coefficient. An adiabatic condition is assumed in this zone.
- For the top center boundary of the laminate ( $-\frac{1}{2}L_s < x < \frac{1}{2}L_s$ ,  $y = H$ ): The laminate is in contact with the sonotrode.
- For the top right and left boundaries of the laminate ( $-\frac{1}{2}L < x < -\frac{1}{2}L_s$ ;  $\frac{1}{2}L_s < x < \frac{1}{2}L$ ,  $y = H$ ): The laminate is free, in contact with the air.

The initial condition of the problem is that, at time  $t = 0$ , all the points of the laminate and the sonotrode are at room temperature.

### 3.1.3 Heats involved in the compaction process

The heat flows that take place during the compaction process when the sonotrode is not moved along the laminate are:

- Conduction between the layers.

- Conduction within each layer.
- Conduction between the top pre-preg ply and the titanium tip of the sonotrode, at  $(-\frac{1}{2}L_s < x < \frac{1}{2}L_s, y = H)$ .
- Convection between the top pre-preg ply and the air, at the zones of the laminate that are not placed under the sonotrode. These zones are described by  $(-\frac{1}{2}L < x < -\frac{1}{2}L_s, y = H)$  and  $(\frac{1}{2}L_s < x < \frac{1}{2}L, y = H)$ .

Outside the area where the heat is generated, far enough from the zone of the laminate where the sonotrode is applied,  $(x = -\frac{1}{2}L, 0 < y < H)$  and  $(x = \frac{1}{2}L, 0 < y < H)$ , the temperature of the laminate will not be affected by the heat generation, so the heat fluxes are considered equal to zero (the temperature of the laminate in these zones is equal to the room temperature).

The conduction between the bottom resin layer and the mould where it is placed  $(-\frac{1}{2}L < x < \frac{1}{2}L, y = 0)$  has been assumed to be negligible, due to the adiabatic character of the peel-ply layer placed between them.

Radiation effects are supposed null compared with the heat conduction and convection. Anyway, the zone of interest is the material being compacted, that is located under the sonotrode, and no radiation effects will happen in this zone.

The heat generated due to the ultrasonic vibration is considered to take place in the zone of the laminate just under the sonotrode, at  $(-\frac{1}{2}L_s < x < \frac{1}{2}L_s, 0 < y < H)$ .

## 3.2 Stationary problem

The real functioning of the prototype that lays-up, compact and cure the plies will entail the movement of the sonotrode throughout the part to be compacted. As all the points experience the same thermal history, this problem can be considered stationary in the sonotrode frame.

### 3.2.1 Geometry definition

The scheme of Figure 3.2 shows the geometry of the problem under study [3.1]. The first, 1, and the last,  $n$ , plies and an intermediate ply,  $i$ , have been depicted. The zone where the sonotrode actuates over the laminate has been marked as  $L_s$ .

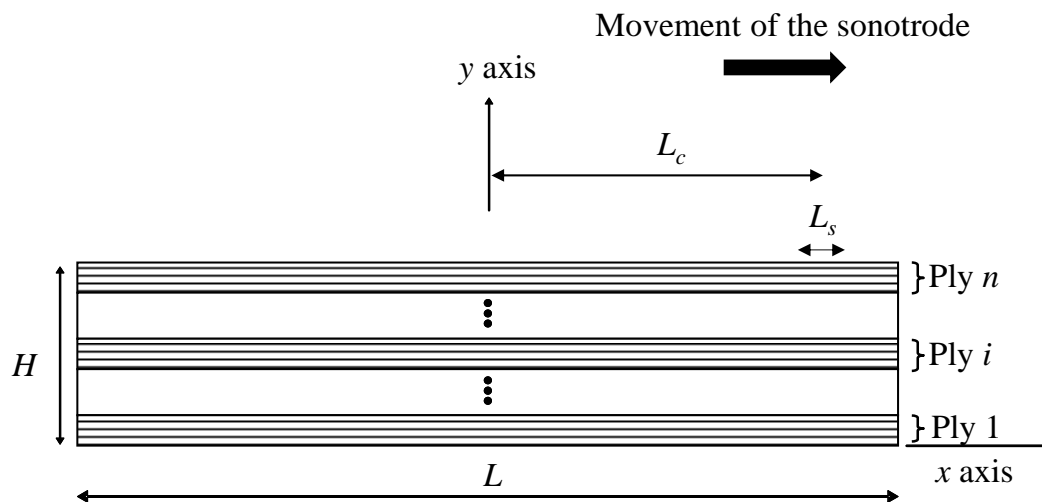


**Figure 3.2. Scheme of the problem for the thermal model**

The parameter  $L_c$  defines the distance between the center of the sonotrode and the center of the laminate.

Note that, as happened in the previous section, the sketch is not at scale,  $H \approx 1$  mm,  $L_s \approx 20$  mm,  $L \approx 3000$  mm

It has to be noticed that, in this case, the geometry is not symmetrical with respect to the  $y$  axis. At the right of the sonotrode the zone affected by the temperature increment will be small but, at the left zone, all the material has been heated previously, so a certain length is needed to study the cooling of this zone. These assertions will be checked in Chapter 9.

### 3.2.2 Boundary conditions

The general boundary conditions of the problem are described next:

- For the left boundary of the laminate ( $x = -\frac{1}{2}L$ ,  $0 < y < H$ ): The laminate is free, in contact with the air.
- For the right boundary of the laminate ( $x = \frac{1}{2}L$ ,  $0 < y < H$ ): The laminate is free, in contact with the air.
- For the bottom boundary of the laminate ( $-\frac{1}{2}L < x < \frac{1}{2}L$ ,  $y = 0$ ): A peel ply layer is located under the laminate [3.1, 3.2], having this peel ply layer a very low conduction coefficient. An adiabatic condition is assumed in this zone.
- For the top center boundary of the laminate ( $L_c - \frac{1}{2}L_s < x < L_c + \frac{1}{2}L_s$ ,  $y = H$ ): The laminate is in contact with the sonotrode.
- For the top right and left boundaries of the laminate ( $-\frac{1}{2}L < x < L_c - \frac{1}{2}L_s$ ;  $L_c + \frac{1}{2}L_s < x < \frac{1}{2}L$ ,  $y = H$ ): The laminate is free, in contact with the air.

### 3.2.3 Heats involved in the compaction process

The heat flow rates involved in the problem are:

- Conduction between the layers.
- Conduction within each layer.
- Conduction between the top pre-preg ply and the titanium tip of the sonotrode, at  $(L_c - \frac{1}{2}L_s < x < L_c + \frac{1}{2}L_s, y = H)$ .
- Convection between the top pre-preg ply and the air, at the zones of the laminate that are not placed under the sonotrode. These zones are described by  $(x < L_c - \frac{1}{2}L_s, y = H)$  and  $(L_c + \frac{1}{2}L_s < x, y = H)$ .

Outside the area where the heat is generated, far enough from the zone of the laminate where the sonotrode is applied,  $(x = -\frac{1}{2}L, 0 < y < H)$  and  $(x = \frac{1}{2}L, 0 < y < H)$ , the temperature of the laminate will not be affected by the heat generation, so the heat fluxes are considered equal to zero (the temperature of the laminate in these zones is equal to the room temperature).

The conduction between the bottom resin layer and the mould where it is placed  $(-\frac{1}{2}L < x < \frac{1}{2}L, y = 0)$  has been assumed to be negligible, due to the adiabatic character of the peel-ply layer placed between them.

Radiation effects are supposed null compared with the heat conduction and convection. In this case, the radiation can appear in the zone that is being cooled down, at the left of the sonotrode but, anyway, as in the previous problem, the zone of interest is the material being compacted, that is located under the sonotrode, so no radiation effects will happen in this zone.

The heat generated due to the ultrasonic vibration is considered to take place in the zone of the laminate just under the sonotrode, at  $(L_c - \frac{1}{2}L_s < x < L_c + \frac{1}{2}L_s, 0 < y < H)$ .

Finally, an extra convective heat will be introduced in the formulation, inside the composite layers, in order to take into account the effect of the horizontal velocity displacement of the sonotrode. This fact will be explained in Chapter 9.

### 3.3 Conclusions

The general parameters that define the compaction procedures that will be analyzed in next Chapters have been posed.

The main difference in the procedures is the possibility of moving (or not) the sonotrode along the laminate. If the sonotrode is moved, the compaction process will be analyzed as a steady-state problem and, if the sonotrode is not moved, the problem will be analyzed as a transient one.

In both cases, the geometry, the boundary conditions and the heats that are involved in the processes have been shown.

### Bibliography

- [3.1] Seebacher, S., *Contributions to the investigation of in-situ ultrasonic tape lamination of composite thermoset prepregs*. Master thesis at the Private fachhochschule Göttingen, 2008.
- [3.2] Campbell, F.C., *Manufacturing Processes for Advanced Composites*. ELSEVIER, 2003.



# *Chapter 4*

## *Initial models*

Prior to study the heat generation inside the laminate due to the internal viscosity of the resin, several analyses have been done, in order to obtain a better knowledge of how the material behaves during the compaction process.

In this case, a static compaction process will be considered, in which the sonotrode is placed over the laminate and vibrates, although it is not moved along the composite.

The following thermal and curing models have been solved implementing them in the FEM commercial program MSC.Marc/Mentat<sup>®</sup> [4.1], due to its possibilities of implementing curing kinetics in thermomechanical analyses.

First, an estimation of the temperature distribution inside the laminate will be done with a FEM thermal model, using as an input the experimental measurement of the temperature in the sonotrode. This estimation will allow the validity of the thermal properties given in the literature [4.3] to be checked.

Second, the model presented in the previous section will be coupled with a curing model, in order to check if the resin achieves a representative degree of cure during the ultrasonic compaction process (due to the heat generated in the process).

Third, from the results of the previous models and curves obtained from experiments, the evolution of the viscosity of the resin with the temperature will be obtained. This evolution will be necessary in the following chapters, for the modelling of the heat generation.

## **4.1 Estimation of the temperature in the laminate**

As mentioned before, the quality of the compaction depends on the debulking of the plies. The air between plies has to be removed properly. This will occur if the resin is fluid enough and this fluidization will occur if the temperature in the laminate is raised during enough time.

With the present model, the analysis of the heat flux and the temperatures reached in the composite laminate, using some data from the measurements made during the ultrasonic compaction process, is attempted.

This is a previous model made to check that, with the properties available, the temperature in the laminate can be controlled without placing thermocouples on

it. It can be achieved by comparing this model with the curve obtained in the experiment presented in Section 2.2.1. However, it cannot be assured that the comparison will reveal satisfactory results because the experiment is made on uncured material and the properties employed in the model have been measured on cured material.

The hypotheses made and the implementation of the model will be detailed first. Then the results obtained with the model will be presented, finishing this section with a comparison with experimental results.

#### 4.1.1 Description, hypotheses and implementation of the thermal model

In this model, only the titanium tip and the laminate that is compacted will be considered, excluding the modelling of the tool where the composite material is placed, as can be seen in Figure 4.1. The tool will be substituted by an isolation condition due to the peel ply layer placed over it, as mentioned before.

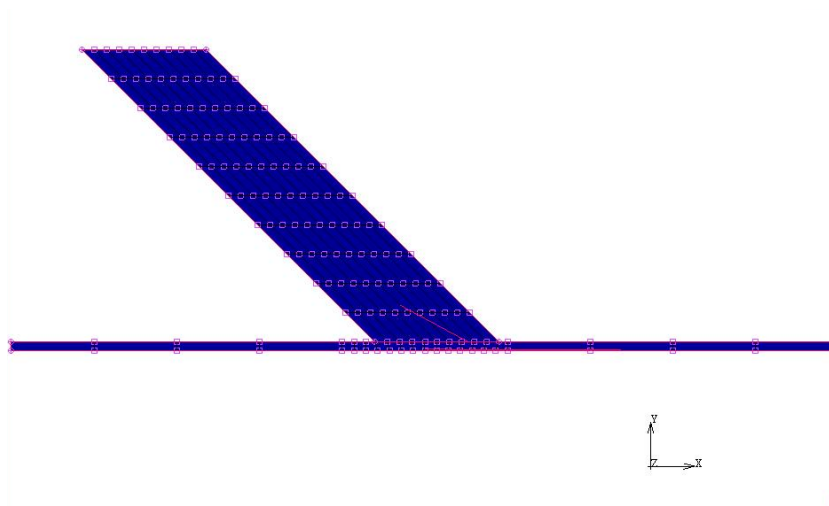


Figure 4.1. FEM thermal model

The dimensions of the model are:

- Length of the laminate,  $L = 130$  mm.
- Thickness of the laminate,  $H = 1.04$  mm.
- Length of the contact zone of the sonotrode,  $L_s = 20$  mm.
- Height of the sonotrode,  $H_s = 45$  mm.

The heat exchanges assumed in this model are:

- Conduction between the sonotrode and the composite laminate
- Convection between the sonotrode and the environment
- Convection between the composite laminate and the environment

As mentioned in Chapter 3, radiation effects have been neglected compared with the heat conduction and convection.

The temperature at the tip of the sonotrode (at the contact zone with the laminate) will be fixed and assumed to be known, letting the temperature of the laminate to evolve freely.

The material that will be compacted consists of 8 plies laid up following the stacking sequence  $(0)_8$ , the  $0^\circ$  direction being coincident with the  $x$  axis of Figure 4.1 and the lay-up direction coincident with the  $y$  axis of the same figure.

The problem has been solved as a 2D problem. The validity of this approximation will be analyzed in Chapter 6.

The main properties of the materials (density,  $\rho$ , heat capacity at constant pressure,  $c_p$ , and conductivity,  $k$ ) [4.3] used in the FEM model are shown in Table 4.1.

Material	$\rho \left[ \frac{kg}{m^3} \right]$	$c_p \left[ \frac{J}{kgK} \right]$	$k \left[ \frac{W}{mK} \right]$
Titanium	4430	580	7,1
Composite material	1570	1180	0,6 (transversal) 1 (longitudinal)

**Table 4.1. Thermal properties of the materials**

A detailed view of the contact zone between the sonotrode and the laminate is shown in Figure 4.2. The node whose temperature will be followed during the compaction process has been marked with a red circle.

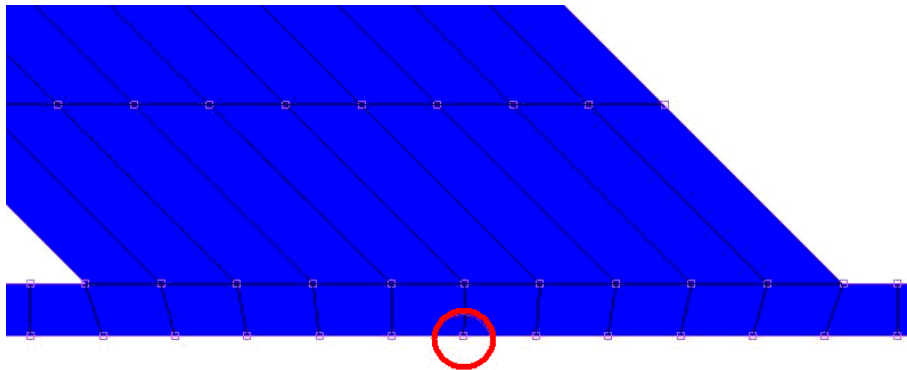


**Figure 4.2. Detailed view of the contact zone between the sonotrode and the laminate**

As can be appreciated, Figure 4.2, a congruent mesh has been used, in order to obtain a smooth transition in the heat transfers.

The problem under study is a static test, as mentioned in the experimental measurements of section 2.2.1 and is formulated as follows: initially, the two bodies remains in contact at room temperature (Figure 4.3). The temperature of the interface sonotrode tip/laminate is raised, transferring the heat to the laminate and to

the sonotrode. The free faces of the laminate and the sonotrode interchange heat with the air through convection.

The raise of the temperature has been modeled using two straight lines (Figure 4.3), based on punctual measurements made at the sonotrode tip. The first line has a very high slope (the temperature is increased up to 100 °C in less than a second) whereas the second line presents a lower slope (as will be checked in Chapter 6, reaching the maximum temperature, the heat generated decreases).

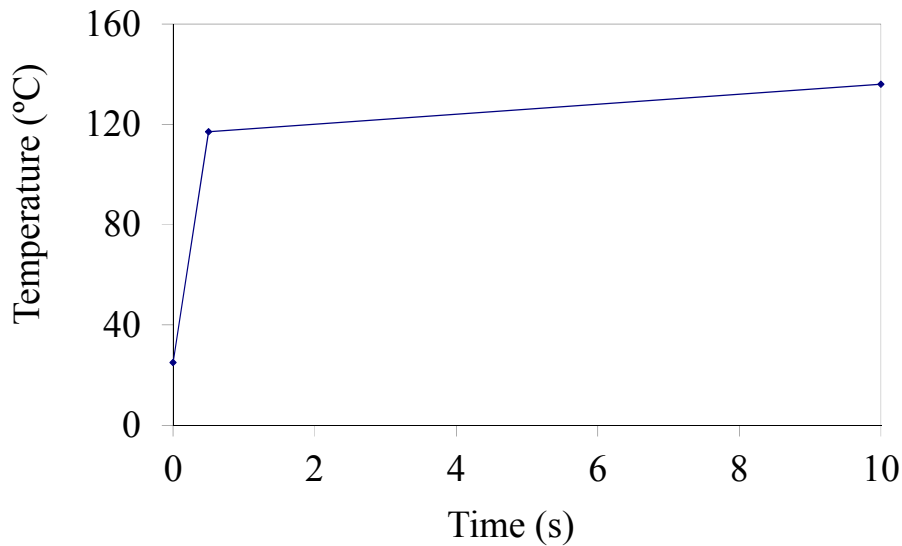


**Figure 4.3. Temperature evolution imposed to the sonotrode tip to evaluate the temperature field in the thermal model**

## 4.1.2 Results

Once the FEM model has been solved, the results obtained are analyzed next.

The evolution of the temperature with the time has been measured at the node marked in Figure 4.2 with a red circle (in order to compare, later, with the experimental results). This evolution is depicted in Figure 4.4.

As expected, a fast initial temperature increment is obtained, in almost 2 seconds 120 °C are reached. After that the temperature raise is slower, until reaching the end of the compaction process.

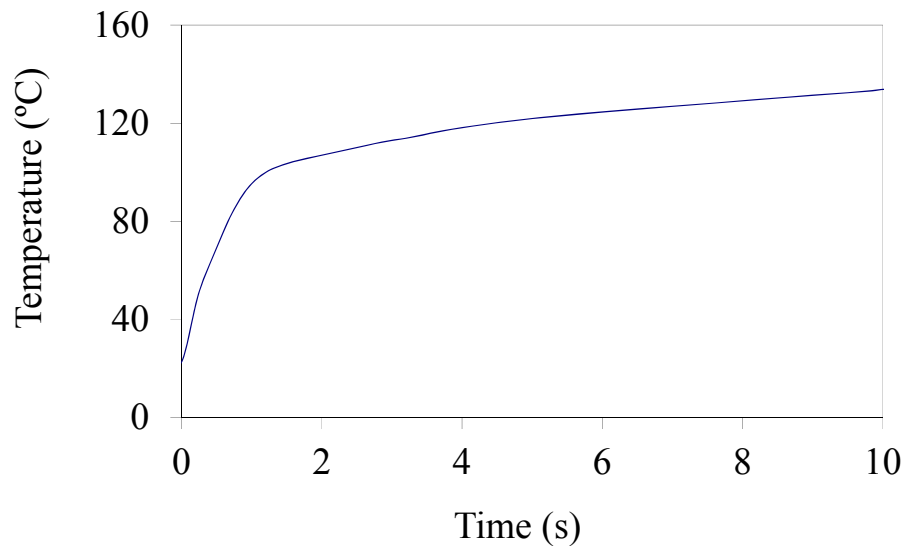


**Figure 4.4. Temperature vs time curve, obtained with the thermal model for a static compaction, at a node situated at  $(x=0, y=0)$**

The temperature distribution inside the laminate can be appreciated in Figure 4.5. It has been obtained at the end of the process, for a time of 10 seconds. The scale of the temperature shown is in Kelvin.

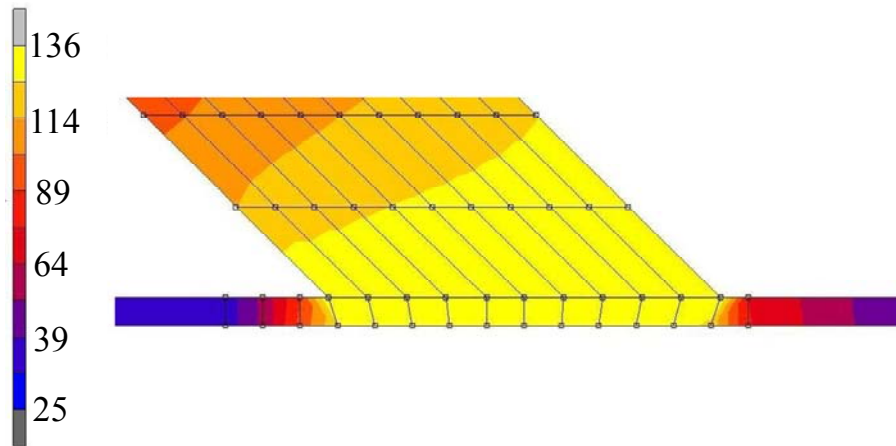


**Figure 4.5. Temperature field inside the laminate during the static ultrasonic compaction process (in Kelvin)**

### 4.1.3 Experimental validation

In order to validate the model, the results obtained in Figure 4.4 are compared with the experimental results presented in Section 2.2.1. This comparison is shown in Figure 4.6.

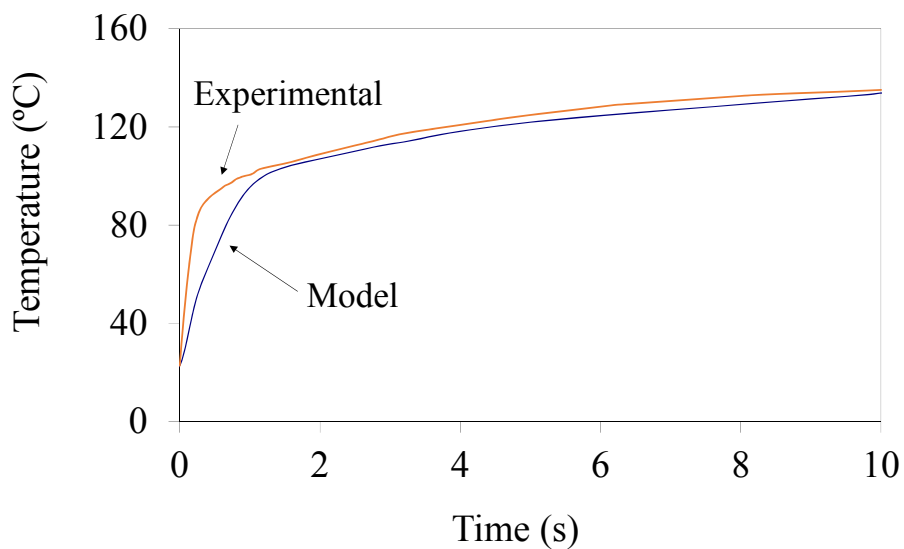


**Figure 4.6. Comparison of the thermal FEM model results with experimental measurements**

Figure 4.6 shows a reasonably good agreement between the thermal FEM model and the experimental results, validating the properties given in the bibliography [4.3].

## **4.2 Evaluation of the possible curing of the resin during the compaction process**

The aim of this model is to check if the heating associated to the vibration can advance the curing of the resin. To this end, a curing model for the resin that forms the matrix of the composite has been developed. This curing model has been coupled with the thermal FEM model described in section 4.1, obtaining as a result the evolution of the degree of cure of the resin during the compaction process. As mentioned at the beginning of this Chapter, this curing model has also been implemented in the commercial FEM program MSC.Marc/Mentat<sup>®</sup>.

Due to the coupled nature of the curing process between the temperature and the degree of cure, an incremental algorithm to solve this process will be presented first. Then, the equations that represent the curing kinetics will be posed. Finally, the results obtained with this model will be shown.

### **4.2.1 Algorithm to calculate the degree of cure**

The present model has been developed to obtain the evolution of the degree of cure of the resin with the temperature during the compaction process. The temperature distribution inside the laminate will be given by the thermal FEM model presented in section 4.1.

The degree of cure ( $\alpha$ ) is defined here as the relative difference between the quantity of epoxy groups existing initially ( $E_0$ ) and the quantity of epoxy groups existing in a certain moment ( $E_i$ ). The degree of cure can there-by be expressed as:

$$\alpha = 1 - \frac{E_i}{E_0} \quad (4.1)$$

The value of the degree of cure varies in the range  $0 \leq \alpha \leq 1$ .

The evolution of the degree of cure along the compaction process will be obtained using an incremental algorithm. The steps of the algorithm are:

Step 1: the degree of cure ( $\alpha_i$ ) and the temperature ( $T_i$ ) of the resin are assumed known at a certain time  $i$ .

Step 2: the curing model (that will be presented next) is used to estimate the variation of the degree of cure with the time ( $\frac{d\alpha_i}{dt}$ ).

Step 3: the degree of cure at the next time step  $i + 1$  is calculated using:

$$\alpha_{i+1} = \alpha_i + \frac{d\alpha_i}{dt} \Delta t \quad (4.2)$$

where  $\Delta t$  is the length of the time step.

Step 4: the heat generated due to curing ( $Q_i^c$ ) is calculated using

$$Q_i^c = \frac{d\alpha_i}{dt} (1 - V_f) \rho_r H_r \quad (4.3)$$

where  $V_f$  is the volumetric fraction of fibers,  $\rho_r$  is the density of the resin and  $H_r$  is the total heat of reaction of the resin [4.2].

Step 5: the heat generated calculated in step 4 is included in the thermal model presented in section 4.1 to solve the thermal problem during the time step, obtaining the temperature field at the next time step,  $T_{i+1}$ .

The algorithm returns to Step 1 until reaching the end of the process time.

A scheme of the algorithm is presented in Figure 4.7.

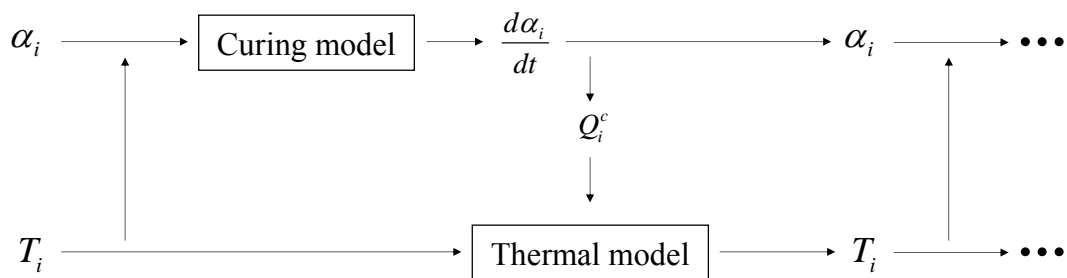


**Figure 4.7. Scheme of the algorithm used to estimate the degree of cure during the compaction process**

In order to initialize the algorithm, an initial value of  $\alpha$ , different to 0, has to be chosen. In this case, as indicated in the bibliography [4.1], a value of 0.0002 has been chosen.

### 4.2.2 Curing model

In this section, the model that represents the curing kinetics of the resin will be presented. The model is obtained from the experimental results presented in Section 2.2.2 of Chapter 2.

In the experimental measurements made with the FTIR [4.6], the expressions of the curing kinetics were given to obtain the absorbance relation  $R$ . Note that  $R$  was defined as the ratio between the absorbance of the  $6005\text{ cm}^{-1}$  band ( $A_{6005}$ ) and the absorbance of the  $4525\text{ cm}^{-1}$  band ( $A_{4525}$ ), measured with the FTIR.

In order to implement this curing kinetics into the FEM program, they have to be expressed in terms of the degree of cure  $\alpha$ . The parameter  $R$  can be related with the degree of cure from the results of the FTIR and the DSC [4.5] using the curve presented in Figure 4.8, extracted from [4.4].

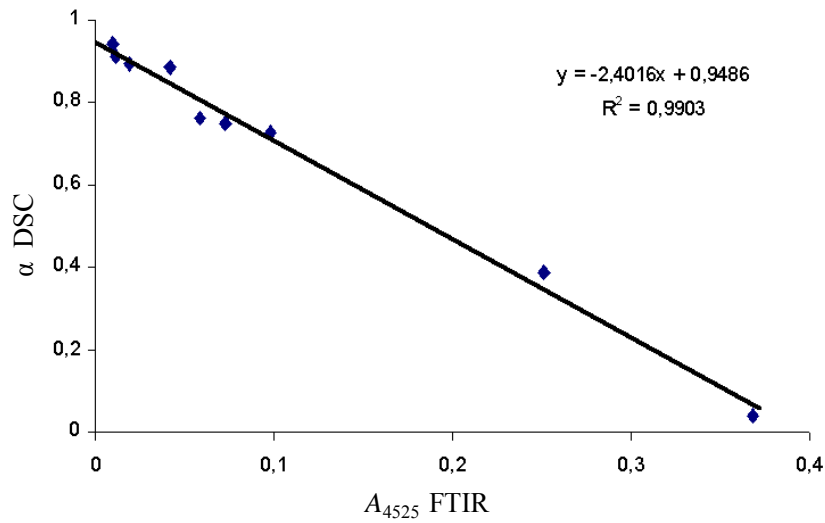


**Figure 4.8. Curve to relate the measurements of the FTIR (horizontal axis) and the DSC (vertical axis)**

From the regression line used to fit the results of Figure 4.8, the expression (4.4) can be obtained:

$$\alpha = -2.4016A_{4525} + 0.9846 \quad (4.4)$$

The parameter  $R$  can be expressed as:

$$R = \frac{A_{6005}}{A_{4525}} \quad (4.5)$$

Substituting equation (4.5) in (4.4), the expression that relates  $\alpha$  and  $R$  is obtained:

$$R(\alpha) = \frac{-2.4016A_{6005}}{\alpha - 0.9846} \quad (4.6)$$

Using equation (4.6), the expressions that define the curing kinetics presented in Table 2.1 of section 2.2.2 can be expressed in terms of  $\alpha$ . These expressions are shown in Table 4.2, where:

$$A_{6005} = 0.1654 ; J(\alpha) = \frac{(\alpha - 0.9846)^2}{2.4016A_{6005}} \quad (4.7)$$

<b>T (°C)</b>	$\alpha \leq 0.75$	$\alpha \geq 0.75$
160	$\frac{d\alpha}{dt} = J(\alpha)(-0.029 + 0.105R(\alpha) - 0.063R(\alpha)^2 + 0.012R(\alpha)^3)$	$\frac{d\alpha}{dt} = J(\alpha)(0.1884R(\alpha)^{-3})$
170	$\frac{d\alpha}{dt} = J(\alpha)(-0.048 + 0.157R(\alpha) - 0.095R(\alpha)^2 + 0.019R(\alpha)^3)$	$\frac{d\alpha}{dt} = J(\alpha)(0.2508R(\alpha)^{-2.49})$
180	$\frac{d\alpha}{dt} = J(\alpha)(-0.086 + 0.261R(\alpha) - 0.151R(\alpha)^2 + 0.031R(\alpha)^3)$	$\frac{d\alpha}{dt} = J(\alpha)(0.2809R(\alpha)^{-0.96})$
190	$\frac{d\alpha}{dt} = J(\alpha)(-0.126 + 0.411R(\alpha) - 0.281R(\alpha)^2 + 0.067R(\alpha)^3)$	$\frac{d\alpha}{dt} = J(\alpha)(0.4851R(\alpha)^{-0.38})$
200	$\frac{d\alpha}{dt} = J(\alpha)(-0.093 + 0.278R(\alpha) - 0.119R(\alpha)^2 + 0.019R(\alpha)^3)$	$\frac{d\alpha}{dt} = J(\alpha)(5.1059R(\alpha)^{-0.98})$

**Table 4.2. Equations of the curing model in terms of  $\alpha$**

The two expressions used to describe the curing kinetics at each temperature are not continuous. Supposing that this fact could introduce errors when implementing the equations into the FEM program, a lineal transition between the

expressions has been chosen. The first expression has been assumed for the interval  $0 \leq \alpha \leq 0.73$  and the second expression for  $\alpha \geq 0.77$ , using a straight line to describe the interval  $0.73 \leq \alpha \leq 0.77$ .

A representation of the curves and the approximation made can be seen in Figure 4.9, where a graph degree of cure versus variation of the degree of cure with the time is presented.

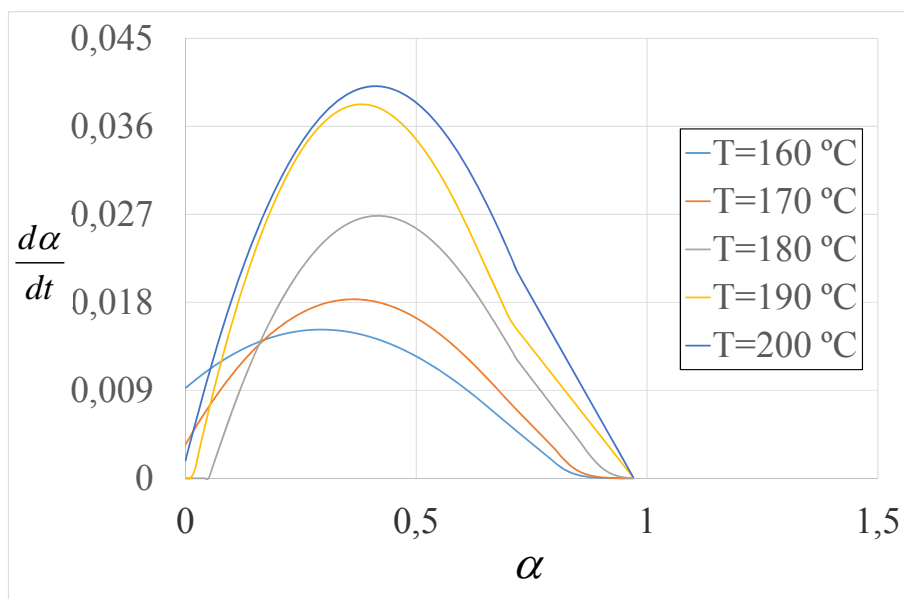


**Figure 4.9. Representations of the cure kinetics as degree of cure/variation of the degree of cure with the time for several values of the temperature**

It can be seen that the transition made between the equations for  $\alpha \approx 0.75$  is almost inappreciable.

In order to better appreciate the curing kinetics, a 3D representation is shown in Figure 4.10.

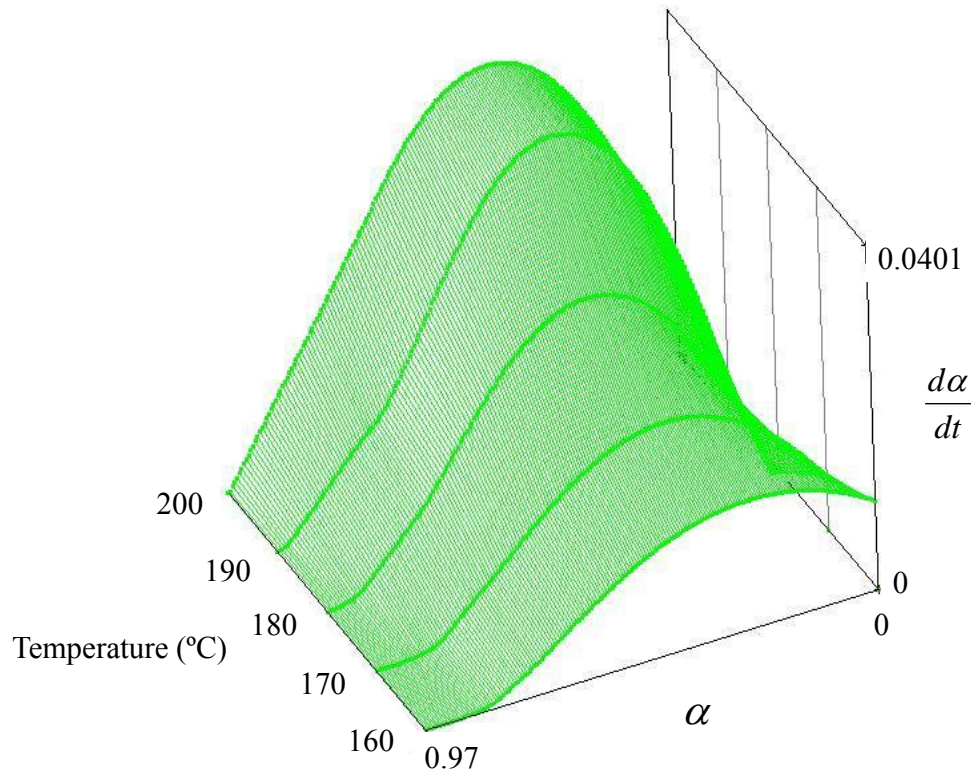


**Figure 4.10. 3D representation of the cure kinetics**

The model proposed is representative for temperatures between 160 °C and 200 °C. As seen in the experiments shown in Chapter 1, the temperature during the compaction process is lower than 140 °C. As there is no information of the curing kinetics for temperatures below 160 °C, the evolution between 0 °C and 160 °C will be supposed.

Observing the evolution of the viscosity in the experimental results of Chapter 1, it is supposed that the resin will not begin to react until reaching 120 °C and, then a smooth reaction will happen. With this data, the evolution is proposed as:

- From 0 °C to 120 °C: the resin is supposed to not react, so the variation of the degree of cure will remain equal to 0.

- From 120 °C to 160 °C: a linear evolution from 0 to the value at 160 °C for the variation of the degree of cure is assumed. This assumption is supposed to provide higher values than in the real behavior, because, in the real case, the evolution should be smoother.

The curing kinetic of the model with the described assumptions is shown in the 3D representation of Figure 4.11.

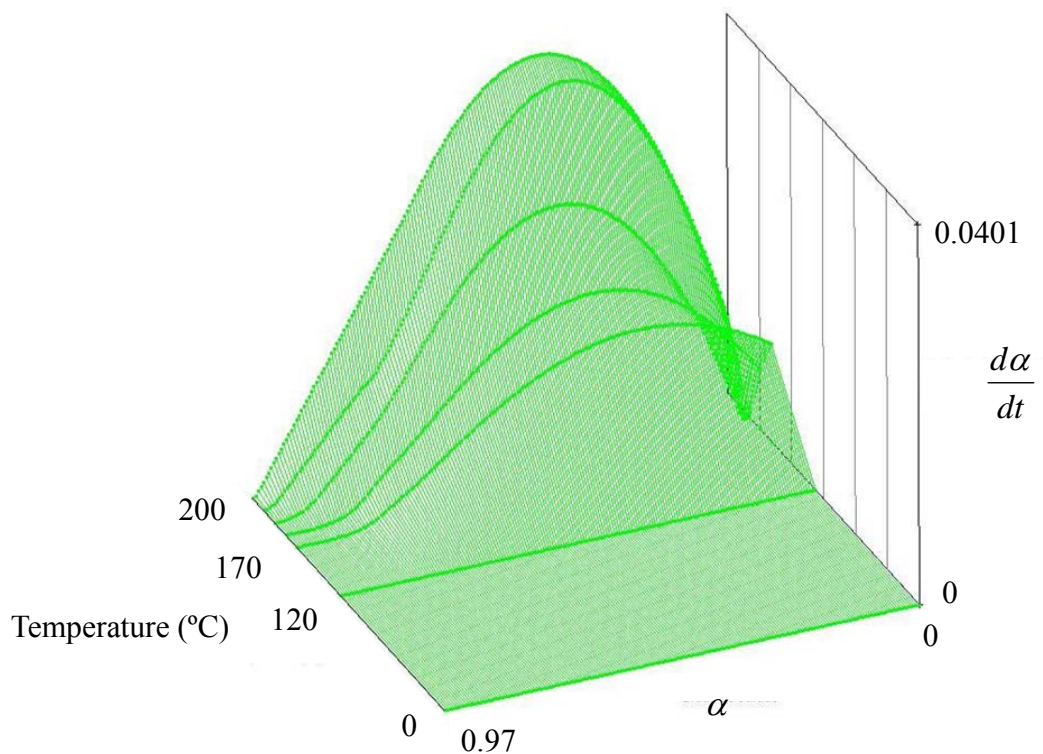


**Figure 4.11. Model of the curing kinetics from 0° to 200 °C**

### 4.2.3 Results of the curing model

The results obtained with the curing model are shown next. As mentioned before, the curing model has been implemented in the commercial FEM program MSC.Marc/Mentat. The type of analysis used is a thermomechanical one, the thermal model presented in section 4.1 being that used also in this case.

The curing kinetic model used is the one presented in Figure 4.11.

The evolution of the degree of cure with the time during the compaction process is shown in Figure 4.12.

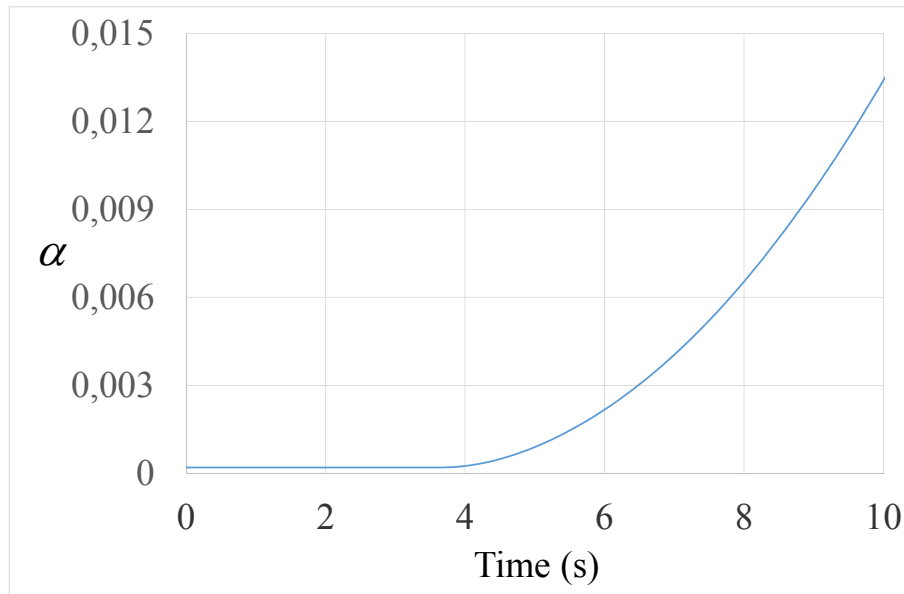


**Figure 4.12. Time vs Degree of cure curve, obtained with the curing kinetic model for a static compaction process during 10 seconds**

The behavior of the curve can be analyzed in two stages:

- Stage 1: the temperature is not high enough, so the material does not react and the degree of cure is not modified.
- Stage 2: after achieving 120 °C, the resin begins to react, increasing its degree of cure. After this stage, the material is cooled down. Therefore the value of the degree of cure will remain constant, as the curing process in the thermoset resins is irreversible.

As can be appreciated, the degree of cure obtained is insignificant, letting us to assert that the compaction process does not advance the curing of the resin.

Note that the evolution of the degree of cure during the first and the second stages is conditioned by the suppositions made for temperatures under 160 °C. It is supposed that the real evolution will be under the one supposed, obtaining values of the degree of cure lower than the one the model predicts, i.e., the model overestimates the value of the degree of cure.

Anyway, it is important to remember that these results have been obtained for a static compaction process. Thus, when the sonotrode is moved along the laminate, the temperatures reached in the resin will be lower than the ones obtained here, leading to an even inferior degrees of cure.

### **4.3 Modelling the evolution of the viscosity with the temperature**

The objective of this section is to obtain an equation that represents the evolution of the viscosity of the resin with the temperature at high heating rates. It will be derived from the experimental results shown in Chapter 1.

The experimental curves that represent the evolution of the viscosity with the temperature were presented in Figure 2.6 of section 2.2.3. Observing the curves, it can be seen that, at low temperatures, the viscosity tends to decrease when increasing the temperature (the viscosity dependence on the temperature is roughly linear if the viscosity is plotted in a logarithmic scale). At a certain temperature, the behavior changes and the viscosity grows when increasing the temperature, this change being due to the beginning of the curing phase. Comparing the different curves, it can be seen that, when increasing the heating rate, the temperature at which the viscosity begins to grow increases.

It has been checked numerically (in section 4.2.3) that the resin is not cured during the ultrasonic compaction process. Therefore, in our case, due to the huge

heating rate that is obtained (that will prevent the initiation of the curing reaction) and the low temperatures raised (up to 120-140°C), a linear approximation between the logarithm of the viscosity and the temperature has been selected, as can be seen in Figure 4.13.

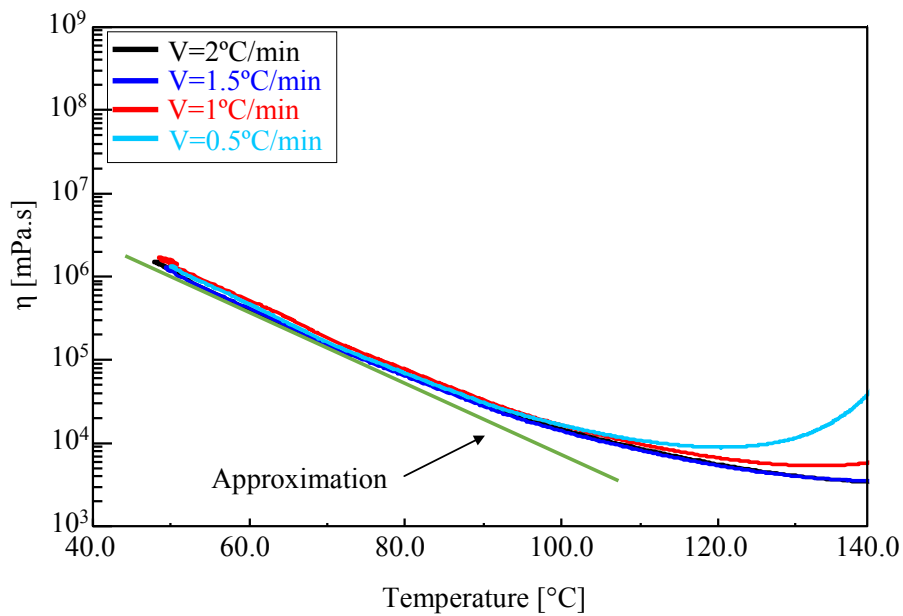


**Figure 4.13. Approximation of the evolution of the viscosity with the temperature for low temperatures and high temperature rates**

The equation that fits this approximation is:

$$\eta = 10^{(17.081-0.04357T)} \quad (4.8)$$

The validity of this approximation of the evolution of the viscosity will be checked comparing the resolution of the model proposed in Chapter 5 with experimental measurements.

## 4.4 Conclusions

In this Chapter, several preliminary models and results have been obtained, in order to understand the compaction process properly. This understanding will conduct to a better modelling of the process.

A thermal model has been developed first. This model has been implemented in a FEM commercial program (MSC.Marc/Mentat [4.1]). The thermal model allows the temperature field in the laminate to be obtained from the measurement of the temperature at the sonotrode tip. Although this model is simple and does not allow the temperature field to be estimated when the compaction conditions are modified, it has been used to validate the thermal properties of the materials involved in the process given in the literature [4.3].

The temperatures obtained with the thermal model have also been used to estimate the possibility of a partial curing of the resin during the compaction process. A curing model has been developed, from experimental measurements, to estimate the degree of cure during the process.

As the experimental results were given for temperatures higher than the ones obtained in the compaction process, several considerations on the evolution of the degree of cure and its variation on the time have been done, for temperatures lower than 160 °C.

The results given by the coupled curing and thermal model have shown that the curing during the compaction process is negligible. It has also been noticed that the results are obtained for a static compaction. Thus, in a process in which the sonotrode is moved along the laminate, the degree of cure obtained will be even lower.

As the temperature field obtained during the compaction process does not increase the degree of cure significantly, it will be assumed that a phase change is not produced in the resin. This fact will lead to assume that the resin will behave as

a liquid during all the process time. This assumption will be used in the heat generation model presented in Chapter 5.

Finally, a model to calculate the evolution of the viscosity with the temperature has been presented. This model will be used next, during the modelling of the heat generation during the compaction. As the experimental results were obtained for heating rates lower than the one obtained in the ultrasonic compaction, several assumptions have been done, its validity being checked in the resolution of the models presented in the following chapters.

## Bibliography

- [4.1] *MSC.MARC/MENTAT product documentation*. MSC.Software Documentation, 2006.
- [4.2] Skordos, S., *Modelling of composites curing in MSC.MARC*, Lecture notes of MSC.Software, Madrid, Febrero de 2008.
- [4.3] Seebacher, S., *Contributions to the investigation of in-situ ultrasonic tape lamination of composite thermoset prepregs*. Master thesis at the Private fachhochschule Göttingen, 2008.
- [4.4] Sánchez-Blázquez, A., *Aplicación de la espectroscopía infrarroja y el análisis térmico en la monitorización de la polimerización de resinas termoestables utilizadas en la industria aeronáutica*. EADS-CASA, Report.
- [4.5] Um, M.-K., Isaac M. Daniel, I.M., Hwang, B.-S., *A study of cure kinetics by the use of dynamic differential scanning calorimetry*. Composites Science and Technology, Vol. 62, pp. 29–40, 2002.
- [4.6] *FTIR modeling on MIHEXCEL 8552*. EADS-CASA, Report, 1999.



# *Chapter 5*

## *Modelling the heat generation*

The scope of this chapter is the development of a model capable to predict the heat generated inside the resin during the ultrasonic compaction due to the internal viscosity.

Several studies have been carried out for similar compaction processes (but with a configuration different than the studied in this work) coupled with the filament winding manufacturing technology [5.1, 5.2, 5.3].

In this case, the model assumes a liquid behavior of the resin along all the process, supposing there is no curing, due to the temperatures reached and the short time the resin is exposed to those temperatures.

The movement of the sonotrode that produces the heat generation will be decomposed in its vertical (corresponding to the  $y$  axis) and horizontal (corresponding to the  $x$  axis) components, in order to study their heating effects separately.

Firstly, some preliminary remarks will be done, concerning the modelling of the pre-preg and the velocity profiles than can be found in the resin, due to the different components of the movement of the sonotrode. Secondly, in section 5.2, the main hypotheses that concern the model will be posed. Thirdly, the boundary conditions that take place in the different resin volumes will be set out. Fourthly, the heat generation will be obtained for both the horizontal and vertical components of the movement of the sonotrode. Finally, in section 5.5, the conclusions concerning this heat generation model will be presented.

## 5.1 Preliminary remarks

Prior to present the main hypotheses and the equations that describe the heat generation, the model assumed for the pre-preg plies, the mechanism by which the heating is generated and the movements induced by the ultrasonic oscillation of the sonotrode inside the resin will be commented.

Note that, in this case, as only the generation of the heat is searched, the area of study will be the zone of the laminate located under the sonotrode.

During the compaction process, the resin inside the uncured preimpregnated plies will be assumed to behave as a liquid with high viscosity. Therefore, heat generation will occur only in uncured plies. Each pre-preg ply will be modeled as the joint of two resin layers with a layer of fibres between them (see Figure 5.1). In this case, the total thickness of a ply,  $h_p$  (see Figure 5.2), is the sum of the thickness of two resin layers (with thickness  $h_r$ ) and one fibre layer (with thickness  $h_f$ ). Other possible model for structure of the pre-preg plies will be commented in Chapter 6, discussing the validity of the model assumed in this Chapter.

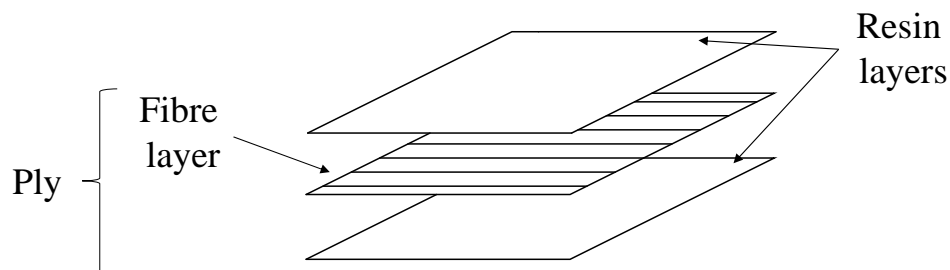


**Figure 5.1. Scheme of a pre-preg ply**

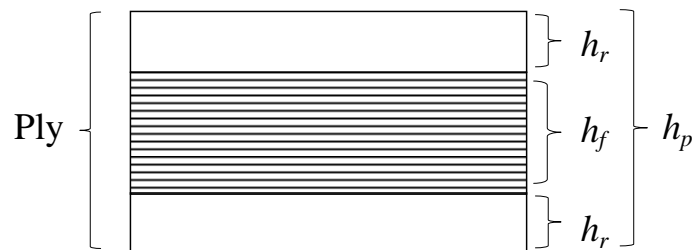


**Figure 5.2. Thicknesses in a pre-preg ply**

The heating of the plies will be generated during the compaction process by the internal viscosity of the resin. The cause is the movement generated inside the resin by the vibration of the sonotrode over the laminate. This movement, which can be decomposed into its horizontal and vertical components, generates several velocity profiles inside the resin that will be described next.

The vertical movement of the sonotrode, whose vertical velocity is designated as  $w_{sv}(t)$ , induces an oscillating pressure that is transmitted to all resin layers due to the compression of the lay-up, and generates a horizontal velocity profile in the resin,  $u^i(x, y, t)$ , called Hagen-Poiseuille profile (see Figure 5.3), Pfitzner [5.4].

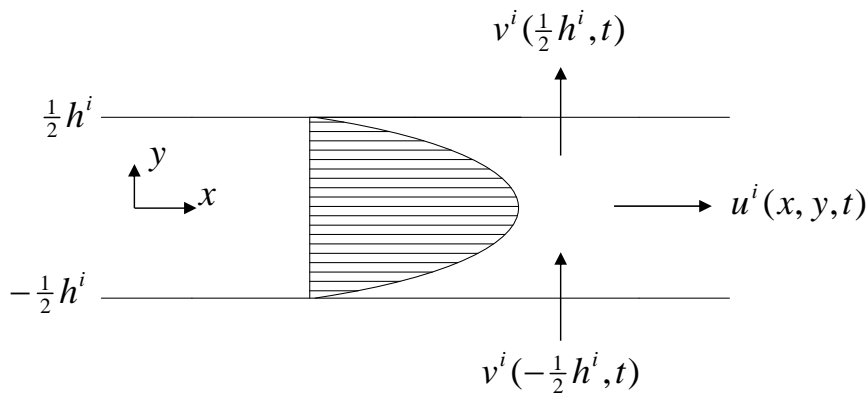


**Figure 5.3. Hagen-Poiseuille horizontal velocity profile of the resin originated by the vertical movement of the sonotrode in the  $i^{\text{th}}$ -resin layer**

The variables that appear in Figure 5.3 are: the horizontal axis  $x$ , the vertical axis  $y$ , the thickness of the  $i^{\text{th}}$  resin layer  $h^i$ , the horizontal velocity  $u^i(x, y, t)$  of the resin, the vertical velocity  $v^i(x, y, t)$  of the resin and the time  $t$  of the process. For the sake of simplicity, in the present chapter a local  $y$  variable will be employed in each resin layer  $-\frac{1}{2}h^i < y < \frac{1}{2}h^i$ .

The horizontal movement of the sonotrode, whose velocity is designated as  $w_{sh}(t)$ , is transmitted only to the first layer of resin due to the shear movement (the fibre is solid and still, the movement not then being transmitted to the resin under it) and generates a horizontal velocity profile in the resin called Couette profile (see Figure 5.4), Wendl [5.5].

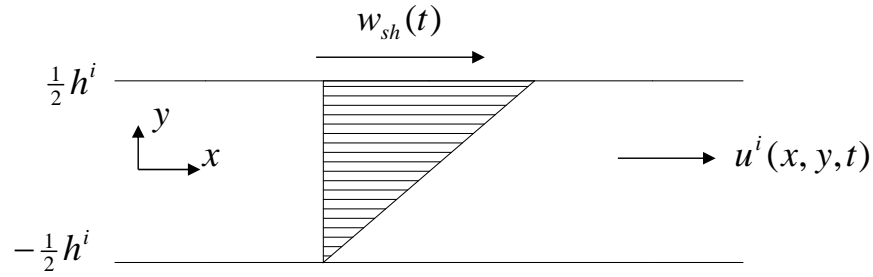


**Figure 5.4. Couette horizontal velocity profile of the resin originated by the horizontal movement of the sonotrode in the  $i^{\text{th}}$ -resin layer**

Notice that plane behavior throughout the  $x$ - $y$  plane has been assumed. This is motivated by the directionality that the fibres force, prescribing the movement of the fluid resin in the  $x$  direction and avoiding possible movements perpendicular to this  $x$ - $y$  plane.

## 5.2 Hypotheses of the model

The equations that govern the heat generation in the compaction of several uncured plies will be presented next. As mentioned in section 5.1, the main hypothesis that will be considered in the analysis of the heat generation, for the problem defined in section 1.3.2.2 (the compaction of multiple uncured plies) is plane behavior.

To obtain the heat generated during the ultrasonic debulking, the inertialess Navier-Stokes equations, i.e. the Stokes equations [5.6], are employed. In particular, for the typical layer  $i$  shown in Figure 2.2 of Chapter 2, Stokes equations write:

$$\begin{aligned} \frac{\partial p^i(x, y, t)}{\partial x} &= \eta^i(t) \left( \frac{\partial^2 u^i(x, y, t)}{\partial x^2} + \frac{\partial^2 u^i(x, y, t)}{\partial y^2} \right) \\ \frac{\partial p^i(x, y, t)}{\partial y} &= \eta^i(t) \left( \frac{\partial^2 v^i(x, y, t)}{\partial x^2} + \frac{\partial^2 v^i(x, y, t)}{\partial y^2} \right) \end{aligned} \quad (5.1)$$

where  $x$  is the horizontal coordinate (i.e. parallel to the fibres),  $y$  is the vertical coordinate (i.e. in the thickness direction of the ply),  $u^i(x, y, t)$  is the horizontal component of the velocity in layer  $i$ ,  $v^i(x, y, t)$  is the vertical component of the velocity in layer  $i$ ,  $\eta^i(t)$  is the viscosity of the resin in layer  $i$  (assumed constant within the layer) and  $p^i(x, y, t)$  is the pressure in layer  $i$ .

Note that  $\eta^i(t)$  is dependent on temperature. Since only the heat generation is being calculated in this section, the influence of temperature is not important. However, in the study of the coupled problem, the dependence of  $\eta^i(t)$  on temperature must be appropriately taken into account, see section 4.3.

Another hypothesis considered is the hydrodynamic lubrication [5.7]. This entails that:

$$\frac{\partial^2 v^i(x, y, t)}{\partial x^2} \approx 0; \quad \frac{\partial^2 v^i(x, y, t)}{\partial y^2} \approx 0 \quad (5.2)$$

and that:

$$\frac{\partial^2 u^i(x, y, t)}{\partial x^2} \ll \frac{\partial^2 u^i(x, y, t)}{\partial y^2} \quad (5.3)$$

Introducing (5.2) and (5.3) in (5.1) implies that the pressure on the layer  $i$  depends only on the  $x$  coordinate:

$$p^i(x, y, t) \approx p^i(x, t) \quad (5.4)$$

The dimensions of the problem (~0.01 mm in the vertical direction and ~20 mm, the width of the zone under the sonotrode, in the horizontal direction) justify the abovementioned hypothesis.

## 5.3 Boundary conditions

Considering a set of uncured plies,  $i = 1, \dots, n$  (see Figure 2.2), with 1 being the ply in contact with the table and  $n$  being the ply in contact with the sonotrode, boundary conditions are those described in the following paragraphs.

For the sake of clarity, boundary conditions employed in the solution associated to the horizontal and vertical movements of the sonotrode are separated into distinct sections.

As shown in Figure 5.1, each ply has two resin layers separated by a fibre layer. The top resin layer of an intermediate ply is adjacent to the bottom resin layer of the ply situated on top of it. Therefore, these two resin layers can be treated as a single resin layer with double thickness. Consequently, for  $n$  plies,  $n+1$  resin layers are obtained, their height being defined as:

$$\begin{aligned} h^1 &= h^{n+1} = h_r \\ h^i &= 2h_r \quad i = 2, \dots, n \end{aligned} \quad (5.5)$$

where  $h_r$  is the thickness of one of the resin layers of a ply.

### 5.3.1 Vertical movement of the sonotrode

For all resin layers, the horizontal velocity of the points in contact with the fibres, with the sonotrode or with the table is equal to zero:

$$u^i(x, -\frac{1}{2}h^i, t) = 0 \quad i = 1, \dots, n+1 \quad (5.6)$$

$$u^i(x, \frac{1}{2}h^i, t) = 0 \quad i = 1, \dots, n+1 \quad (5.7)$$

The vertical velocity of the resin in contact with the sonotrode (in the upper boundary of the top layer) is equal to the vertical velocity of the sonotrode  $w_{sv}(t)$ :

$$v^{n+1}\left(x, \frac{1}{2}h^{n+1}, t\right) = w_{sv}(t) = \delta_v \omega \cos(\omega t) \quad (5.8)$$

where  $\delta_v$  is the amplitude of the oscillations in the vertical movement and  $\omega$  is the frequency of the ultrasounds.

The vertical velocities of the layers are coupled through the fibre interphase.

$$v^i\left(x, \frac{1}{2}h^i, t\right) = v^{i+1}\left(x, -\frac{1}{2}h^{i+1}, t\right) \quad i = 1, \dots, n \quad (5.9)$$

For the sake of clarity, the vertical velocities in contact with the fibre will be equaled with the vertical velocity of the fibre layer, reducing the notation to:

$$v_f^i(t) = v^i\left(x, \frac{1}{2}h^i, t\right) = v^{i+1}\left(x, -\frac{1}{2}h^{i+1}, t\right) \quad i = 1, \dots, n \quad (5.10)$$

The vertical velocity of the resin in contact with the table (bottom layer) is equal to zero:

$$v_f^0(t) = v^1\left(x, -\frac{1}{2}h^1, t\right) = 0 \quad (5.11)$$

### 5.3.2 Horizontal movement of the sonotrode

The conditions given by equation (5.6) and (5.7) remains equal in this situation, except for the case of the horizontal velocity of the points in contact with the sonotrode. In this case, the horizontal velocity of the resin in contact with the sonotrode (in the upper boundary of the top layer) is equal to the horizontal velocity of the sonotrode,  $w_{sh}(t)$ , that is, as described in [5.8], a sinusoidal function:

$$u^{n+1}\left(x, \frac{1}{2}h^{n+1}, t\right) = w_{sh}(t) = \delta_h \omega \cos(\omega t) \quad (5.12)$$

where  $\delta_h$  is the amplitude of the oscillations in the horizontal movement of the sonotrode and  $\omega$  is the frequency of the ultrasounds.

In this movement, vertical velocities are assumed to be negligible everywhere.

## 5.4 Evaluation of the heat generated

The heat generated in a resin layer  $i$  will be denoted by  $\dot{Q}_{gen}^i(x, y, t)$ . Its general form can be written as:

$$\dot{Q}_{gen}^i(x, y, t) = \boldsymbol{\sigma}^i(x, y, t) : \mathbf{D}^i(x, y, t) \quad (5.13)$$

where  $:$  denotes the product component by component of the tensors  $\boldsymbol{\sigma}^i$  and  $\mathbf{D}^i$ .

$\mathbf{D}^i$  is the strain velocities tensor of the resin for layer  $i$ , which for this particular case adopts the form:

$$\mathbf{D}^i(x, y, t) \approx \begin{pmatrix} 0 & \frac{1}{2} \frac{\partial u^i(x, y, t)}{\partial y} \\ \frac{1}{2} \frac{\partial u^i(x, y, t)}{\partial y} & 0 \end{pmatrix} \quad (5.14)$$

$\boldsymbol{\sigma}^i$  is the stress tensor of the resin in layer  $i$ :

$$\boldsymbol{\sigma}^i(x, y, t) = 2\eta^i(t)\mathbf{D}^i(x, y, t) \quad (5.15)$$

The solutions for the vertical and the horizontal components of the movement of the sonotrode are presented separately again. The equations for the velocity  $u^i(x, y, t)$  and for the heat generated  $\dot{Q}_{gen}^i(x, y, t)$  will be obtained for each component.

### 5.4.1 Heat generated by the vertical movement of the sonotrode

To obtain the horizontal velocity field associated to the vertical movement of the sonotrode, the pressure distribution in each layer needs to be determined. Therefore, the vertical velocities of the fibres will be determined first.

Taking into account the assumptions made in (5.4), the following condition can be obtained for the pressure distribution in each layer:

$$\frac{\partial p^i(x, y, t)}{\partial y} = 0 \Rightarrow p^i(x, y, t) = p^i(x, t) \quad (5.16)$$

Thus, the first equation of (5.1) can easily be integrated to obtain:

$$\begin{aligned} \frac{\partial p^i(x, t)}{\partial x} &= \eta^i(t) \frac{\partial^2 u^i(x, y, t)}{\partial y^2} \Rightarrow \\ \Rightarrow \frac{\partial u^i(x, y, t)}{\partial y} &= \frac{1}{\eta^i(t)} \frac{\partial p^i(x, t)}{\partial x} y + A(x, t) \end{aligned} \quad (5.17)$$

$A$  being a function that can be determined applying to the horizontal velocity the condition that the flow rate has to be symmetric:

$$y = 0 \Rightarrow \frac{\partial u^i(x, y, t)}{\partial y} = 0 \Rightarrow A(x, t) = 0 \quad (5.18)$$

Integrating (5.17), the equation that defines the horizontal velocity as a function of the variation of the pressure is obtained:

$$u^i(x, y, t) = \frac{1}{2\eta^i(t)} \frac{\partial p^i(x, t)}{\partial x} y^2 + B(x, t) \quad (5.19)$$

$B$  being a function that can be determined applying the boundary conditions at the top or, because of the symmetry, at the bottom of the layer (5.7):

$$\begin{aligned}
 u^i\left(x, \frac{1}{2}h^i, t\right) = 0 &= \frac{1}{2\eta^i(t)} \frac{\partial p^i(x, t)}{\partial x} \frac{(h^i)^2}{4} + B(x, t) \Rightarrow \\
 \Rightarrow B(x, t) &= -\frac{1}{2\eta^i(t)} \frac{\partial p^i(x, t)}{\partial x} \frac{(h^i)^2}{4}
 \end{aligned}
 \tag{5.20}$$

Thus, the horizontal velocity distribution is:

$$u^i(x, y, t) = \frac{1}{2\eta^i(t)} \frac{\partial p^i(x, t)}{\partial x} \left( y^2 - \frac{(h^i)^2}{4} \right)
 \tag{5.21}$$

The pressure gradient can be obtained by applying the mass balance. The flow rate in layer  $i$  in horizontal direction,  $F^i(x, t)$ , will be:

$$F^i(x, t) = \int_{-h^i/2}^{h^i/2} u^i(x, y, t) dy = -\frac{(h^i)^3}{12\eta^i(t)} \frac{\partial p^i(x, t)}{\partial x}
 \tag{5.22}$$

The expression that relates the flow rate and the vertical velocities of the surrounding fibres is obtained by applying the balance of flow rate in the differential element shown in Figure 5.5.

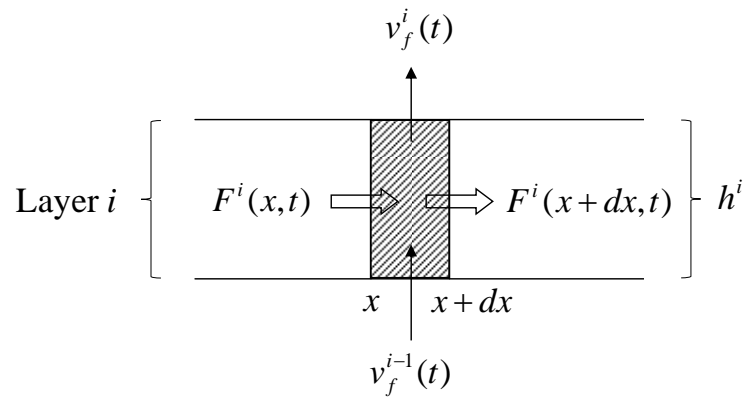


**Figure 5.5. Balance of flow rate in a control volume**

The mass balance, the fluid being incompressible, reads:

$$F^i(x, t)dt - F^i(x + dx, t)dt = v_f^i(t)dxdt - v_f^{i-1}(t)dxdt
 \tag{5.23}$$

Assuming a linear expansion of  $F^i$ :

$$F^i(x+dx, t) = F^i(x, t) + \frac{\partial F^i(x, t)}{\partial x} dx \quad (5.24)$$

and substituting (5.24) in (5.23), it yields:

$$-\frac{\partial F^i(x, t)}{\partial x} = v_f^i(t) - v_f^{i-1}(t) \quad (5.25)$$

Substituting (5.22) in (5.25) yields:

$$\frac{(h^i)^3}{12\eta^i(t)} \frac{\partial^2 p^i(x, t)}{\partial x^2} = v_f^i(t) - v_f^{i-1}(t) \quad (5.26)$$

Now, equation (5.26) is going to be particularized for resin layer 1, resin layer 2 and a general resin layer  $i$ . Notice that the lowest layer (layer 1) is in contact with the table and the vertical velocity in its lower side is null.

Particularization of (5.26) for layer 1 leads to:

$$\begin{aligned} \frac{(h^1)^3}{12\eta^1(t)} \frac{\partial^2 p^1(x, t)}{\partial x^2} &= v_f^1(t) - v_f^0(t) \Rightarrow \\ \Rightarrow \frac{\partial^2 p^1(x, t)}{\partial x^2} &= v_f^1(t) \frac{12\eta^1(t)}{(h^1)^3} \end{aligned} \quad (5.27)$$

where it has been taken into account that  $v_f^0(t) = 0$ .

Particularization of (5.26) for layer 2 leads to:

$$\frac{(h^2)^3}{12\eta^2(t)} \frac{\partial^2 p^2(x, t)}{\partial x^2} = v_f^2(t) - v_f^1(t) \quad (5.28)$$

Particularization of (5.26) for layer  $i$  leads to:

$$\frac{(h^i)^3}{12\eta^i(t)} \frac{\partial^2 p^i(x,t)}{\partial x^2} = v_f^i(t) - v_f^{i-1}(t) \quad (5.29)$$

The balance of forces in the vertical direction in the fibre layer between resin layers 1 and 2 implies that:

$$p^1(x,t) = p^2(x,t) \quad (5.30)$$

The relation between the vertical velocities is obtained by substituting (5.27) into (5.28):

$$\begin{aligned} \frac{12\eta^1(t)}{(h^1)^3} v_f^1(t) &= \frac{12\eta^2(t)}{(h^2)^3} (v_f^2(t) - v_f^1(t)) \Rightarrow \\ \Rightarrow v_f^1(t) &= \frac{(h^1)^3 \eta^2(t)}{(h^2)^3 \eta^1(t) + (h^1)^3 \eta^2(t)} v_f^2(t) = S^2(t) v_f^2(t) \end{aligned} \quad (5.31)$$

The balance of forces in the fibre layer between resin layers  $i-1$  and  $i$  implies that:

$$p^{i-1}(x,t) = p^i(x,t) \quad (5.32)$$

which enables obtaining the relation between the vertical velocities of two consecutive fibre layers.

$$v_f^{i-1}(t) = \frac{(h^{i-1})^3 \eta^i(t)}{(h^i)^3 \eta^{i-1}(t)(1 - S^{i-1}(t)) + (h^{i-1})^3 \eta^i(t)} v_f^i(t) = S^i(t) v_f^i(t) \quad (5.33)$$

The relation for all the vertical velocities can be obtained following the methodology described by (5.31) and (5.33) for all resin layers. The vertical velocity at the top of the upper layer,  $v_f^{n+1}(t) = v^{n+1}(x, \frac{1}{2}h^{n+1}, t)$ , is known (since it is equal to the vertical velocity of the sonotrode). Thus, all the vertical velocities can be obtained starting from the top and calculating each velocity downwards from the previous one until  $v_f^1$  is determined.

Once the vertical velocities of the fibres have been determined, the horizontal velocity profile in the resin can be obtained for this component of the movement of the sonotrode.

With reference to the horizontal velocity of the resin, as mentioned in section 1.3.2 for the Hagen-Poiseuille velocity profile [5.4], it is assumed to be parabolic:

$$u^i(x, y, t) = C(x, t) + D(x, t)y + E(x, t)y^2 \quad (5.34)$$

where  $C(x, t)$ ,  $D(x, t)$  and  $E(x, t)$  are functions that have to be determined by the application of the following conditions.

$D$  can be obtained applying the flow symmetry:

$$\frac{\partial u^i(x, y = 0, t)}{\partial y} = D(x, t) = 0 \Rightarrow D(x, t) = 0 \quad (5.35)$$

$C$  can be obtained applying (5.6):

$$\begin{aligned} u^i(x, y = -\frac{1}{2}h^i, t) = 0 &\Rightarrow C(x, t) + E(x, t)\frac{(h^i)^2}{4} = 0 \Rightarrow \\ &\Rightarrow C = -E(x, t)\frac{(h^i)^2}{4} \end{aligned} \quad (5.36)$$

The horizontal velocity field, at this point, is:

$$u^i(x, y, t) = E(x, t)\left(y^2 - \frac{(h^i)^2}{4}\right) \quad (5.37)$$

$E(x, t)$  can be obtained by applying the mass balance at the control volume shown in Figure 5.6:

$$\begin{aligned}
 2F^i(x,t) &= v_f^{i-1}(t)2x - v_f^i(t)2x \Rightarrow \\
 \Rightarrow F^i(x,t) &= [v_f^{i-1}(t) - v_f^i(t)]x
 \end{aligned} \tag{5.38}$$

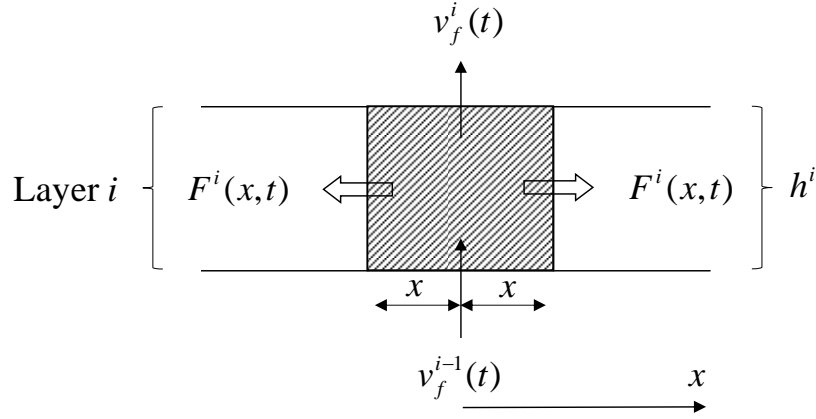


**Figure 5.6. Balance at the  $i^{\text{th}}$  layer**

Substituting (5.38) in the balance of flow rate:

$$\begin{aligned}
 [v_f^{i-1}(t) - v_f^i(t)]x &= F^i(x,t) = \int_{-\frac{h^i}{2}}^{\frac{h^i}{2}} u^i(x,y,t) dy \Rightarrow \\
 \Rightarrow E(x,t) &= -\frac{6}{(h^i)^3} [v_f^{i-1}(t) - v_f^i(t)]x
 \end{aligned} \tag{5.39}$$

Therefore, the horizontal component of the velocity field obtained in this problem, generalized for any layer,  $u^i$ , is:

$$u^i(x,y,t) = -\frac{6}{(h^i)^3} [v_f^{i-1}(t) - v_f^i(t)] \left( y^2 - \frac{(h^i)^2}{4} \right) x \tag{5.40}$$

The vertical components of the velocity field obtained at the interphases are:

$$v_f^0(t) = 0 \tag{5.41}$$

$$v_f^{n+1}(t) = w_{sv}(t) \tag{5.42}$$

$$v_f^{i-1}(t) = S^i(t)v_f^i(t) \quad \text{for } i = 2, \dots, n+1 \quad (5.43)$$

and

$$S^1(t) = 0$$

$$S^i(t) = \frac{(h^{i-1})^3 \eta^i(t)}{(h^i)^3 \eta^{i-1}(t)(1 - S^{i-1}(t)) + (h^{i-1})^3 \eta^i(t)} \quad i = 2, \dots, n+1 \quad (5.44)$$

Once the velocity profile is determined, the heat generated in any layer,  $\dot{Q}_{gen\_v}^i$ , can be obtained from (5.13-5.15) yielding:

$$\dot{Q}_{gen\_v}^i(x, y, t) = \frac{144\eta^i(t)}{(h^i)^6} [v_f^{i-1}(t) - v_f^i(t)]^2 y^2 x^2 \quad (5.45)$$

In this case,  $u^i(x, y, t)$  depends linearly on  $x$  and quadratically on  $y$ . Thus, the heat generated is different at each point of the layer.

## 5.4.2 Heat generated by the horizontal movement of the sonotrode

As mentioned above, the horizontal component of the movement will only affect to the resin layer in contact with the sonotrode.

In this case, the vertical velocity field is null, since there is no movement transmitted vertically.

The horizontal velocity of the sonotrode is defined by:

$$w_{sh}(t) = \delta_h \cdot \omega \cdot \cos(\omega \cdot t) \quad (5.46)$$

The horizontal velocity profile in the resin in this case, as mentioned in section 1.3.2 for the Couette velocity profile [5.5], is assumed to depend linearly on  $y$ . Therefore, it will be of the form:

$$u^{n+1}(x, y, t) = F(x, t) + G(x, t)y \quad (5.47)$$

where  $F$  and  $G$  are functions to be determined.

Applying (5.6), the value of the function  $F(x, t)$  can be obtained:

$$\begin{aligned} u^{n+1}\left(x, -\frac{1}{2}h^{n+1}, t\right) = 0 &= F(x, t) - G(x, t)\frac{h^{n+1}}{2} \Rightarrow \\ \Rightarrow F(x, t) &= G(x, t)\frac{h^{n+1}}{2} \end{aligned} \quad (5.48)$$

Applying (5.12), the value of the function  $G(x, t)$  can be obtained:

$$\begin{aligned} u^{n+1}\left(x, \frac{1}{2}h^{n+1}, t\right) = w_{sh}(t) &= F(x, t) + G(x, t)\frac{h^{n+1}}{2} \Rightarrow \\ \Rightarrow G(x, t) &= \frac{w_{sh}(t)}{h^{n+1}} \end{aligned} \quad (5.49)$$

The horizontal component of the velocity field associated to the horizontal movement of the sonotrode is:

$$\begin{aligned} u^{n+1}(x, y, t) &= \frac{w_{sh}(t)}{h^{n+1}} \left( \frac{h^{n+1}}{2} + y \right) \\ u^i(x, y, t) &= 0 \quad i = 1, \dots, n \end{aligned} \quad (5.50)$$

The vertical component of the velocity is equal to zero for all the layers.

The solution of the problem for the heat generated in the horizontal movement of the sonotrode,  $\dot{Q}_{gen\_h}^n$ , is:

$$\dot{Q}_{gen\_h}^{n+1}(x, y, t) = \eta^{n+1}(t) \left( \frac{w_{sh}(t)}{h^{n+1}} \right)^2 \quad (5.51)$$

In the rest of the layers the heat generated is equal to zero due to the absence of velocity.

Note that only the derivatives of  $u^i(x, y, t)$  with respect to the vertical coordinate  $y$  appear in (5.14) and (5.15). Since  $u^i(x, y, t)$  has been assumed to depend linearly on  $y$ , equations (5.47) and (5.50), the heat generated at a point does not depend on the position of the point.

As can be seen in equations (5.40)-(5.43) and (5.51), the heat generated at each point by the vibration of the sonotrode is presented as a function of the amplitude,  $\delta_h$ ,  $\delta_v$ , and the frequency of the sonotrode oscillations,  $\omega$ , defined in equations (5.8) and (5.12), the location of the point and the time of the process.

## 5.5 Conclusions

A model that determines the viscous heat generation of the resin in a laminate during the ultrasonic compaction has been developed.

The heat generated has been decomposed in two components, given by the vertical and horizontal components of the movement of the sonotrode. These movements lead to different velocity profiles. In this case, the Couette and Hagen-Poiseuille velocity profiles have been assumed for both the horizontal and the vertical movements, respectively. The velocity profiles assumed has conditioned the transmission of the movement along the resin layers, the Hagen-Poiseuille velocity profile being transmitted to all the resin layers and the Couette velocity profile being transmitted only to the first resin layer.

The main hypotheses used in the development of this heat generation model have been the plane behavior, given by the directionality that the fibres impose to the liquid resin and the hydrodynamic lubrication, assumed due to the dimensions of the problem. This last hypothesis helps to simplify the Stokes equations that define the pressure field in the different resin layers.

The heat generated has been obtained as a function of the viscosity and the vertical velocities at the extremes of the resin layers.

The vertical velocities of the resin layers have been related with the vertical velocities of the fibre layers, which can be obtained from the vertical velocity of the sonotrode.

This heat generation model will be implemented, in next Chapters, in several heat distribution resolutions. In this way the thermal field in the laminate during the compaction process will be solved.

## Bibliography

- [5.1] Roylance M., Roylance D., Nesmith K.: *Use of Ultrasonic Tape Lamination for In-Process Debulking of Thick Composite Structures*. Proceedings of the 43rd International SAMPE Symposium and Exhibition (1998).
- [5.2] Loud S.: *Bridging the Centuries with SAMPE's Materials and Processes Technology*. Long Beach Convention Center, Long Beach California. Taylor & Francis (2000).
- [5.3] Roylance M., Player J., Zukas W., Roylance D.: *Modeling of Ultrasonic Processing*. *Journal of Applied Polymer Science*. Vol. 93, 1609–1615 (2004).
- [5.4] Pfitzner, J.: *Poiseuille and his law*. *Anaesthesia* 31 (2), 273–5 (1976).

[5.5] Wendl, M.C.: *General Solution for the Couette Flow Profile*. Physical Review E 60, 6192-6194 (1999).

[5.6] Temam, R.: *Navier-Stokes Equations*. American Mathematical Society (2001).

[5.7] Hori, Y.: *Hydrodynamic Lubrication*. Springer (2006).

[5.8] Seebacher, S.: *Contributions to the investigation of in-situ ultrasonic tape lamination of composite thermoset prepregs*. Master Thesis at the Private fachhochschule Göttingen (2008).

# *Chapter 6*

## *Semi-analytical model*

In order to check the validity of the heat generation model developed in Chapter 5, a semi-analytical model that couples this heat generation with the heat distribution inside the laminate is presented. This model is based on 1D heat transfer equations, taking into account the heats involved in two directions, on a way of enriching the 1D solution.

First, several considerations about the modelling of the pre-preg plies are presented. Two possibilities will be distinguished: considering each pre-preg ply as

the sum of two resin layers and a fibre layer, and considering each pre-preg ply formed by the same number of resin layers as the number of fibres in the thickness.

Second, the heat generation model that has been assumed will be presented. In the third section, the equations used to define the heat distribution in the laminate will be posed. Due to the coupled nature of the problem (the heat generated in each resin layer depends on the temperatures of the other resin layers), an incremental algorithm will be developed in the fourth section.

In section 6.5, the way of implementing the geometry and the algorithm to solve the problem in a commercial mathematical programming software (Matlab [6.1]) will be shown. The results obtained with the model are presented in section 6.6, in which a comparison of the results with experimental data will also be carried out.

Finally, the conclusions related to the semi-analytical model and the results presented in this Chapter will be discussed.

## **6.1 Alternatives in the pre-preg modelling**

Prior to implement the heat generation model presented in Chapter 5 into a heat distribution model, several considerations concerning the modelling of the pre-preg plies are going to be done.

During the development of the formulation presented in Chapter 5, each pre-preg ply was considered formed by several resin and fibre layers. As can be supposed, the number of resin layers considered to be contained in a ply can affect the solution. Two hypotheses concerning the number of layers that conforms a ply have been done:

- First hypothesis: Each pre-preg ply is formed by two resin layers and, in the middle of them, a fibre layer, the thickness of the fibre

layer being the half of the total ply thickness. In this case, the formulation of each ply can be expressed as [RL/FL/RL].

- Second hypothesis: The pre-preg is formed by  $q$  resin layers and  $q-1$  fibre layers, uniformly distributed along the ply thickness, following the sequence [(RL/FL) $_{q-1}$ /RL]. In this case, the number of fibres layers coincide with the number of fibres contained in the ply thickness. The thickness of all layers is considered the same, and equal to the thickness of a single fibre.

Both models considered in the hypotheses can be appreciated in the drafts shown in Figure 6.1 and Figure 6.2, respectively.



**Figure 6.1. First hypothesis considered for the pre-preg modelling**

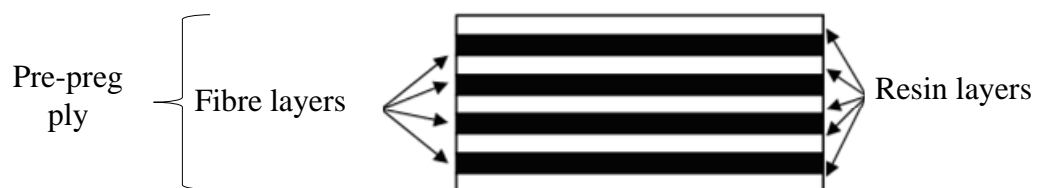


**Figure 6.2. Second hypothesis considered for the pre-preg modelling**

The first hypothesis is supposed to be closed to the reality just at the beginning of the compaction process, due to the method of manufacturing the pre-preg [6.2].

The second hypothesis is supposed to be closed to the reality along and at the end of the process, due to the mixing procedure carried out during the compaction of the laminate. This consideration is not completely true in several pre-preg formulations (a minority), in which few mixing of the components is appreciated. Thus, the first hypothesis is more realistic during all the compaction process.

It is important to remark that, when observing the pre-preg ply drafted in the second hypothesis, the plane behaviour of the problem assumed in Chapter 5 can be better appreciated. In this case, the fluid resin is contained in “fibre channels”, only having the possibility to flow along the  $x$  axis direction.

The results obtained when using both hypotheses and a comparison of them will be presented in section 6.6.

Note that the equations and algorithms presented in the following sections are valid for both hypotheses which only differ in the number and size of the fibre layers and resin layers.

## 6.2 Heat generation modelling

In order to model the heat generated, the equations developed in Chapter 5 will be used. In those equations, the heat generated is obtained for both the vertical,  $\dot{Q}_{gen\_v}^i$ , and horizontal,  $\dot{Q}_{gen\_h}^i$ , components of the movement of the sonotrode. The heats are expressed as a function of the temperatures, the vertical velocities and the viscosities of each resin layer.

As the heat inside the resin is supposed to be homogenized very fast, the heats generated are integrated in the resin volumes,  $\dot{Q}_{gen\_m}^i$ , leading to the following expression:

$$\dot{Q}_{gen\_m}^i(t_j) = \int_{-L_s/2}^{L_s/2} \int_{-h^i/2}^{h^i/2} [\dot{Q}_{gen\_h}^i(x, y, t_j) + \dot{Q}_{gen\_v}^i(x, y, t_j)] dy dx \quad (6.1)$$

where  $i$  is the number of layer and  $t_j$  the time at the time step  $j$ .

Note that, in this case, the  $x$  and  $y$  axis are contained in each resin layer and concern only the resin volumes.

The value of the heat generated due to the vertical,  $\dot{Q}_{gen\_v}^i(x, y, t_j)$ , and the horizontal,  $\dot{Q}_{gen\_h}^i(x, y, t_j)$ , components of the movement of the sonotrode are calculated with Equations (5.45), (5.51) and related.

This integrated expression will be used, as will be shown in section 6.4, in the calculation of the total heat in the resin layers.

### 6.3 Heat distribution modelling

In this section, the equations used to solve the heat transfers in the thermal distribution model will be explained.

In this case, only the material located under the sonotrode will be modelled and, therefore, only heat conduction will be taken into account as heat transfer (as the sonotrode is located over the laminate, no convection phenomena will take place). To model the conduction, the 1D Fourier heat transfer equations have been considered, resulting in each case in the following equations:

- Equation used to model the conduction between the top layer and the sonotrode:

$$\dot{Q}_{cu}^n(t_j) = k_s \left( \frac{T_0 - T^n(t_j)}{l_s} \right) b \cdot a \quad (6.2)$$

where  $\dot{Q}_{cu}^n$  is the heat conduction with the sonotrode,  $k_s$  is the conductivity of the sonotrode,  $a$  is the depth of the sonotrode,  $b$  is the width of the sonotrode,  $l_s$  is the length of the sonotrode and  $T_0$  is the room temperature.

- Equation used to model the conduction that takes place along the fibres, between the resin layers:

$$\dot{Q}_{cu}^i(t_j) = -\dot{Q}_{cd}^{(i+1)}(t_j) = k_f \left( \frac{T^i(t_j) - T^{(i+1)}(t_j)}{h_f} \right) b \cdot a \quad i = 1, \dots, n-1 \quad (6.3)$$

where  $\dot{Q}_{cu}^i = -\dot{Q}_{cd}^{(i+1)}$  are the vertical heat conductions through the fibres,  $k_f$  is the conductivity of the fibre and  $h_f$  is the thickness of the fibre layer.

- Equation used to model the conduction inside the resin, along the  $x$  axis direction (this conduction will be named later, in Figure 6.3, as lateral conduction):

$$\dot{Q}_{cl}^i(t_j) = k_r \left( \frac{T_0 - T^i(t_j)}{d_c} \right) 2 \cdot h_r \cdot a \quad i = 1, \dots, n \quad (6.4)$$

where  $\dot{Q}_{cl}^i$  is the lateral heat conduction through the resin,  $k_r$  is the conductivity of the resin,  $d_c$  is the distance from the border of the resin control volume to the zone in which the laminate remains at room temperature (estimated in two times the thickness of the laminate) and  $h_r$  is the thickness of the resin layer.

## 6.4 Algorithm for solving the heat generation-distribution problem

As mentioned above, due to the strong coupling that exists between the layers, an incremental algorithm is needed to solve the problem. The algorithm is described next step by step:

Step 1: Initially, the temperature of all layers is known.  $T^i(t_1) = T_0 = 298 K$  with  $i = 1, \dots, n$ , the time at the beginning of the first time step being  $t_1 = 0$ .

Step 2: From the temperature of the layers,  $T^i(t_j)$ , the viscosity of each layer,  $\eta^i(t_j)$ , is calculated using (4.8), the time at the  $j$  time step being  $t_j$ .

Step 3: From the viscosities,  $\eta^i(t_j)$ , and the thicknesses of the layers,  $h^i$ , the damping functions  $S^i(t_j)$  are calculated using (5.44).

Step 4: With the viscosities,  $\eta^i(t_j)$ , the damping functions,  $S^i(t_j)$ , and the velocity of the sonotrode,  $w_{sv}(t_j) = \delta_v \omega \cos(\omega t_j)$ , the velocities of the layers,  $v^i(t_j)$ , are calculated using (5.41)-(5.43).

Step 5: The heats generated at each layer during the step,  $\dot{Q}_{gen\_h}^i(x, y, t_j)$  and  $\dot{Q}_{gen\_v}^i(x, y, t_j)$ , are calculated with the velocities and viscosities of the layers using Equations (5.51) and (5.45), respectively.

Step 6: The heat generated is integrated in the resin volumes,  $\dot{Q}_{gen\_m}^i(t_j)$ , using Equation (6.1).

Step 7: The heat transfers of the laminate,  $\dot{Q}_{cu}^i(t_j)$ ,  $\dot{Q}_{cd}^i(t_j)$  and  $\dot{Q}_{cl}^i(t_j)$ , are calculated at this step using Equations (6.2), (6.3) and (6.4).

Step 8: Since heating of the layers may be very fast, the length of the time step is calculated fixing the maximum temperature variation allowed in a layer during one load step as  $\Delta T_{\max} = 1K$ , as:

$$\Delta t(t_j) \leq \frac{\Delta T_{\max} \rho_r C_{Pr} V^i}{\max |\dot{Q}^i(t_j)|} \quad (6.5)$$

where  $V^i$  is the volume of each resin layer under the sonotrode,  $\rho_r$  is the density of the resin,  $C_{Pr}$  is the specific heat capacity at constant pressure of the resin and  $\dot{Q}^i(t_j)$  is the total heat in each layer:

$$\dot{Q}^i(t_j) = \dot{Q}_{gen\_m}^i(t_j) + \dot{Q}_{cu}^i(t_j) + \dot{Q}_{cd}^i(t_j) + \dot{Q}_{cl}^i(t_j) \quad (6.6)$$

Another limit has also been employed for the maximum length of the time step:

$$\Delta t(t_j) \leq \frac{1}{10\omega} \quad (6.7)$$

in order to properly follow the oscillations of the sonotrode.

The minor of the two limits is that employed for each time step. At the beginning of the compaction process, the heating is very fast and (6.5) is the most restrictive time increment condition. Once the process has evolved and the temperatures begins to stabilize, (6.7) turns more restrictive and it is the expression that rules the time increment until the process ends.

Step 9: Using the time step and the total heat, presented in equation (6.6), the temperature increment in each layer is calculated using the equation that defines the heat absorbed:

$$\Delta T^i(t_j) = \left( \frac{\dot{Q}^i(t_j)}{\rho_r \cdot C_{Pr} \cdot V^i} \right) \Delta t(t_j) \quad (6.8)$$

Step 10: Having obtained the temperature increment, the temperature for the next step is calculated using:

$$T^i(t_{j+1}) = T^i(t_j) + \Delta T^i(t_j) \quad (6.9)$$

where  $t_{j+1} = t_j + \Delta t_j$ .

Then, the algorithm returns to Step 2 to continue the solution process. The algorithm stops when the final time is reached.

## 6.5 Implementation of the algorithm in Matlab

In this case, the problem will be solved semi-analytically, assuming that all unknowns only vary across the thickness direction of the laminate. The algorithm presented in section 6.4 has been implemented in the commercial mathematical programming software Matlab.

The resin layers under the sonotrode have been considered as separated volumes, related between them through the heat transfer equations, as shown in Figure 6.3.

Note that the heat transfers along the length of the laminate direction (marked as lateral conduction in Figure 6.3) will also be taken into account, introducing in this way 2D effects in the one direction solution.

As mentioned in Chapter 5, the horizontal component of the velocity of the sonotrode only affects the top layer, so the heat generation due to the horizontal movement (5.51) will only be applied to the volume that represents the top resin layer. On the contrary, the heat generation due to the vertical movement (5.45) is transmitted to all layers and thus it will be applied to all volumes.

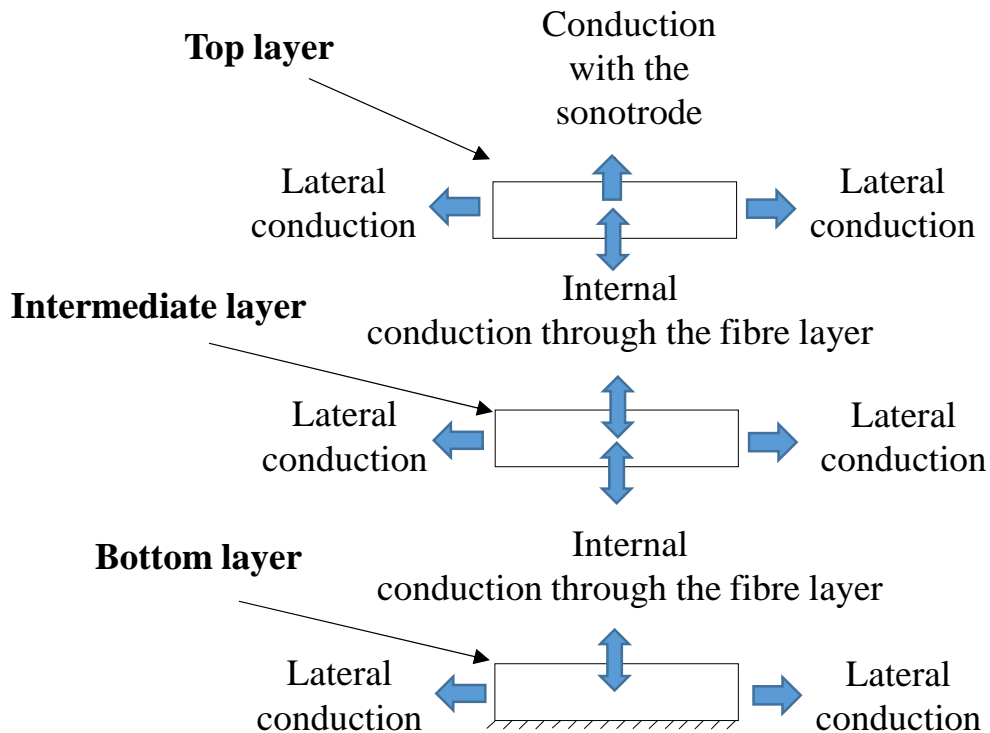


Figure 6.3. Scheme of the resin layers for the 1D model

## 6.6 Results

The results obtained with the model presented in this Chapter will be presented next. The evolution of the temperature with time during the compaction process will be shown. Then, a comparison between the results obtained with the pre-preg hypotheses presented in section 6.1 will be posed. Finally, the model will be compared with the experimental result presented in Chapter 2, Section 2.2.

### 6.6.1 Results of the model

The compaction process has been simulated for 8 composite plies, subjected to ultrasonic vibrations during 10 seconds. The following results have been obtained using the first hypothesis described in section 6.1, the laminate consisting on 9 resin layers separated by 8 fibre layers. The comparison between the results obtained with both hypotheses will be carried out at the end of this section.

The main dimensions of the model are:  $l_s = 20$  mm and the total thickness  $H = 1.04$  mm, which determine the size of the resin volumes. In this way, the area is  $20 \times 0.0325$  mm<sup>2</sup> for the upper and lower resin volumes and  $20 \times 0.065$  mm<sup>2</sup> for the intermediate resin volumes.

The evolution of the temperature with the time at the bottom layer is shown in Figure 6.4.

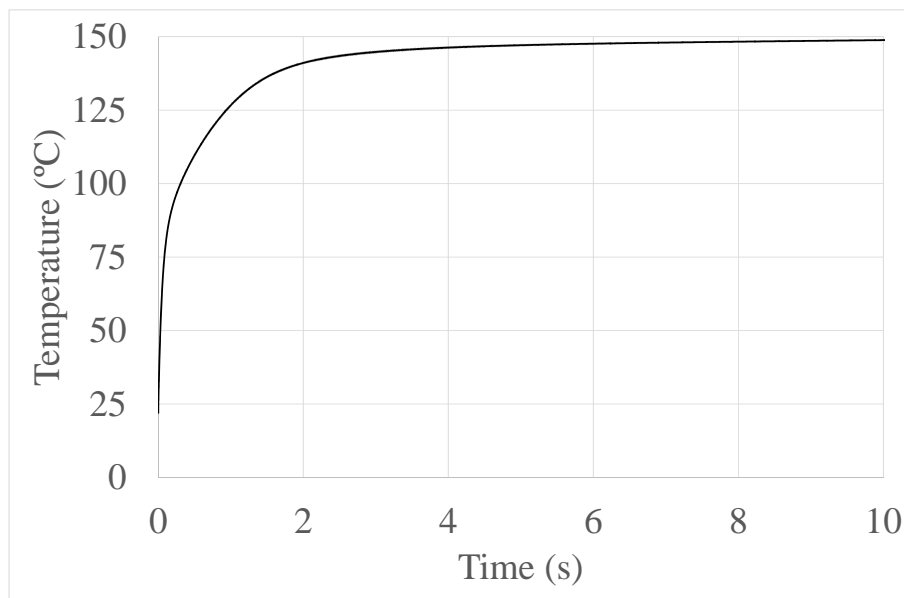


**Figure 6.4. Evolution of the temperature with the time at the bottom layer in the 1D semi-analytical model**

It can be appreciated that there is a very fast increment of the temperature of the resin at the beginning of the compaction process. After a transition phase in which the increment of the temperature decreases, a stabilization phase is reached, resulting in a very low temperature growth rate.

The evolution of the temperature can be explained studying the heat generated along the process. To this end, the evolution of the heat generated inside the bottom resin layer during the simulation is shown in Figure 6.5, presented dimensionless with reference to its maximum value,  $(Q^{visc})_{\max}$ .

The heat generated decreases very fast from its maximum, since the temperature of the resin is increased and, so, the viscosity of the resin decreases. At a certain value, the rate of the heat generated is stabilized, its evolution (and, because of that, the evolution of the temperature) being almost planar, but never reaching a plateau. This fact can be appreciated better in the enlarged view of Figure 6.6.

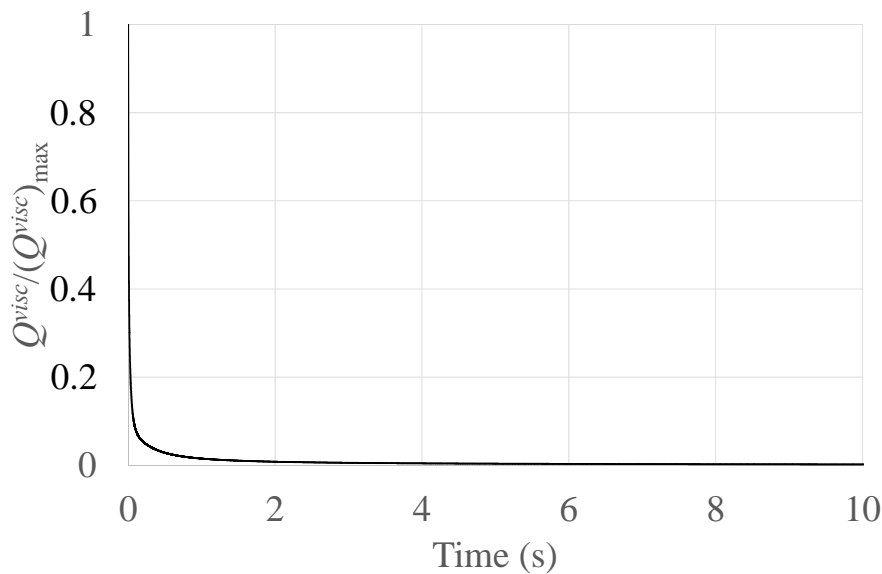


**Figure 6.5. Evolution of the heat generated during the compaction process in one layer, presented dimensionless**

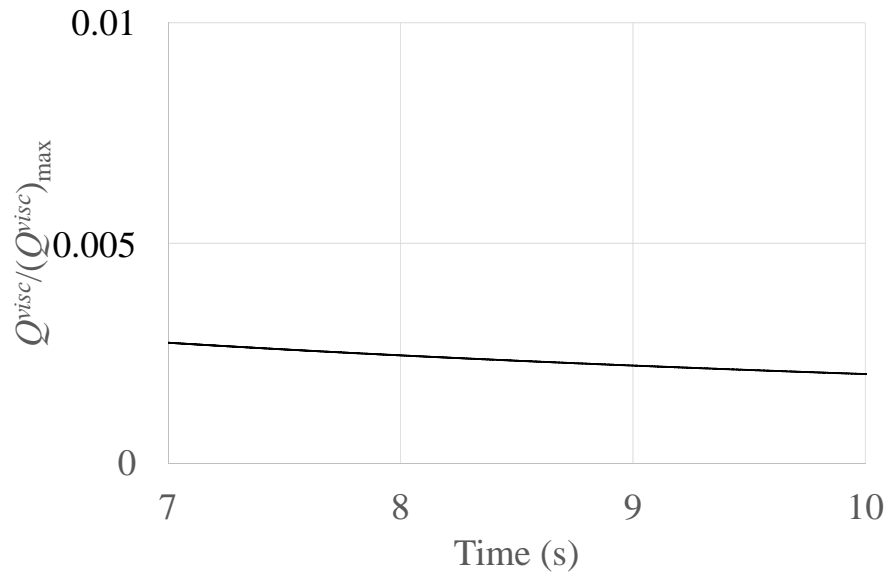


**Figure 6.6. Enlarged view of the evolution of the heat generated during the compaction process in one layer, presented dimensionless, from 7 to 10 seconds of the process**

### 6.6.2 Comparison of the pre-preg models

The problem presented in section 6.6.1, in which the first hypothesis for the pre-preg modeling (shown in Figure 6.1) was used, will be solved, in this section, using the second hypothesis, presented in Figure 6.2.

In this case, the 8-ply laminate is considered to be formed by 100 resin layers and 99 fibre layers.

The algorithm used to solve the problem is the one presented in section 6.3, as done with the previous hypothesis.

The main dimensions of the model are, again:  $l_s = 20$  mm and the total thickness  $H = 1.04$  mm, which determine the size of the resin volumes. In this case, the area of all resin volumes is the same, and equal to  $20 \times 7 \times 10^{-3}$  mm<sup>2</sup>.

The evolution of the temperature with the time at the bottom layer is shown in Figure 6.7.

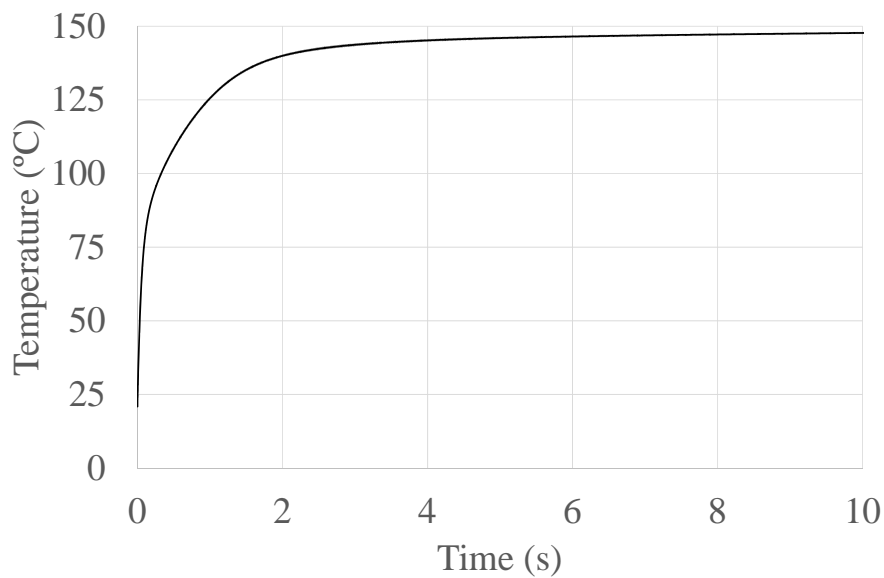


**Figure 6.7. Evolution of the temperature with the time at the bottom layer in the 1D semi-analytical model**

In order to compare the pre-preg models, the results obtained with both hypotheses of the evolution of the temperature during the compaction process are shown in Figure 6.8.

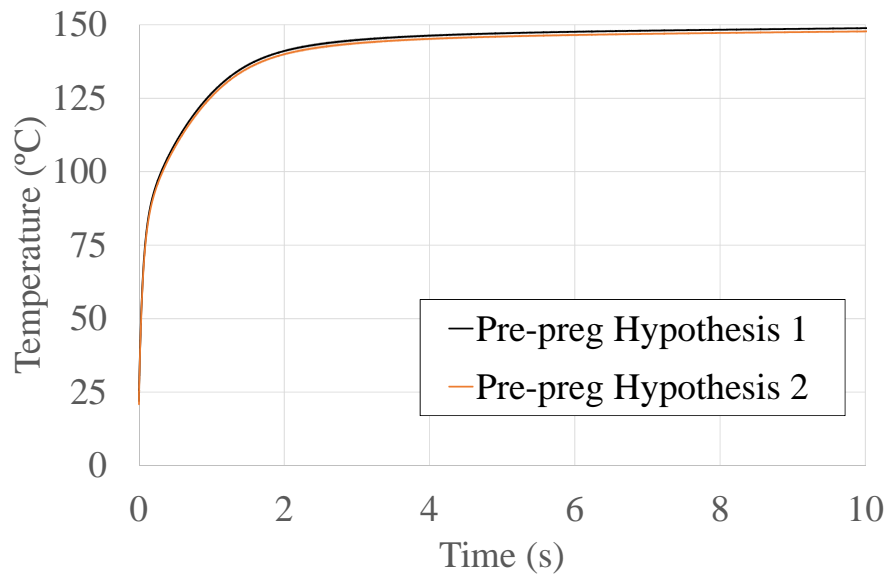


**Figure 6.8. Evolution of the temperature with the time at the bottom layer in the 1D semi-analytical model**

It can be appreciated that both models obtain almost the same results. The reason can be that, although the resin volumes are different and so the heat generated in each of them, the total heat is equivalent, leading to obtain the same thermal field. This result validates the use, from now on, of the first hypothesis, that requires less resources, from the computational point of view.

### 6.6.3 Experimental comparison

In order to check the validity of the thermomechanical model, developed in Chapter 5, and the resolution developed in this Chapter, a comparison with the experiment presented in Chapter 2, Section 2.2, has been carried out. The pre-preg model used, as mentioned in previous section, is the corresponding with the first hypothesis.

The evolution of the temperature with the time given by the experimental and semi-analytical curves is shown in Figure 6.9.

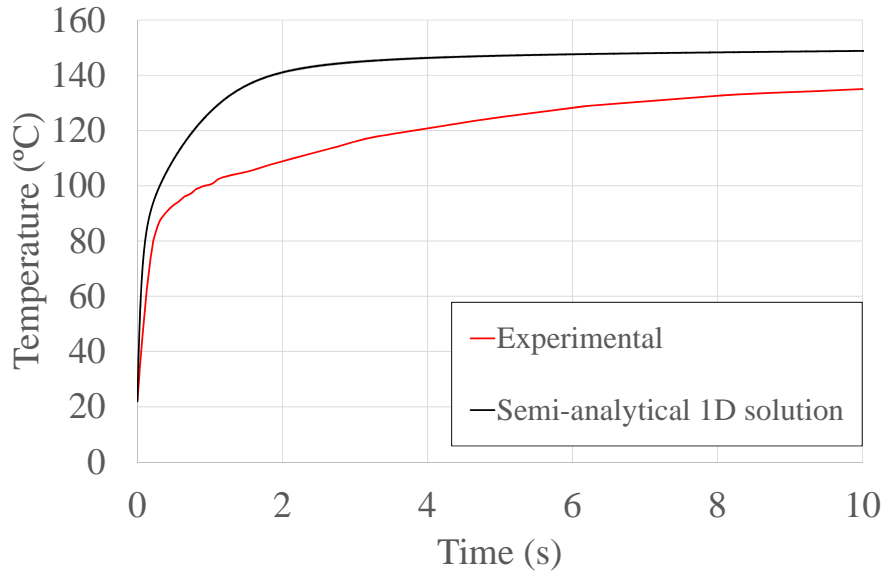


**Figure 6.9. Comparison between the time/temperature experimental and semi-analytical curves**

It can be appreciated that the model estimates, qualitatively speaking, the behavior of the evolution of the temperature. The differences appreciated can be due to the following reason: in the case of the 1D semi-analytical solution, the Fourier 1D equations used to calculate the heat transfers in two directions underestimate the heat transferred throughout the material (because the interactions that appear along the other direction are not taken into account). This fact leads to obtain a temperature inside the laminate higher than the real one.

## 6.7 Conclusions

A semi-analytical model capable to estimate the heat generation and distribution during the compaction process has been developed. After discussing two possible ways of modelling the pre-preg composite plies, the equations that

govern, in this case, the heat generation and the heat transfers (heat conductions and heat convections) have been presented.

Due to the non linear nature of the problem, an incremental algorithm that couples the generation and distribution of heat has been posed. The considerations made for the implementation of this algorithm in a 1D semi-analytical model has been presented.

The evolution of the temperature inside the laminate has been obtained during the whole compaction process. The behavior of the temperature has been explained with the representation of the evolution of the heat generated, that becomes almost null when the temperature has grown over a determined value.

A comparison between the temperature evolutions obtained with the two pre-preg models has shown that they provide similar results. This comparison validates the use of the first pre-preg hypothesis, that is faster to solve and less costly to implement, since the geometry discretization point of view. In this way, the models presented in next chapters will consider only the first hypothesis.

The comparison between the experiments and the model proposed in this Chapter has not permitted to check that the heat generation model estimates the value of the heat generated properly. The semi-analytical method is very fast to compute, but, although it estimates the behavior of the temperature with qualitatively good accuracy, it does not model the heat distribution properly, the predictions being significantly higher than those experimentally obtained.

The validity of the heat generation model will be checked with the models presented in next Chapters.

## Bibliography

[6.1] Mathworks: *Matlab User's Guide* (R2011b), The Mathworks, Inc. (2011).

[6.2] Mazumdar, S.K.: *Composites Manufacturing. Materials, Product, and Process Engineering*. CRC Press. (2002).

# *Chapter 7*

## *2D FEM model*

The effectiveness of the heat generation model presented in Chapter 5 could not be checked with the semi-analytical model presented in Chapter 6, due to the simplicity of the approximations made in the calculations of the heat distribution. In order to prove the validity of the equations presented in Chapter 5, a 2D FEM model that implements the heat generation has been developed. This model has been programmed into the commercial FEM program ANSYS® [7.1], that will be used to solve the heat distribution equations during the compaction process. The model and the results obtained with it will be explained in this Chapter.

First, several considerations about the heat generation and distributions models assumed will be commented.

In the second section, an incremental algorithm will be presented. The algorithm has been developed to solve the coupling between the heat generation and distribution mechanisms.

In section 7.3, the geometry and the mesh used to model the problem in the FEM program are shown. Several remarks about the possibilities to use a fine mesh and a fine discretization in time will be done.

The results obtained with the model are presented in section 7.4, in which a comparison of the results with experimental results will also be carried out. The considerations concerning the mesh and the time step chosen previously presented will be discussed.

Finally, the conclusions related to the 2D FEM model and the results presented in this Chapter will be shown.

## 7.1 Heat generation and distribution modelling

In the model presented in this Chapter, a commercial FEM program will solve the heat distribution. The FEM solver takes into account the possible interactions of the heat flows along the  $x$  and  $y$  axis. Thus, this approach is supposed to give more accurate results than the one done in Chapter 6.

In the case of the heat generation, as done in Chapter 6, see Equation (6.1), the heat generation equations obtained in Chapter 5 will be integrated in the resin volumes, as the heat inside the resin is supposed to be homogenized very fast:

$$\dot{Q}_{gen\_m}^i(t_j) = \int_{-L_s/2}^{L_s/2} \int_{-h^i/2}^{h^i/2} [\dot{Q}_{gen\_h}^i(x, y, t_j) + \dot{Q}_{gen\_v}^i(x, y, t_j)] dy dx \quad (7.1)$$

The heats generated due to the horizontal,  $\dot{Q}_{gen\_h}^i(x, y, t_j)$ , and vertical,  $\dot{Q}_{gen\_v}^i(x, y, t_j)$ , components of the displacement of the sonotrode are calculated using Equations (5.41), (5.51) and related, shown in Chapter 5.

As remarked in Chapter 6, the calculation of the heats generated in each resin layer involve the use of the temperatures of the other resin layers so the heat generation-distribution problem is coupled.

## 7.2 Algorithm for solving the heat generation-distribution problem

As mentioned above, due to the strong coupling that exists between the layers when solving the heat generation-distribution, an incremental algorithm is needed to solve the problem. The algorithm is described next step by step. Note that the first steps remains equal than in the algorithm shown in Chapter 6.

Step 1: Initially, the temperature of all layers is known.  $T^i(t_1) = T_0 = 298 K$ ,  $i = 1, \dots, n$ , the time at the beginning of the first time step being  $t_1 = 0$ .

Step 2: From the temperature of the layers,  $T^i(t_j)$ , the viscosity of each layer,  $\eta^i(t_j)$ , is calculated using (4.8), the time at the  $j$  time step being  $t_j$ .

Step 3: From the viscosities,  $\eta^i(t_j)$ , and the thicknesses of the layers,  $h^i$ , the damping functions  $S^i(t_j)$  are calculated using (5.44).

Step 4: With the viscosities,  $\eta^i(t_j)$ , the damping functions,  $S^i(t_j)$ , and the velocity of the sonotrode,  $w_{sv}(t_j) = \delta_v \omega \cos(\omega t_j)$ , the velocities of the layers,  $v^i(t_j)$ , are calculated using (5.41)-(5.43).

Step 5: The heats generated at each layer during the step,  $\dot{Q}_{gen\_h}^i(x, y, t_j)$  and  $\dot{Q}_{gen\_v}^i(x, y, t_j)$ , are calculated with the velocities and viscosities of the layers using (5.41) and (5.51).

Step 6: The heats generated are integrated to obtain the heat generated in the resin volume, using (7.1).

Step 7: A FEM model is created to calculate the heat transfers that take place in the laminate. The initial temperature is defined in the nodes and the heat generated is introduced as a heat source in the elements of the resin layers located under the sonotrode.

Step 8: In order to calculate the time step, as done in Chapter 6, two possible time steps are used, one time step related with the oscillations of the sonotrode and one time step related with the maximum temperature increment allowed. The time step related with the oscillations of the sonotrode (where  $f$  is the ultrasonic frequency) is calculated using:

$$\Delta t_f(t_j) \leq \frac{1}{10f} \quad (7.2)$$

However, in the case of the time step related with the temperature increment, its calculation cannot be done directly, due to the fact that, in this case, not all the heats involved in the process are calculated analytically (note that the heat transfers are calculated by the FEM program). As only the heat generated in each resin layer is well known, to set the maximum temperature increment (1K) in a load step, steps 9 and 10 are used.

Step 9: The heat balance equation is solved by the FEM program, using the length of the time step given by (7.2). It leads to obtain the temperatures at the end of the time step due to the oscillations of the sonotrode,  $T^i(t_j + \Delta t_f(t_j))$ .

Step 10: If the maximum temperature increment,  $\Delta T_{\max}$ , is higher than 1K, assuming the linearity of the solution, the temperatures at the end of the time step are recalculated using:

$$T^i(t_{j+1}) = T^i(t_j) + \frac{T^i(t_j + \Delta t_f(t_j)) - T^i(t_j)}{\Delta T_{\max}} \quad (7.3)$$

where  $t_{j+1} = t_j + \Delta t(t_j)$  with  $\Delta t(t_j) = \frac{\Delta t_f(t_j)}{\Delta T_{\max}}$ .

Then, the algorithm returns to Step 2 to continue the solution process. The algorithm stops when the final time is reached.

### 7.3 Geometry and mesh

The geometry and the mesh of the FEM model developed are shown in Figure 7.1 and represents the sonotrode over 8 uncured pre-preg plies of a total length of 25 mm.

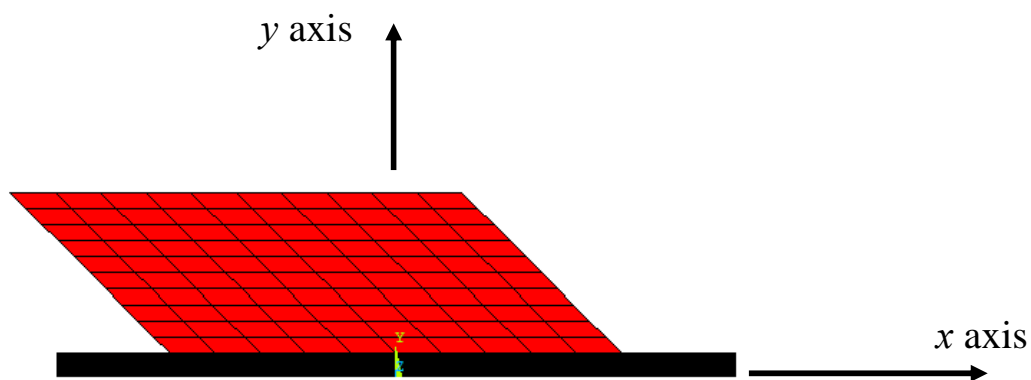


**Figure 7.1. View of the mesh used for the laminate and the sonotrode in the 2D FEM resolution of the compaction problem**

In this case, the laminate has not been considered longer because the zone influenced by the heating is very small, reducing in this way the number of elements along the  $x$  axis that are not located under the sonotrode.

In order to show the mesh of the plies in a better way, a detailed view of Figure 7.1 is shown in Figure 7.2.

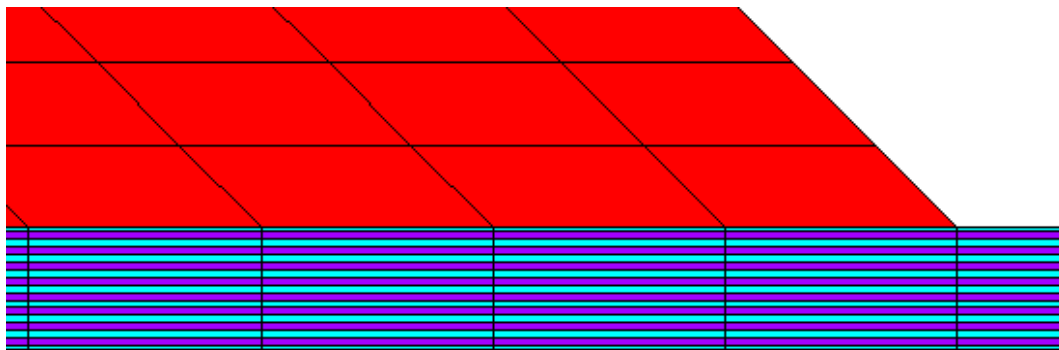


**Figure 7.2. Detail of the mesh used for the laminate and the sonotrode in the 2D FEM resolution of the compaction problem**

As can be appreciated, there are huge differences between the dimensions of the problem throughout the  $x$  axis and the  $y$  axis, since the thickness of the resin layers is less than  $10^{-3}$  times the width of the sonotrode. This fact makes it difficult to obtain a reasonable mesh, in terms of number of elements with good aspect ratio versus computation time (in Figure 7.2 is shown a mesh with 1 element in the thickness of each resin or fibre layer and 10 elements in the length direction below the sonotrode; the distortion of the elements being easily appreciated).

The resolution of the problem has been carried out using several meshes in order to check the convergence of the solution, modifying the number of elements along the  $x$  axis under the sonotrode.

The mesh that models the sonotrode has been made using the same number of elements along the  $x$  axis as for the laminate, obtaining in this way a congruent

mesh along the  $x$  axis. The number of elements along the  $y$  axis has been selected in order to obtain elements with a little distortion.

In the case of the zones of the laminate that are not placed under the sonotrode (and, for this reason, do not generate heat), the mesh is formed by one element per layer along the  $y$  axis and just a few elements along the  $x$  axis. This election has been made in order to obtain a coherent mesh but not incrementing the computation cost in a zone that will not contribute significantly to the solution.

Another difficulty that has been found during the solution of the problem is the difference in the time scales, one concerning the process time (of the order of 10 seconds) and another concerning the ultrasonic vibration (of the order of  $10^{-6}$  seconds). The number of time steps needed to solve the whole problem with a fine discretization of the ultrasonic wave is higher than 500000 steps, impeding to obtain the solution in a reasonable computing time. Due to this fact, in order to obtain the solution along the whole process and to compare with the semi-analytical model and the experiments, several less restrictive limits for the time increment have been implemented, and will be detailed in next section.

## 7.4 Results

The evolutions of the temperature at a node located at the mid-point ( $x = 0, y = 0$ ) of the bottom layer of the laminate, under the sonotrode (in order to compare later this solution with that obtained in the previous section), are shown in Figure 7.3. The problem has been solved for a mesh with 10, 20, 40, 80 and 160 elements under the sonotrode in the  $x$  direction, in order to check the influence of the mesh size in the solution. Supposing that the time increment given by Equation (7.2) would not allow to obtain the solution along the whole process time (it would imply large computing times), the time increment has been fixed in 0.01 seconds. The influence of the time increment will be studied next.

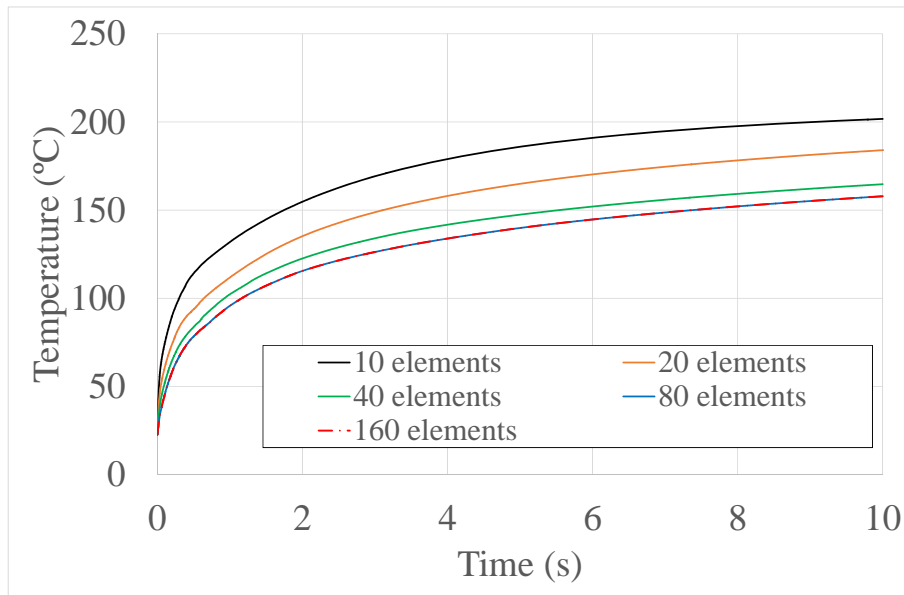


**Figure 7.3. Evolution of the temperature with the time at the middle of the bottom layer in the 2D FEM model for several number of elements along the  $x$  direction under the sonotrode**

It can be observed that the solution tends to converge when increasing the number of elements under the sonotrode in the longitudinal direction, obtaining in this way a smoother mesh.

In order to check the influence of the time increment limit, several values of it, which substitute the limit presented in Equation (7.2), are shown in Figure 7.4. In this case, the mesh for the laminate under the sonotrode consists on 1 element per thickness layer and 80 elements under the sonotrode along the  $x$  axis (note that the solution converged using this mesh, as could be seen in Figure 7.3). The time increment limits chosen are 0.1, 0.01, 0.001 and  $1/(10f)$  seconds. Note that the solution that uses the time increment defined by the sonotrode oscillation has been included, although only 0.4 seconds have been computed, due to the extreme time of computation (2 months running in a computer cluster of 16 nodes).

It can be appreciated that the evolution obtained is qualitatively quite similar to that obtained with the 1D semi-analytical model presented in Chapter 6, i. e., a

very fast increment of the temperature at the beginning and a stabilization of the temperature increment when the temperature reaches a certain value.

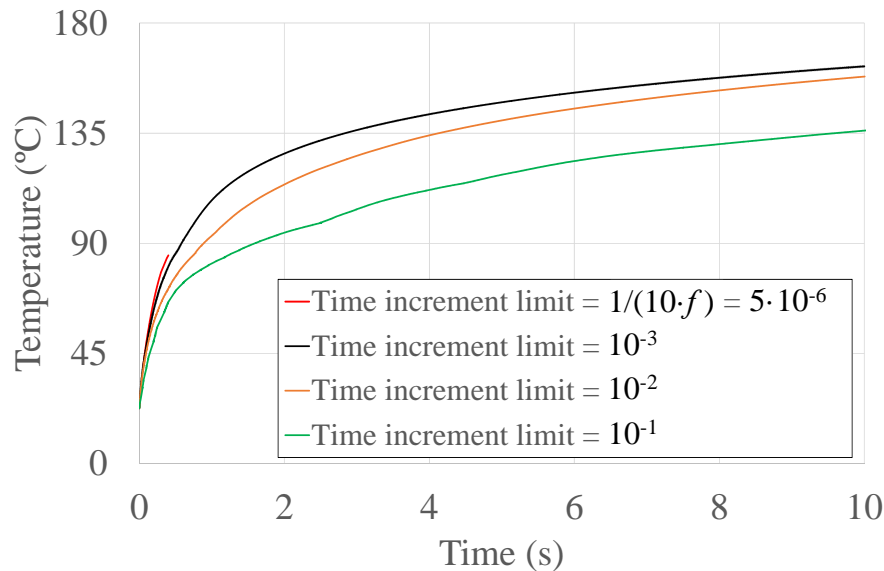


**Figure 7.4. Evolution of the temperature with the time at the middle of the bottom layer in the 2D FEM model for several values of the time increment limit**

In order to better appreciate the solution obtained with the time increment given by Equation (7.2), an enlarged view of the first second (in the  $x$  axis) of Figure 7.4 is shown in Figure 7.5.

When a high time increment is used, the excitation that is really being applied is a low frequency excitation (due to the aliasing phenomena), the heating obtained not being representative of the process. It can be seen that the solution obtained with Equation (7.2) follows the ultrasonic wave properly, as shown in the enlarged view of Figure 7.6.

The importance of an adequate selection of the time increment limit can be clearly observed from Figure 7.4. It can be seen that the solution converges when the time increment limit is decreased, tending to raise the temperature at which the thermal gradient begins to decrease.

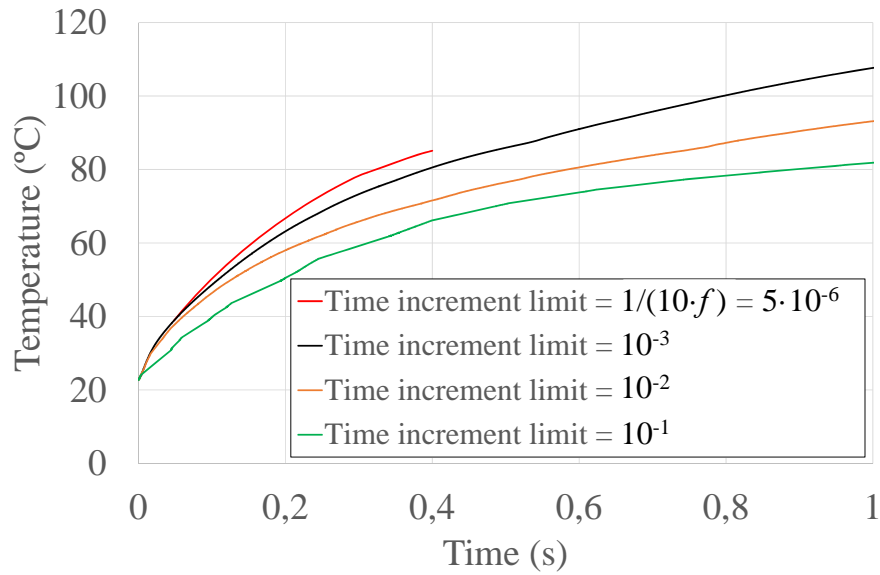


**Figure 7.5. Enlarged view of the evolution of the temperature with the time at the middle of the bottom layer in the 2D FEM model for several values of the time increment limit**

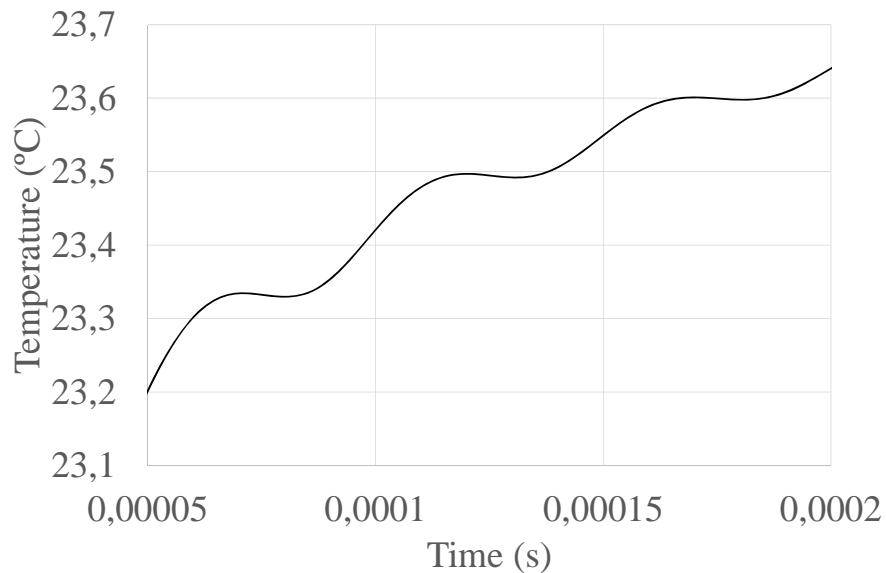


**Figure 7.6. Enlarged view of the evolution of the temperature with the time when using the time increment limit presented in (7.2)**

In order to check the validity of the thermomechanical model (developed in Chapter 5) and the resolution developed in this Chapter, a comparison with the experiment presented in Chapter 2, Section 2.2, has been carried out. The experimental and the finest 2D FEM solution curves are shown in Figure 7.7. In the case of the 2D FEM solution, it has been obtained using 80 elements under the sonotrode and the time increment limit described in Equation (7.2).

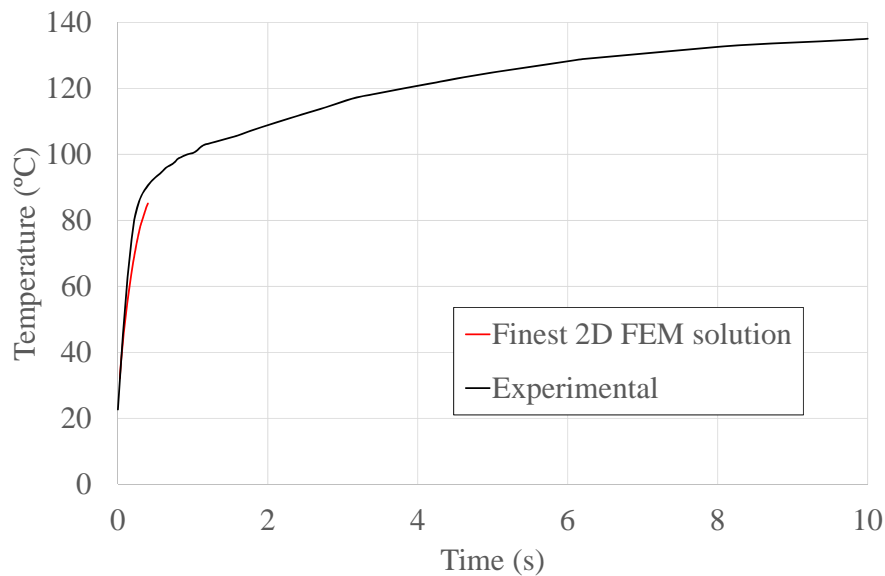


**Figure 7.7. Comparison of experimental and numerical 2D FEM temperature/time curve at the bottom of the laminate for a long process time**

In order to better appreciate the approximation of the finest FEM solution to the experimental results, an enlarged view of the first second (in the  $x$  axis) of Figure 7.7 is shown in Figure 7.8.

It can be appreciated that the finest FEM solution approximates properly the experimental measurements, at the range it has been computed.

Note that when a sufficiently fine mesh and an appropriate time increment are employed (finest 2D FEM solution) the FEM solution agrees much better with the experimental results. However, the computational costs associated make it very expensive to obtain the solution for a long process time.

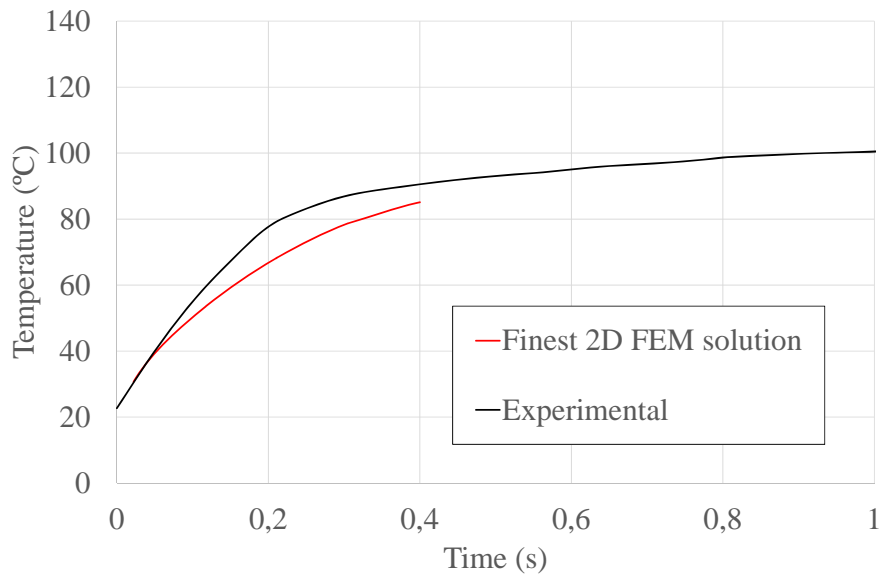


**Figure 7.8. Comparison of experimental and numerical 2D FEM temperature/time curve at the bottom of the laminate for a short process time**

## 7.5 Conclusions

As the semi-analytical model presented in Chapter 5 did not allow to obtain an accurate solution, a 2D FEM model capable to estimate the heat generation and distribution during the compaction process has been developed.

Initially, the equations that rule, in this case, the heat generation and the way of modelling the heat transfers have been presented. A FEM model has been employed to study the heat transfers and the temperature evolution in the laminate, in which the heat generation described in Chapter 5 has been included as an external heat source.

Due to the nonlinear nature of the problem, an incremental algorithm that couples the generation and distributions of heat has been posed.

The evolution of the temperature during the process has been obtained for various meshes (in order to check the convergence of the results) and for various time increment limits (due to the difficulty to solve the problem during the whole process with the time increment ruled by the sonotrode oscillations, less restrictive time limits having been tried).

The results obtained with this model and the difficulties to achieve an appropriate solution have been shown. In this case, comparing with the model shown in Chapter 6, the heat distribution can be modelled more correctly, if the mesh is fine enough. However, it has been checked that to obtain an appropriate solution with this FEM model, a very large computation time is required (as mentioned before, in our case, to compute 0.4 seconds, it was needed 2 months running in a computer cluster of 16 nodes), due to the fine mesh and the short time steps needed to properly follow the ultrasonic wave.

## **Bibliography**

[7.1] ANSYS, Inc.: *ANSYS User's Manual*. (2010)



# *Chapter 8*

## *PGD transient model*

The mechanism of generation of heat associated to the ultrasonic movement of the resin induced by the sonotrode oscillations has been studied and modeled in Chapter 5. The implementation of this heat generation model coupled with a thermal model to obtain the heat distribution was carried out in two ways of resolution in Chapter 6 and Chapter 7, respectively. Those models, (a 1D semianalytical model and a 2D FEM model) achieved to predict the shape of the real behavior of the temperature during the compaction process but presented several limitations. The main problems found were the large computing times that did not allow to obtain a complete solution (in the case of the 2D FEM model) and

the poorness of the equations to approximate the heat transfers in the thermal distribution (in the case of the 1D semi-analytical model).

To circumvent these problems, another resolution technique is presented. The alternative chosen is the Proper Generalized Decomposition (PGD) [8.1, 8.2, 8.3, 8.4, 8.5, 8.6, 8.7].

PGD is based on a separated representation of the unknown fields involved in the considered models. Thus, a solution depending on the space coordinates  $x$  and  $y$  and the time  $t$ , i.e.  $u(x, y, t)$ , that traditionally defines a 2D transient problem (that can be easily extended to the general 3D case), can be written as a finite sum of functional products, each one involving a function of the  $x$ -coordinate, a function of the  $y$ -coordinate and finally a time function. The space separation results particularly natural when the domain  $\Omega$  in which the problem is defined can be expressed as  $\Omega = \Omega_x \times \Omega_y$ , as is the case when addressing plates or laminates. As can be inferred from the approximation

$$u(x, y, t) \approx \sum_{l=1}^M X_l(x) \cdot Y_l(y) \cdot T_l(t)$$

the 2D transient solution only requires the solution of around  $3M$  one-dimensional problems for calculating functions  $X_l(x)$ ,  $Y_l(y)$  and  $T_l(t)$ . The number of problems to be solved is not exactly  $3M$  because the resulting problem is nonlinear (unknown functions  $X_l(x)$ ,  $Y_l(y)$  and  $T_l(t)$  appear multiplied in the solution approximation) and then an iterative procedure must be carried out for solving it.

In any case, if we imagine that these three functions are described from their values at certain points ( $N$  nodes in space for describing functions  $X_l(x)$  and  $Y_l(y)$  and  $P$  time instants), the computational complexity scales as  $M \times (P + 2N)$ . Now, we can compare such complexity with the usual transient solution, that would have require the solution of  $P$  (time instants) 2D problems of size  $N^2$ , which finally

results in a complexity scaling with  $P \times N^2$ . As in general  $M = N$ , the computing time savings can reach several orders of magnitude.

It is important to emphasize that within the space-time PGD the whole transient solution is being computed simultaneously, in the whole time interval. In the numerical solutions addressed in the present work, the number of time steps is around a half million and the meshes involves thousands of nodes. In this case the use of the PGD offers significant advantages.

First, in section 8.1, the equations that govern the heat generation and the heat distribution will be posed.

Second, in section 8.2, an algorithm to solve the coupled problem of heat generation due to the internal viscosity of the resin under ultrasonic loads (using the analytical equations presented in Chapter 5) and heat distribution inside the laminate (that will be solved using the PGD) will be explained.

Next, the formulation of the equations that solve the problem of the heat distribution with the PGD will be presented.

The results of the transient problem that describes the initial heating phase when the sonotrode is not moving along the laminate will be shown in section 8.4. The temperature inside the laminate during all the time of this process will be obtained.

Finally, the results of the transient model will be compared with experimental results, showing that it can predict the temperature reached in the laminate properly.

## 8.1 Heat generation and distribution modelling

The equations that will be used to solve the heat distribution and the heat generation will be presented next. Several considerations about the modelling of the pre-preg and its properties will also be done.

The thermal problem is defined by the heat equation:

$$\rho C_p \frac{\partial T}{\partial t} - \nabla \cdot (\mathbf{K} \nabla T) = \mathbf{Q}^{visc} \quad (8.1)$$

where  $T$  is the temperature field,  $t$  is the time of the process,  $\mathbf{Q}^{visc}$  is the heat generated in the resin due to its internal viscosity when is submitted to ultrasonic vibrations,  $\rho$  is the density of the material,  $C_p$  the specific heat capacity of the material and  $\mathbf{K}$  is the conductivity tensor.

The transient model will be defined in a plate domain, given by  $\Xi = \Omega_x \times \Omega_y \times \Gamma$ , with  $\Omega_x = [-\frac{1}{2}L, \frac{1}{2}L]$ ,  $\Omega_y = [0, H]$  and  $\Gamma = [0, t_{max}]$ , the maximum time of the process being  $t_{max}$ .

The laminate is considered to be composed of  $P$  different orthotropic layers, each one characterized by a well defined conductivity tensor  $\mathbf{K}_j$ , assumed constant in the layer thickness. In this way, a characteristic function representing the position of each layer can be defined:

$$\chi_j(y) = \begin{cases} 1 & y_j \leq y \leq y_{j+1} \\ 0 & otherwise \end{cases} \quad j = 1, \dots, P \quad (8.2)$$

where  $y_j$  and  $y_{j+1}$  are the bottom and top values of  $y$  coordinate in the  $j^{\text{th}}$  layer, respectively.

The laminate conductivity can be written in the following separated form using (2):

$$\mathbf{K}(x, y) = \sum_{j=1}^P \mathbf{K}_j(x) \chi_j(y) \quad (8.3)$$

In this work,  $\mathbf{K}$  has been assumed constant in each layer, so it does not depend on the  $x$  coordinate.

In the case of the other properties of the material,  $\rho$  and  $C_p$ , a similar separated form is applied.

$$\rho(x, y) = \sum_{j=1}^P \rho_j(x) \chi_j(y) \quad (8.4)$$

$$C_p(x, y) = \sum_{j=1}^P C_{p_j}(x) \chi_j(y) \quad (8.5)$$

The same idea can be applied to the heat generation, but using a function  $\gamma_j(y)$  equal to 1 in the resin layers and null in the fibre layers (in order to represent that the heat is only generated at the resin layers). The separated representation of the heat generated can be expressed as:

$$\mathbf{Q}^{visc}(x, y, t) = \sum_{j=1}^P \phi_j(x) \gamma_j(y) \mathcal{Q}_j(t) \quad (8.6)$$

Note that  $\phi_j(x)$  is a function that takes a value of 1 when  $x$  is located under the sonotrode and 0 when  $x$  is not located under the sonotrode.

The problem of the heat generation has been solved in Chapter 5. The equations that govern this generation are presented next. Note that the  $y'$  coordinate that appear in these equations is associated to each resin layer,  $-\frac{1}{2}h_j < y' < \frac{1}{2}h_j$ , with  $h_j$  being the thickness of layer  $j$ .

$$\begin{aligned}
Q_P(t) &= \int_{-\frac{1}{2}h_P}^{\frac{1}{2}h_P} \int_{-\frac{1}{2}L_S}^{\frac{1}{2}L_S} Q_P^h(x, y', t) dx dy' + \int_{-\frac{1}{2}h_P}^{\frac{1}{2}h_P} \int_{-\frac{1}{2}L_S}^{\frac{1}{2}L_S} Q_P^v(x, y', t) dx dy' \\
Q_j(t) &= \int_{-\frac{1}{2}h_j}^{\frac{1}{2}h_j} \int_{-\frac{1}{2}L_S}^{\frac{1}{2}L_S} Q_j^v(x, y', t) dx dy' \quad j = 1, \dots, P-1
\end{aligned} \tag{8.7}$$

where:

$$Q_P^h(x, y', t) = \eta_P(t) \left( \frac{w_{sh}(t)}{h_P} \right)^2 \tag{8.8}$$

$$Q_j^v(x, y', t) = \frac{144\eta_j(t)}{(h_j)^6} \left[ v_j \left( -\frac{1}{2}h_j, t \right) - v_j \left( \frac{1}{2}h_j, t \right) \right]^2 y'^2 x^2 \quad j = 1, \dots, P-1 \tag{8.9}$$

where  $Q_P^h(x, y', t)$  is the heat generated due to the horizontal movement of the sonotrode, only generated inside the top layer  $P$ ,  $Q_j^v(x, y', t)$  is the heat generated due to the vertical movement of the sonotrode,  $\eta_j(t)$  is the viscosity of the  $j$ th-layer,  $v_j$  is the vertical velocity of the resin layer at the extremes of the  $j^{\text{th}}$ -layer,  $h_j$  is the thickness of the  $j^{\text{th}}$ -layer and  $w_{sh}(t)$  is the horizontal component of the velocity of the sonotrode.

Note that the heat generation presents a strong coupling between the layers, through their vertical velocities.

## 8.2 Algorithm for solving the heat generation-distribution problem

As mentioned before, as the heat generation presents a strong coupling between the layers and with the heat distribution, this problem is going to be solved in two parts, iteratively, until reaching convergence.

The first part of the heat equation, corresponding to the heat distribution, i. e., left member of equation (8.1), will be solved with the PGD, assuming the values of the viscous heating to be known. The problem is solved for every spatial node in the laminate and for every time node. The equations used to solve this part of the problem will be described in Section 8.3.

The second part of the equation, corresponding to the heat generation, i. e., the right member of equation (8.1), will be solved using the equations (8.7), (8.8), (8.9) and derived, presented in Chapter 5, using the temperatures calculated with the PGD. As mentioned before, the heat generation phase only takes place in the resin layers in the zone located under the sonotrode.

In order to obtain the solution to this problem, using the procedures described before, an algorithm is presented next:

Step 1: Initially, the temperature at each spatial node and at each time node is supposed known and equal to the room temperature.

Step 2: With the temperature field assumed in step 1, the viscous heating induced by the ultrasonic vibration is calculated at every resin layer and at every time node using the procedure described in Chapter 5.

Step 3: The viscous heating matrix calculated in the previous step is used in the resolution of the heat distribution problem by solving equation (8.1) with the PGD. In this way, the value of the temperature at each spatial node and at each time node is obtained in this step.

Step 4: The heat generation in each resin layer is calculated again using the generation equations of Chapter 5. The temperatures used in this step are a mean of the temperatures of the nodes under the sonotrode of each resin layer, obtained in step 3.

Step 5: In the first iteration, the updated heat generation matrix is compared with the one obtained in step 2 and, if the difference is smaller than a certain tolerance, the algorithm stops. If not, the updated heat generation matrix is used to solve the thermal problem again with the PGD (step 3), and the algorithm continues until reaching convergence (i.e. until the difference between the heat generation matrix obtained in Step 4 in two consecutive iterations is smaller than the abovementioned tolerance), iterating between steps 3, 4 and 5.

Once finished, the algorithm returns the temperature field inside the laminate, at every node, during the compaction process.

### 8.3 PGD formulation of the heat distribution in laminates for a transient problem

The construction of the Proper Generalized Decomposition of the transient heat transfer model is illustrated in what follows.

The thermal equation that defines the problem was presented in Equation (1).

Assuming that the coordinate system is oriented with the principal directions of  $\mathbf{K}$ , this tensor becomes diagonal.

$$\mathbf{K} = \begin{pmatrix} k_x & 0 \\ 0 & k_y \end{pmatrix} \quad (8.10)$$

where  $k_x$  and  $k_y$  are its principal thermal conductivities.

In this coordinate system, Equation (1) writes:

$$\rho C_P \frac{\partial T}{\partial t} - k_x \frac{\partial^2 T}{\partial x^2} - k_y \frac{\partial^2 T}{\partial y^2} - \mathbf{Q}^{visc} = 0 \quad (8.11)$$

As mentioned in the previous section,  $\mathbf{Q}^{visc}$  is assumed to be known.

The initial temperature will be assumed to be known and equal to the room temperature,  $T_{amb}$ ,

$$T(x, y, t = 0) = T_{amb} \quad (8.12)$$

and the heat flux will be prescribed on the whole boundary  $\Phi = \partial(\Omega_x \times \Omega_y)$ ,  $\Phi = \Phi_1 \cup \Phi_2 \cup \Phi_3 \cup \Phi_4$ , the boundaries being  $\Phi_1 = (x = -\frac{1}{2}L, y \in \Omega_y)$ ,  $\Phi_2 = (x \in \Omega_x, y = 0)$ ,  $\Phi_3 = (x = \frac{1}{2}L, y \in \Omega_y)$ ,  $\Phi_4 = (x \in \Omega_x, y = H)$ . The boundary conditions of the problem are: isolation at  $\Phi_1$ ,  $\Phi_2$  and  $\Phi_3$  and conduction with the sonotrode/convection with the air (depending on the value of the  $x$  coordinate) at  $\Phi_4$ . These conditions can be expressed as:

$$\begin{aligned} \frac{\partial T}{\partial x} \Big|_{x,y \in \Phi_1} = 0, \quad \frac{\partial T}{\partial y} \Big|_{x,y \in \Phi_2} = 0, \quad \frac{\partial T}{\partial x} \Big|_{x,y \in \Phi_3} = 0 \\ -k_y \frac{\partial T}{\partial y} \Big|_{x,y \in \Phi_4} = \begin{cases} h \cdot (T(x, y = H, t) - T_{amb}) & x \in \Phi_4 - \Phi_4^s \\ h_s \cdot (T(x, y = H, t) - T_{amb}) & x \in \Phi_4^s \end{cases} \end{aligned} \quad (8.13)$$

where  $\Phi_4^s$  is the area of  $\Phi_4$  located under the sonotrode,  $h$  is the convection coefficient and  $h_s$  is a coefficient that determines the heat loss through the

sonotrode (this coefficient depends on the conductivity and the geometry of the sonotrode and has been calibrated experimentally).

The weighted residual form of equation (8.11) writes:

$$\int_{\Xi} T^* \left( \rho C_p \frac{\partial T}{\partial t} - k_x \frac{\partial^2 T}{\partial x^2} - k_y \frac{\partial^2 T}{\partial y^2} - \mathbf{Q}^{visc} \right) d\Xi = 0 \quad (8.14)$$

with the test function  $T^*$  being defined in an appropriate functional space.

To introduce the boundary conditions into the formulation, the equation will be solved integrating by parts the term that involves second order derivatives. Note that in all boundaries the integral is equal to zero, except in the upper boundary. In this zone conduction exists with the sonotrode, in  $\Phi_4^s$ , and convection exists with the air in the zones that are not located under the sonotrode, in  $\Phi_4 - \Phi_4^s$ .

$$\begin{aligned} & \int_{\Xi} T^* \rho C_p \frac{\partial T}{\partial t} d\Xi + \int_{(\Phi_4 - \Phi_4^s) \times \Gamma} T^* h (T(x, y = H, t) - T_{amb}) dxdt + \\ & + \int_{\Phi_4^s \times \Gamma} T^* h_s (T(x, y = H, t) - T_{amb}) dxdt + \int_{\Xi} k_x \frac{\partial T^*}{\partial x} \frac{\partial T}{\partial x} d\Xi + \\ & + \int_{\Xi} k_y \frac{\partial T^*}{\partial y} \frac{\partial T}{\partial y} d\Xi - \int_{\Xi} T^* \mathbf{Q}_j^{visc} d\Xi = 0 \end{aligned} \quad (8.15)$$

The solution  $T(x, y, t)$  is searched under the separated form:

$$T(x, y, t) \approx \sum_{l=1}^{l=M} X_l(x) \cdot Y_l(y) \cdot \Theta_l(t) \quad (8.16)$$

where  $X_l(x)$ ,  $Y_l(y)$  and  $\Theta_l(t)$  are the approximation functions to be determined iteratively during the solution of the problem.

In what follows the construction of one of such enrichment functions is illustrated. For this purpose, we assume that, at iteration  $m < M$ , the solution is already known:

$$T^m(x, y, t) \approx \sum_{l=1}^{l=m} X_l(x) \cdot Y_l(y) \cdot \Theta_l(t) \quad (8.17)$$

Thus, at the present iteration we look for the solution enrichment:

$$T^{m+1}(x, y, t) = T^m(x, z, t) + R(x) \cdot W(y) \cdot S(t) \quad (8.18)$$

The test function involved in the weak form of the thermal equation, (8.15), is searched under the form:

$$T^*(x, y, t) = R^*(x) \cdot W(y) \cdot S(t) + R(x) \cdot W^*(y) \cdot S(t) + R(x) \cdot W(y) \cdot S^*(t) \quad (8.19)$$

As the enrichment process is non-linear, the functions  $R(x)$ ,  $W(y)$  and  $S(t)$  are proposed to be searched by applying an alternating direction fixed point algorithm.

- First, assuming  $S(t)$  and  $W(y)$  to be known,  $R(x)$  is computed.
- Second,  $W(y)$  is updated from previous  $S(t)$  and the just updated  $R(x)$ .
- Third,  $S(t)$  is calculated with the previously calculated  $R(x)$  and  $W(y)$ .
- The process continues until reaching convergence.

The converged solutions allow the next term in the finite sums decomposition to be defined:  $X_{m+1}(x) = R(x)$ ,  $Y_{m+1}(y) = W(y)$  and  $\Theta_{m+1}(t) = S(t)$ .

In the following subsections the operations implied on each one of the just referred steps are illustrated.

### 8.3.1 Computing $R(x)$ from $W(y)$ and $S(t)$

When  $W(y)$  and  $S(t)$  are known, the test function (8.19) reduces to:

$$T^*(x, y, t) = R^*(x) \cdot W(y) \cdot S(t) \quad (8.20)$$

and the weak form (8.15) reduces to:

$$\begin{aligned} & \int_{\Xi} R^* W S \rho C_p \left( R W \frac{dS}{dt} \right) d\Xi + \int_{(\Phi_4 - \Phi_4^i) \times \Gamma} R^* W (H) Sh (R W (H) S - T_{amb}) dx dt + \\ & + \int_{\Phi_4^i \times \Gamma} R^* W (H) Sh_s (R W (H) S - T_{amb}) dx dt + \int_{\Xi} k_x \frac{dR^*}{dx} W S \frac{dR}{dx} W S d\Xi + \\ & + \int_{\Xi} k_y R^* \frac{dW}{dy} S R \frac{dW}{dy} S d\Xi = - \int_{\Xi} R^* W S \zeta^m d\Xi - \\ & - \int_{\Xi} \left( \frac{dR^*}{dx} W S \quad R^* \frac{dW}{dy} S \right) \xi^m d\Xi - \int_{(\Phi_4 - \Phi_4^i) \times \Gamma} R^* W (H) Sh \psi^m dx dt - \\ & - \int_{\Phi_4^i \times \Gamma} R^* W (H) Sh_s \psi^m dx dt \end{aligned} \quad (8.21)$$

where  $\zeta^m$ ,  $\xi^m$  and  $\psi^m$  are the residuals at enrichment step  $m$ :

$$\zeta^m = \sum_{i=1}^{l=m} \rho C_p X_l(x) Y_l(y) \frac{d\Theta_l(t)}{dt} - \mathbf{Q}^{visc}$$

$$\xi^m = \mathbf{K} \sum_{l=1}^{l=m} \begin{pmatrix} \frac{dX_l(x)}{dx} Y_l(y) \Theta_l(t) \\ X_l(x) \frac{dY_l(y)}{dy} \Theta_l(t) \end{pmatrix} \quad (8.22)$$

$$\psi^m = \sum_{l=1}^{l=m} X_l(x) Y_l(H) \Theta_l(t)$$

As all the functions involving coordinates  $y$  and  $t$  are known, they can be integrated in  $\Omega_y = [0, H]$  and  $\Gamma = [0, t_{\max}]$ . These integrations are presented next. Note that, in order to simplify the number of equations, (8.23) includes integrals in  $R$  that cannot be integrated at this moment, but will be used in subsequent computations (sections 3.1.2 and 3.1.3).

$$\begin{aligned} w_1 &= \int_{\Omega_y} W^2 dy & s_1 &= \int_{\Gamma} S \frac{dS}{dt} dt & r_1 &= \int_{\Omega_x} R^2 dx \\ w_2^l &= \int_{\Omega_y} W Y_l dy & s_2^l &= \int_{\Gamma} S \cdot \frac{d\Theta_l}{dt} dt & r_2^l &= \int_{\Omega_x} R \cdot X_l dx \\ & & s_3 &= \int_{\Gamma} S dt & & \\ w_3 &= \int_{\Omega_y} W dy & s_4 &= \int_{\Gamma} S^2 dt & r_3 &= \int_{\Omega_x} R dx \end{aligned} \quad (8.23)$$

Then we can define:

$$\mathbf{K}_x = \begin{pmatrix} \int_{\Omega_y} k_x W^2 dy \int_{\Gamma} S^2 dt & 0 \\ 0 & \int_{\Omega_y} k_z \left( \frac{dW}{dy} \right)^2 dy \int_{\Gamma} S^2 dt \end{pmatrix} \quad (8.24)$$

and

$$\xi_x^m = \sum_{l=1}^{l=m} \left( \begin{array}{cc} \left( \int_{\Omega_y} k_x W Y_l dy \int_{\Gamma} S \Theta_l dt & 0 \right) \\ 0 & \int_{\Omega_y} k_z \frac{dW}{dy} \frac{dY_l}{dy} dy \int_{\Gamma} S \Theta_l dt \end{array} \right) \begin{pmatrix} \frac{dX_l(x)}{dx} \\ X_l(x) \end{pmatrix} \quad (8.25)$$

$$\psi_x^m = \sum_{l=1}^{l=m} W(H) Y_l(H) \int_{\Gamma} S \Theta_l(t) dt (X_l(x))$$

Then, eq. (8.21) reduces to:

$$\begin{aligned} & \int_{\Omega_x} R^* w_1 s_1 \rho C_p R dx + \int_{\Omega_x - \Omega_s} R^* (W(H))^2 s_4 h R dx + \int_{\Omega_s} R^* (W(H))^2 s_4 h_s R dx + \\ & + \int_{\Omega_x - \Omega_s} R^* W(H) s_3 h (-T_{amb}) dx + \int_{\Omega_s} R^* W(H) s_3 h_s (-T_{amb}) dx + \\ & + \int_{\Omega_x} \left( \frac{dR^*}{dx} \quad R^* \right) \mathbf{K}_x \left( \frac{dR}{dx} \quad R \right) d\Xi = - \int_{\Omega_x} R^* \left( \sum_{l=1}^{l=m} w_2^l s_2^l \rho C_p X_l - w_3 s_3 \mathbf{Q}^{visc} \right) dx - \\ & - \int_{\Omega_x} \left( \frac{dR^*}{dx} \quad R^* \right) \xi_x^m dx - \int_{\Omega_x - \Omega_s} R^* h \psi_x^m dx - \int_{\Omega_s} R^* h_s \psi_x^m dx \end{aligned} \quad (8.26)$$

Equation (8.26) defines an elliptic steady-state boundary value problem (BVP) for the unknown function  $R$ , which can be solved by using a FE model with a 1D smooth mesh.

Once  $R(x)$  is obtained, the next step in the fixed point algorithm is the calculation of  $W(y)$ .

### 8.3.2 Computing $W(y)$ from $R(x)$ and $S(t)$

When  $R(x)$  and  $S(t)$  are known, the test function (8.19) reduces to:

$$T^*(x, y, t) = R(x) \cdot W^*(y) \cdot S(t) \quad (8.27)$$

and the weak form (8.15) reduces to:

$$\begin{aligned} & \int_{\Xi} RW^* S \rho C_p \left( RW \frac{dS}{dt} \right) d\Xi + \int_{(\Phi_4 - \Phi_4^*) \times \Gamma} RW^* (H) Sh (RW(H)S - T_{amb}) dx dt + \\ & + \int_{\Phi_4^* \times \Gamma} RW^* (H) Sh_s (RW(H)S - T_{amb}) dx dt + \int_{\Xi} k_x \frac{dR}{dx} W^* S \frac{dR}{dx} W S d\Xi + \\ & + \int_{\Xi} k_z R \frac{dW^*}{dy} S R \frac{dW}{dy} S d\Xi = - \int_{\Xi} RW^* S \zeta^m d\Xi - \\ & - \int_{\Xi} \left( \frac{dR}{dx} W^* S \quad R \frac{dW^*}{dy} S \right) \xi^m d\Xi - \int_{(\Phi_4 - \Phi_4^*) \times \Gamma} RW^* (H) Sh \psi^m dx dt - \\ & - \int_{\Phi_4^* \times \Gamma} RW^* (H) Sh_s \psi^m dx dt \end{aligned} \quad (8.28)$$

As all the functions involving the in-plane coordinate  $x$  and the time coordinate  $t$  are known, they can be integrated in  $\Omega_x = [-\frac{1}{2}L, \frac{1}{2}L]$  and  $\Gamma = [0, t_{\max}]$ . Thus, using the previous notation, we can define:

$$\mathbf{K}_y = \begin{pmatrix} \int_{\Omega_x} k_x \left( \frac{dR}{dx} \right)^2 dx \int_{\Gamma} S^2 dt & 0 \\ 0 & \int_{\Omega_x} k_y R^2 dx \int_{\Gamma} S^2 dt \end{pmatrix} \quad (8.29)$$

and

$$\xi_y^m = \sum_{l=1}^{l=m} \left( \begin{array}{cc} \left( \int_{\Omega_x} k_x \frac{dR}{dx} \frac{dX_l}{dx} dx \int_{\Gamma} S\Theta_l dt & 0 \\ 0 & \int_{\Omega_x} k_y R X_l dx \int_{\Gamma} S\Theta_l dt \right) \begin{pmatrix} Y_l(y) \\ \frac{dY_l(y)}{dy} \end{pmatrix} \end{array} \right)$$

$$\psi_y^m = h \sum_{l=1}^{l=m} \int_{\Omega_x - \Omega_s} R X_l(x) dx \int_{\Gamma} S\Theta_l(t) dt (Y_l(H)) \quad (8.30)$$

$$\psi_{ys}^m = h_s \sum_{l=1}^{l=m} \int_{\Omega_s} R X_l(x) dx \int_{\Gamma} S\Theta_l(t) dt (Y_l(H))$$

Then, eq. (8.28) reduces to:

$$\begin{aligned} & \int_{\Omega_y} W^* r_1 s_1 \rho C_p W dy + W^*(H) r_1|_{\Omega_x - \Omega_s} s_4 h W(H) + W^*(H) r_1|_{\Omega_s} s_4 h_s W(H) + \\ & + W^*(H) r_3|_{\Omega_x - \Omega_s} s_3 h(-T_{amb}) + W^*(H) r_3|_{\Omega_s} s_3 h_s(-T_{amb}) + \\ & + \int_{\Omega_y} \left( W^* \frac{dW^*}{dy} \right) \mathbf{K}_y \left( \frac{W}{dy} \right) dy = - \int_{\Omega_y} W^* \left( \sum_{l=1}^{l=m} r_2^l s_2^l \rho C_p Y_l - r_3 s_3 \mathbf{Q}^{visc} \right) dy - \\ & - \int_{\Omega_y} \left( W^* \frac{dW^*}{dy} \right) \xi_y^m dy - W^*(H) (\psi_y^m + \psi_{ys}^m) \end{aligned} \quad (8.31)$$

where  $r_1|_{\Omega_x - \Omega_s}$  denotes that the integral  $r_1$  is evaluated in  $\Omega_x - \Omega_s$ .

Equation (8.31) defines a one-dimensional BVP that can be solved with FEM using a 1D smooth mesh.

Once  $W(y)$  is obtained, the next step in the fixed point algorithm is the calculation of  $S(t)$ .

### 8.3.3 Computing $S(t)$ from $R(x)$ and $W(y)$

When  $R(x)$  and  $W(y)$  are known, those obtained in Sections 8.3.1 and 8.3.2, the test function (8.19) writes:

$$T^*(x, y, t) = R(x) \cdot W(y) \cdot S^*(t) \quad (8.32)$$

and the weak form (8.15) reduces to:

$$\begin{aligned} & \int_{\Xi} RWS^* \rho C_p \left( RW \frac{dS}{dt} \right) d\Xi + \int_{(\Phi_4 - \Phi_4^i) \times \Gamma} RW(H)S^* h (RW(H)S - T_{amb}) dxdt + \\ & + \int_{\Phi_4^i \times \Gamma} RW(H)S^* h_s (RW(H)S - T_{amb}) dxdt + \int_{\Xi} k_x \frac{dR}{dx} WS^* \frac{dR}{dx} WS d\Xi + \\ & + \int_{\Xi} k_y R \frac{dW}{dy} S^* R \frac{dW}{dy} S d\Xi = - \int_{\Xi} RWS^* \zeta^m d\Xi - \\ & - \int_{\Xi} \left( \frac{dR}{dx} WS^* \quad R \frac{dW}{dy} S^* \right) \xi^m d\Xi - \int_{(\Phi_4 - \Phi_4^i) \times \Gamma} RW(H)S^* h \psi^m dxdt - \\ & - \int_{\Phi_4^i \times \Gamma} RW(H)S^* h_s \psi^m dxdt \end{aligned} \quad (8.33)$$

As all the functions involving the in-plane coordinate  $x$  and the thickness coordinate  $y$  are known, they can be integrated in  $\Omega_x = [-\frac{1}{2}L, \frac{1}{2}L]$  and  $\Omega_y = [0, H]$ . Thus, using the previous notation, we can define:

$$\mathbf{K}_t = \begin{pmatrix} \int_{\Omega_x} k_x \left( \frac{dR}{dx} \right)^2 dx \int_{\Omega_y} W^2 dy & 0 \\ 0 & \int_{\Omega_x} k_y R^2 dx \int_{\Omega_y} \left( \frac{dW}{dy} \right)^2 dy \end{pmatrix} \quad (8.34)$$

and

$$\xi_t^m = \sum_{l=1}^{l=m} \left( \begin{array}{cc} \int_{\Omega_x} k_x \frac{dR}{dx} \frac{dX_l}{dx} dx \int_{\Omega_y} W Y_l dy & 0 \\ 0 & \int_{\Omega_x} k_z R X_l dx \int_{\Omega_y} \frac{dW}{dy} \frac{dY_l}{dy} dy \end{array} \right) \begin{pmatrix} \Theta_l(t) \\ \Theta_l(t) \end{pmatrix}$$

$$\psi_t^m = h \sum_{l=1}^{l=m} W(H) Y_l(H) \int_{\Omega_x - \Omega_s} R X_l(x) dx (\Theta_l(t)) \quad (8.35)$$

$$\psi_{ts}^m = h_s \sum_{l=1}^{l=m} W(H) Y_l(H) \int_{\Omega_s} R X_l(x) dx (\Theta_l(t))$$

Then, eq. (8.33) reduces to

$$\int_{\Gamma} S^* r_1 w_1 \rho C_p \frac{dS}{dt} dt + \int_{\Gamma} S^* r_1|_{\Omega_x - \Omega_s} (W(H))^2 h S dt + \int_{\Gamma} S^* r_1|_{\Omega_s} (W(H))^2 h_s S dt +$$

$$+ \int_{\Gamma} S^* r_3|_{\Omega_x - \Omega_s} W(H) h (-T_{amb}) dt + \int_{\Gamma} S^* r_3|_{\Omega_s} W(H) h_s (-T_{amb}) dt +$$

$$+ \int_{\Gamma} (S^* \quad S^*) \mathbf{K}_t \begin{pmatrix} S \\ S \end{pmatrix} dt = - \int_{\Gamma} S^* \left( \sum_{l=1}^{l=m} r_2^l w_2^l \rho C_p \frac{d\Theta_l}{dt} - r_3 w_3 \mathbf{Q}^{visc} \right) dt -$$

$$- \int_{\Gamma} (S^* \quad S^*) \xi_t^m dt - \int_{\Gamma} S^* (\psi_t^m + \psi_{ts}^m) dt \quad (8.36)$$

Equation (8.36) represents the weak form of the ordinary differential equation (ODE) defining the time evolution of the field  $S$ , which can be solved by using any stabilized discretization technique.

As all the functions of (8.36) does not involve derivatives of  $S^*$ , it is possible to come back to its strong form:

$$\begin{aligned}
& r_1 w_1 \rho C_P \frac{dS}{dt} + r_1 \Big|_{\Omega_x - \Omega_s} (W(H))^2 h S + r_1 \Big|_{\Omega_s} (W(H))^2 h_s S + \\
& + r_3 \Big|_{\Omega_x - \Omega_s} W(H) h (-T_{amb}) + r_3 \Big|_{\Omega_s} W(H) h_s (-T_{amb}) + \mathbf{K}_t \begin{pmatrix} S \\ S \end{pmatrix} = \quad (8.37) \\
& - \left( \sum_{l=1}^{l=m} r_2^l w_2^l \rho C_P \frac{d\Theta_l}{dt} - r_3 w_3 \mathbf{Q}^{visc} \right) - \xi_t^m - (\psi_t^m + \psi_{ts}^m)
\end{aligned}$$

Equation (8.37) defines an initial value problem (IVP) for the unknown function  $S$  that can be solved by using standard backward finite differences or higher order Runge-Kutta schemes.

## 8.4 Results

The problem that will be studied in this section is the compaction of 8 uncured plies with the sonotrode placed over a certain zone of the laminate during a certain time. In this procedure, the sonotrode is only vibrating, without any displacement along the laminate.

In this case, the problem is going to be studied from the initial conditions, when the sonotrode begins to actuate, until reaching a certain process time, when the sonotrode is lifted. In these conditions, the compaction process has been studied as a transient problem.

The problem has been solved with the PGD using the formulation presented in Section 8.3, where the applied boundary conditions were also specified.

The mesh used consists on 100 nodes for the length of the laminate, along the  $x$  axis (being  $L = 60$  mm ), 321 nodes for the thickness of the laminate, along

the  $y$  axis (being  $H = 1.04$  mm ) and 500000 nodes on the time axis (being  $t_{\max} = 10$  seconds). The length of the sonotrode on the  $x$  axis is  $L_s = 20$ mm.

The convergence of the PGD resolution was reached after adding 24 sums of products of functions  $X_l(x)Y_l(y)\Theta_l(t)$ . The evolution of the functions  $X_l(x)$ ,  $Y_l(y)$  and  $\Theta_l(t)$  with their respective coordinates can be seen in Appendix I.

In order to check how the solution is approximated when adding several products of functions  $X_l(x)Y_l(y)\Theta_l(t)$ , the evolutions of the temperature along the  $x$  axis, along the  $y$  axis and along the time axis are shown next, respectively.

The curve shown in Figure 8.1, which represents the evolution of the temperature along the  $x$  axis, has been obtained for a value of the time  $t = 1.5$  seconds and at the line of nodes located at the bottom of the laminate ( $y = 0$ ). The curves represent the solution given by Equation (8.16) from  $M=1$  to  $M = 24$ .

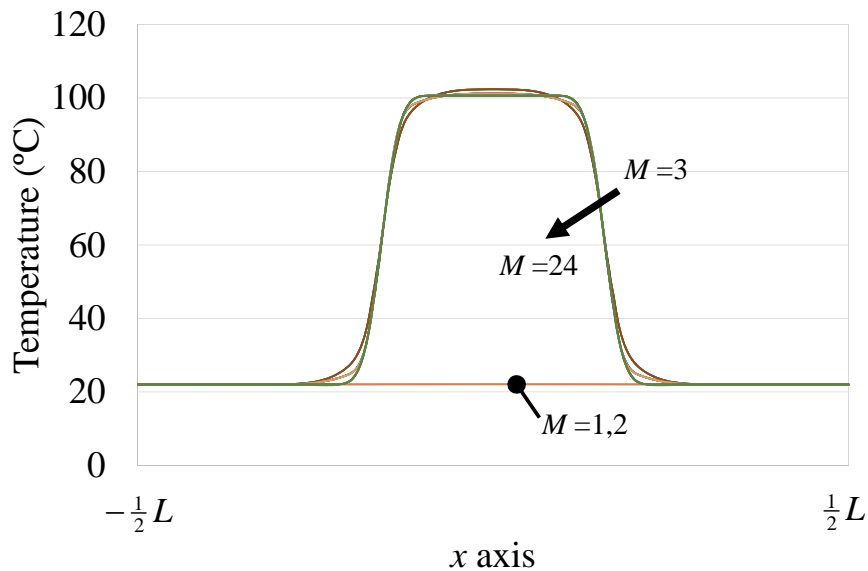


**Figure 8.1. Evolution of the temperature along the  $x$  axis for  $t=1.5$  seconds and  $y=0$ , from  $M=1$  to  $M=24$**

Note that, for  $M=1$  and  $M=2$ , the solution obtained is very far from the final one but, from  $M=3$  the evolution of the curve remains very close to the final solution.

As most of the approximations are very close one to each other, in order to show the improvement of the solution more precisely, an enlarged view of the curve of Figure 8.1, extracted from the zone where the maximum temperature is reached, is shown in Figure 8.2. Note that the solutions given by  $M=1$  and  $M=2$  are not included in this picture because they remain close to  $23\text{ }^{\circ}\text{C}$ .

After  $M=16$ , the solution is only slightly modified in each iteration, obtaining a very similar shape of the curve than for the complete solution, with  $M=24$ .

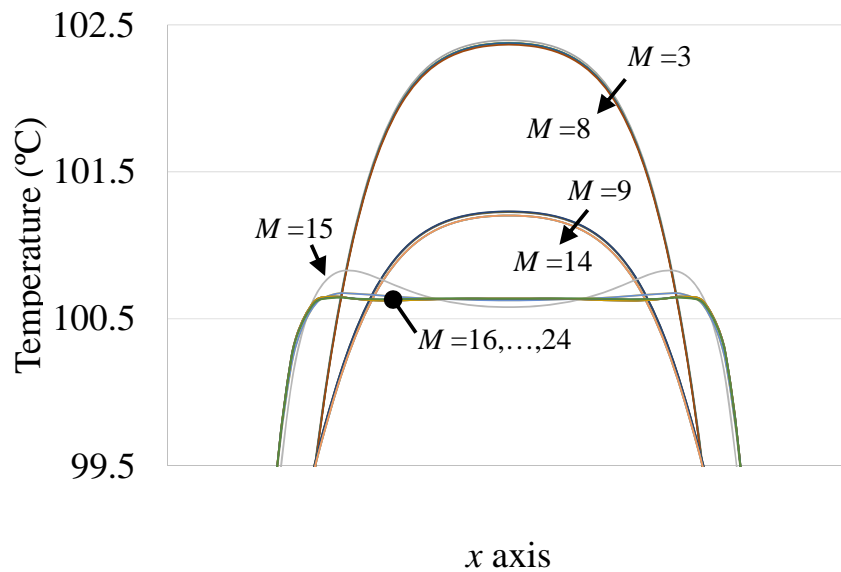


**Figure 8.2. Enlarged view of the evolution of the temperature along the  $x$  axis for  $t=1.5$  seconds and  $y=0$ , from  $M=3$  to  $M=24$**

The curve shown in Figure 8.3, which represents the evolution of the temperature along the  $y$  axis, has been obtained for a value of the time

$t = 1.5$  seconds and at the line of nodes located at the central section of the laminate ( $x = 0$ ).

As most of the approximations are very close one to each other, in order to show the improvement of the solution more precisely, an enlarged view of the curve of Figure 8.3, extracted from the zone where the maximum temperature is reached, is shown in Figure 8.4. The different resin and fibre layers can be appreciated in the solution, the resin layers reaching a higher temperature due to the heat generated inside them.

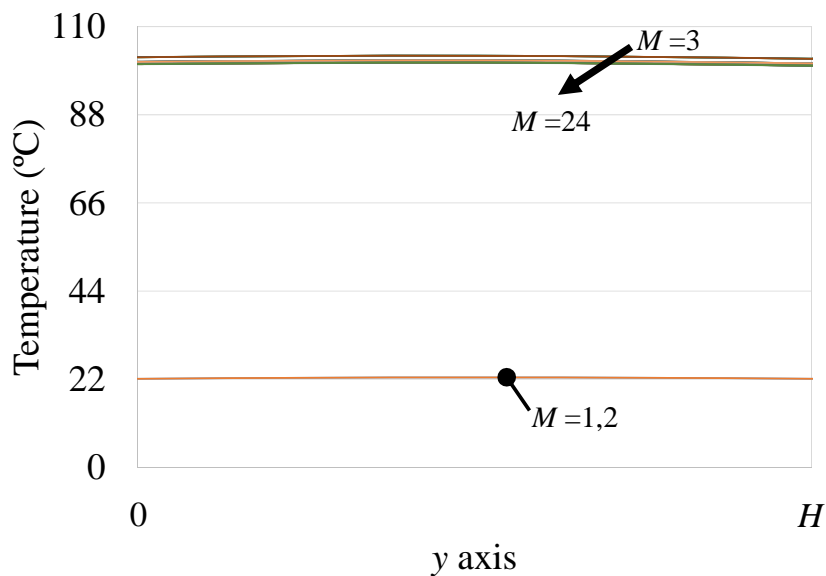


**Figure 8.3. Evolution of the temperature along the y axis for  $t=1.5$  seconds and  $x=0$ , from  $M=1$  to  $M=24$**

The curve shown in Figure 8.5, which represents the evolution of the temperature along the time axis, has been obtained at the line of nodes located at the central section and at the bottom of the laminate ( $x = 0, y = 0$ ).

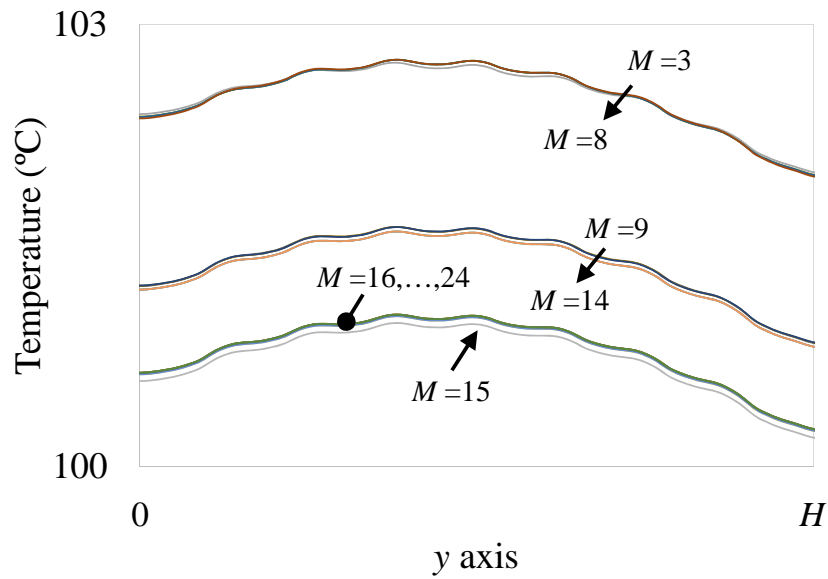


**Figure 8.4. Enlarged view of the evolution of the temperature along the y axis for  $t=1.5$  seconds and  $x=0$ , from  $M=3$  to  $M=24$**

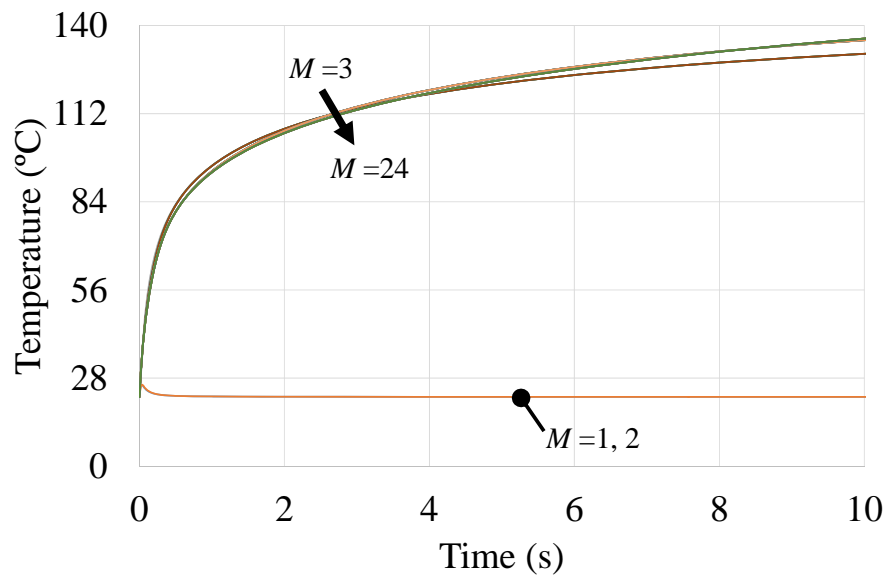


**Figure 8.5. Evolution of the temperature along the time axis for  $x=0$  and  $y=0$ , from  $M=1$  to  $M=24$**

As most of the approximations are very close one to each other, in order to show the improvement of the solution more precisely, an enlarged view of the curve of Figure 8.5, extracted from the zone where the maximum temperature is reached, is shown in Figure 8.6.

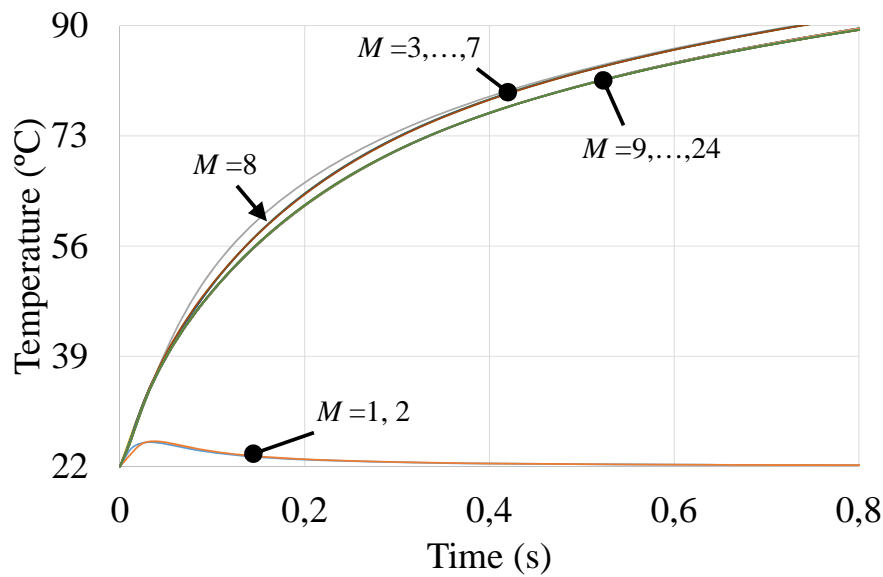


**Figure 8.6. Enlarged view of the evolution of the temperature along the time axis for  $x=0$  and  $y=0$ , from  $M=1$  to  $M=24$**

In order to check the evolution of the temperature across the thickness of the laminate, a 3D representation is shown in Figure 8.7.

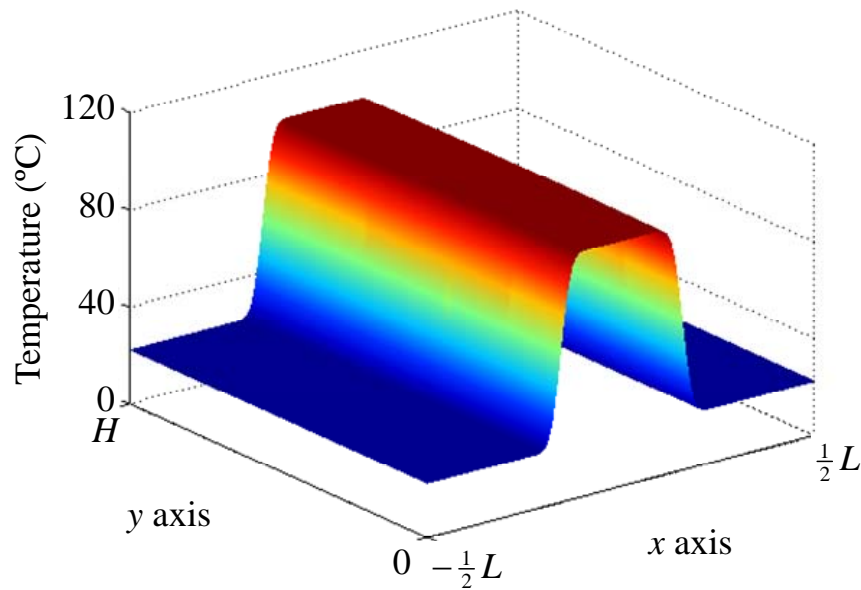


**Figure 8.7. 3D View of the temperature distribution inside the laminate during compaction process ( $t=1.5$  seconds)**

As can be appreciated, there is almost no variation in the  $y$  direction. Due to the high heat generated, the boundary condition that concerns the sonotrode has almost no influence in the results.

As could be expected, the maximum temperature is obtained at the centre of the sonotrode and it decreases when reaching the ends of the sonotrode, due to the heat conduction inside the laminate along the direction of the fibre. Far enough from the sonotrode, the temperature of the laminate is the same than at the beginning of the compaction process (note that, at this time, the information of the heating has not reached these zones of the laminate).

In order to study the evolution of the temperature along the process, a curve time/temperature is presented in Figure 8.8. The curve has been obtained from a node situated at the bottom layer, in the middle of the length of the sonotrode, i. e., at  $x = 0$  and  $y = 0$ . The process time computed is from  $t = 0$  seconds to  $t_{\max} = 10$  seconds.

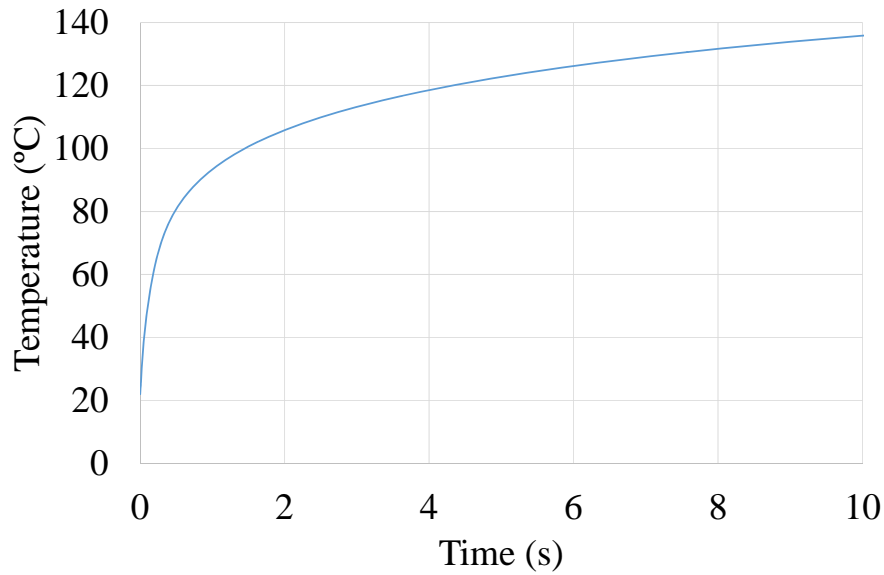


**Figure 8.8. Evolution of the temperature with time during the compaction process at  $(x=0, y=0)$**

As can be appreciated, there is a fast heating in an initial stage (at a time of the order of 0.5 seconds) and then a stabilization phase follows. This stabilization is due to the evolution of the viscosity with the temperature (it decreases very fast when temperature increases), making the value of the heat generated due to internal viscosity almost negligible when the temperature is close to 150 °C.

## 8.5 Model validation

The evolution of the temperature during the compaction process obtained with the transient solution will be compared with an experimental result. The experiment and the result obtained were presented in Chapter 2. In that case, the sonotrode was actuated over a 8-ply laminate during 10 seconds. The temperature was measured with a thermocouple, placed at the bottom of the laminate and just at the middle of the length of the sonotrode, i.e., at  $x = 0$  and  $y = 0$  in the model.

The comparison of PGD predictions with the experimental results is shown in Figure 8.9.

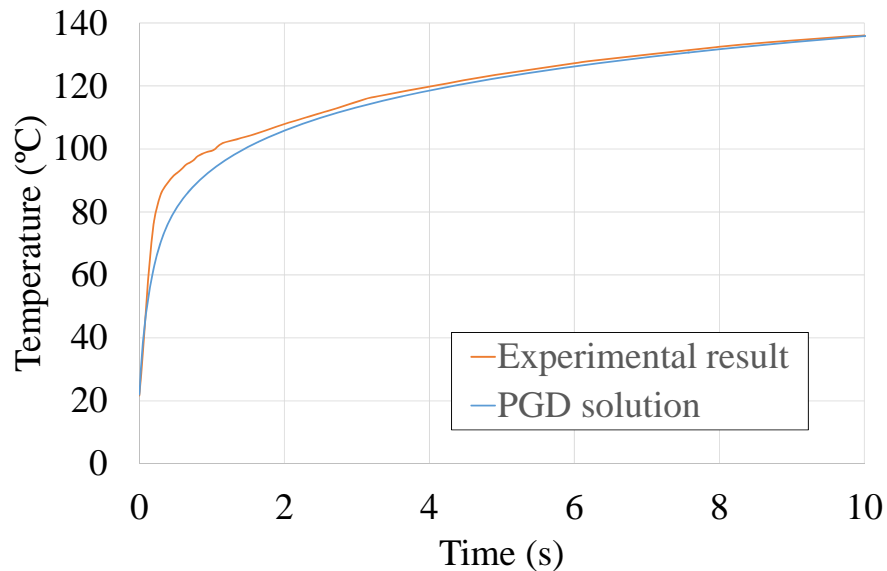


**Figure 8.9. Comparison of experimental and numerical temperature/time curve at the bottom of the laminate**

The validation of the thermal properties of the materials carried out in Chapter 4 and the experience achieved with the previous models presented in Chapters 6 and 7 has led to obtain an appropriate solution with the PGD. In this way, the agreement between the experimental and the numerical curves is very satisfactory. This agreement allows us to validate the thermomechanical model presented in Chapter 5.

The only discrepancies that can be found between the numerical and experimental results are at the zone between 80 and 100 °C, in which the tendency of the curves change. It can be motivated by the election of the evolution of the viscosity, a linear tendency having been chosen. In the real case, when the temperature is high enough, the curve change its tendency, presenting differences with the linear trend. In any case, as only one curve has been obtained experimentally, the light differences between the experimental and numerical

results should not be considered, as, surely, with more measurements the dispersion of the experimental results would absorb these discrepancies.

## 8.6 Conclusions

A new approach to study the heat generation and distribution during ultrasonic compaction process has been carried out. As remarked, this study is a very important task in order to optimize the process.

After remarking the complexity and the strong coupling between the variables of the problem and the difficulties of the previous approaches, a new solution strategy has been considered. The Proper Generalized Decomposition has been considered capable to avoid the numerical and computational problems presented.

The equations to solve the problem with the PGD have been presented. This equations solve the heat distribution but not the heat generation. To this end, an algorithm that couples the resolution of the heat generation and the heat distribution has been generated.

The compaction process has been studied from one way of operation: the compaction process when the sonotrode is still (treated as a transient problem), i.e., the sonotrode vibrates over the laminate but it is not moved along it. As a result, the temperature field of the composite plies has been obtained.

In this transient case, the evolution of the temperature inside the laminate from the initial conditions to a certain time of the compaction process has been depicted.

The model has been compared with experimental values, showing a good agreement with the predictions. This comparison validates the heat generation model developed in Chapter 5.

The numerical technique shown has presented an enormous reduction in the computing times, compared with the FEM, allowing also obtaining a very fine solution.

It has to be noticed that, in order to obtain the finest solution possible, the heat generation has been calculated taking into account all the oscillations of the sonotrode. This model has led to validate the heat generation model. Another possible approach could have been to study the heat generation during a cycle of the vibration (obtaining in this way the heat per time unit) and then, extending this heat along the process time (or splitting the process time in several sections in which this procedure were carried out). In this way, the cost in time would have been smaller than the resolution presented in this Chapter, but the accuracy of the solution would have also been smaller. A similar simplification to obtain the heat per time unit to estimate the heat generation will be used in Chapter 9, in the steady-state model.

## Bibliography

- [8.1] Chinesta, F., Leygue, A., Bordeu, F., Aguado, J.V., Cueto, E., Gonzalez, D., Alfaro, I., Ammar, A., Huerta, A.: *PGD-Based Computational Vademecum for Efficient Design, Optimization and Control*. Archives of Computational Methods in Engineering, 20:31–59 (2013).
- [8.2] Chinesta, F., Ammar, A., Cueto, E.: *Recent Advances and New Challenges in the Use of the Proper Generalized Decomposition for Solving Multidimensional Models*. Archives of Computational Methods in Engineering, Vol 17, Issue 4, 327-350 (2010).

- [8.3] Ammar, A., Mokdad, B., Chinesta, F., Keunings, R.: *A new family of solvers for some classes of multidimensional partial differential equations encountered in kinetic theory modeling of complex fluids*. J. Non-Newtonian Fluid Mech., 139, 153-176 (2006).
- [8.4] Ammar, A., Mokdad, B., Chinesta, F., Keunings, R.: *A new family of solvers for some classes of multidimensional partial differential equations encountered in kinetic theory modeling of complex fluids. Part II: transient simulation using space-time separated representations*. J. Non-Newtonian Fluid Mech., 144, 98-121 (2007).
- [8.5] Pruliere, E., Chinesta, F., Ammar, A.: *On the deterministic solution of multidimensional parametric models using the Proper Generalized Decomposition*. Mathematics and Computers in Simulation, Vol. 81, Issue 4, 791-810 (2010).
- [8.6] Chinesta, F., Leygue, A., Bognet, B., Ghnatios, Ch., Poulhaon, F., Bordeu, F., Barasinski, A., Poitou, A., Chatel, S., Maison-Le-Poec, S.: *First steps towards an advanced simulation of composites manufacturing by automated tape placement*. International Journal of Material Forming. In press.
- [8.7] Chinesta, F., Ammar, A., Leygue, A., Keunings, R.: *An overview of the proper generalized decomposition with applications in computational rheology*. Journal of Non-Newtonian Fluid Mechanics, 166, 578-592 (2011).

# *Chapter 9*

## *PGD steady-state model*

The validity of the heat generation model developed in Chapter 5 has been proved with the PGD resolution of Chapter 8. Furthermore, the PGD has demonstrated to be a valid resolution technique to solve the coupled problem of the heat generation and distribution. The PGD compared with the FEM solution allows also a better solution (in terms of geometry discretization) to be obtained in very few computation times.

In this Chapter, the PGD and the heat generation model will be used to solve the problem of the compaction of several composite plies when the sonotrode is

moving along the laminate. In this case, the problem will be considered steady-state, as will be shown in Section 9.1. The content of the sections is explained next.

First, several considerations about the heat generation and distributions models assumed will be presented.

In the second section, as done in Chapter 8, an incremental algorithm will be presented, posed to solve the coupling between the heat generation and distribution mechanisms. In this case, as a steady-state problem is considered, the algorithm is not time-dependent.

In section 9.3, the equations that govern the resolution of the thermal field with the PGD in this problem will be developed. The results obtained with the model, for a fixed value of the horizontal displacement velocity of the sonotrode are presented in section 9.4. Then, a parametric analysis of the variables concerning the ultrasonic compaction will be done in section 9.5.

Finally, the conclusions related to this model and the results presented in this Chapter will be discussed.

## **9.1 Heat generation and distribution modelling**

The equations that define the thermal problem will be presented in this section. As done in previous Chapters, the equations that solve the heat distribution and the heat generation will be presented separately.

The problem that will be studied in this case is the compaction of several uncured plies when the sonotrode is moved over the laminate, along the fibre direction, with a certain horizontal displacement velocity. During the displacement, the sonotrode also vibrates over the laminate at an ultrasonic frequency.

The objective in this case is to obtain the steady state temperature inside the laminate in a coordinate system attached to the sonotrode tip, which is assumed to move with a constant velocity. In this condition, each material point experiences the same thermal history during the process: it is progressively heated when approaching the ultrasonic compactor, it reaches its maximum when the sonotrode applies directly on it and it cools down when getting far from the heat source.

Therefore, as done in [9.1] for the tape placement process, instead of considering a problem where the domain is fixed and the boundary conditions are time dependent, we can explicitly introduce the sonotrode horizontal displacement velocity,  $\mathbf{v} = (v, 0)$ , in the heat transfer equation by adding a convection term.

In this case, the heat equation writes:

$$\mathbf{v}\nabla T - \nabla \cdot (\mathbf{K}\nabla T) = \mathbf{Q}^{visc} \quad (9.1)$$

where  $T$  is the temperature field,  $\mathbf{Q}^{visc}$  is the heat generated in the resin due to its internal viscosity when is submitted to ultrasonic vibrations and  $\mathbf{K}$  is the conductivity tensor.

The steady-state model will be defined in a plate domain, given by  $\Omega = \Omega_x \times \Omega_y$ , with  $\Omega_x = [-\frac{1}{2}L, \frac{1}{2}L]$  and  $\Omega_y = [0, H]$ .

The laminate is considered to be composed of  $P$  different orthotropic layers, each one characterized by a well defined conductivity tensor  $\mathbf{K}_j$ , assumed constant in the layer thickness. In this way, a characteristic function representing the position of each layer can be defined:

$$\chi_j(y) = \begin{cases} 1 & y_j \leq y \leq y_{j+1} \\ 0 & otherwise \end{cases} \quad j = 1, \dots, P \quad (9.2)$$

where  $y_j$  and  $y_{j+1}$  are the bottom and top values of  $y$  of the  $j^{\text{th}}$  layer, respectively.

The laminate conductivity can be written in the following in a separated form using (2):

$$\mathbf{K}(x, y) = \sum_{j=1}^P \mathbf{K}_j(x) \chi_j(y) \quad (9.3)$$

In this work,  $\mathbf{K}$  has been assumed constant in each layer, so it does not depend on the  $x$  coordinate. In the case of the other properties of the material,  $\rho$  and  $C_p$ , as done in Section 8.1, a similar separated form is applied.

The same idea can be applied to the heat generation, but using a function  $\gamma_j(y)$  equal to 1 in the resin layers and null in the fibre layers (in order to represent that the heat is only generated at the resin layers). The separated representation of the heat generated can be expressed as:

$$\mathbf{Q}^{visc}(x, y, t) = \sum_{j=1}^P \phi_j(x) \gamma_j(y) Q_j(t) \quad (9.4)$$

In this case,  $\phi_j(x)$  is a function that takes a value of 1 when  $x$  is located under the sonotrode and 0 when  $x$  is not located under the sonotrode.

Note that, in this case, in order to consider the problem as steady-state, the heat generation has to be made independent of the time. It has been done calculating the heat generated during a cycle of the ultrasonic vibration ( $t_c$  being the time needed to complete a cycle). This heat generated, considered as heat per time unit, has been extended to all the process, making the variable time to disappear from the formulation. In this situation  $\mathbf{Q}^{visc}(x, y, t)$  reduces to  $\mathbf{Q}^{visc}(x, y)$ .

The problem of the heat generation has been solved in Chapter 5. The equations that govern this generation are presented next, integrated in time. Note that the  $y'$  coordinate that appears in these equations is associated to each resin layer,  $-\frac{1}{2}h_j < y' < \frac{1}{2}h_j$ , with  $h_j$  being the thickness of layer  $j$ .

$$Q_P = \int_0^{t_c} \int_{-\frac{1}{2}h_P}^{\frac{1}{2}h_P} \int_{-\frac{1}{2}L_S}^{\frac{1}{2}L_S} Q_P^h(x, y', t) dx dy' dt + \int_0^{t_c} \int_{-\frac{1}{2}h_P}^{\frac{1}{2}h_P} \int_{-\frac{1}{2}L_S}^{\frac{1}{2}L_S} Q_P^v(x, y', t) dx dy' dt \quad (9.5)$$

$$Q_j = \int_0^{t_c} \int_{-\frac{1}{2}h_j}^{\frac{1}{2}h_j} \int_{-\frac{1}{2}L_S}^{\frac{1}{2}L_S} Q_j^v(x, y', t) dx dy' dt \quad j = 1, \dots, P-1$$

where:

$$Q_P^h(x, y', t) = \eta_P(t) \left( \frac{w_{sh}(t)}{h_P} \right)^2 \quad (9.6)$$

$$Q_j^v(x, y', t) = \frac{144\eta_j(t)}{(h_j)^6} \left[ v_j\left(-\frac{1}{2}h_j, t\right) - v_j\left(\frac{1}{2}h_j, t\right) \right]^2 y'^2 x^2 \quad j = 1, \dots, P-1 \quad (9.7)$$

$Q_P^h(x, y', t)$  being the heat generated due to the horizontal movement of the sonotrode, only generated inside the top layer  $P$ ,  $Q_j^v(x, y', t)$  the heat generated due to the vertical movement of the sonotrode,  $\eta_j$  the viscosity of the  $j$ th-layer,  $v_j$  the vertical velocity of the resin layer at the extremes of the  $j^{\text{th}}$ -layer,  $h_j$  the thickness of the  $j^{\text{th}}$ -layer and  $w_{sh}$  the horizontal component of the velocity of the sonotrode.

## 9.2 Algorithm for solving the heat generation-distribution problem

This problem is going to be solved in two parts, iteratively, searching the convergence of the value of the heat generated.

The first part of the heat equation, corresponding to the heat distribution, i. e., left term of equation (9.1), will be solved with the PGD, assuming the values of

the viscous heating to be known. The problem is solved for every spatial node in the laminate. The equations used to solve this part of the problem will be described in section 8.3 of this Chapter.

The second part of the equation, corresponding to the heat generation, i. e., the right member of equation (9.1), will be solved using the equations (9.5), (9.6), (9.7) and related, presented in Chapter 5, using the temperatures calculated with the PGD. As mentioned before, the heat generation phase only takes place in the resin layers in the zone located under the sonotrode.

In order to obtain the solution to this problem, using the procedures described before, an algorithm is presented next:

Step 1: At the beginning of the algorithm, the horizontal displacement velocity of the sonotrode is fixed.

Step 2: The initial temperature at each spatial node is supposed known and equal to the room temperature.

Step 3: With the temperature field assumed in step 2, the viscous heating induced by the ultrasonic vibration is calculated at every resin layer using the procedure described in Chapter 5.

Step 4: The viscous heating matrix calculated in the previous step is used in the resolution of the heat distribution problem by solving equation (9.1) with the PGD. In this way, the value of the temperature at each spatial node is obtained in this step.

Step 5: The heat generation in each resin layer is calculated again using the generation equations of Chapter 5. The temperatures used in this step are a mean value of the temperatures of the nodes under the sonotrode of each resin layer, obtained in step 4.

Step 6: The updated heat generation matrix is compared with the one obtained in the previous iteration and, if the difference is smaller than a certain tolerance, the algorithm stops. If not, the updated heat generation matrix is used to solve the thermal problem again with the PGD (step 4).

The algorithm continues until reaching convergence, iterating between steps 4, 5 and 6.

Once finished, the algorithm returns the temperature field inside the laminate, at every node, during the compaction process.

### 9.3 PGD formulation of the heat distribution in laminates for a transient problem

The construction of the Proper Generalized Decomposition of the steady-state heat transfer model is illustrated in what follows. The thermal equation that defines the problem was presented in Equation (9.1).

Assuming that the coordinate system is oriented with the principal directions of  $\mathbf{K}$ , this tensor becomes diagonal:

$$\mathbf{K} = \begin{pmatrix} k_x & 0 \\ 0 & k_y \end{pmatrix} \quad (9.8)$$

where  $k_x$  and  $k_y$  are its principal thermal conductivities.

In this coordinate system, Equation (9.1) writes:

$$v \frac{\partial T}{\partial x} - k_x \frac{\partial^2 T}{\partial x^2} - k_y \frac{\partial^2 T}{\partial y^2} - \mathbf{Q}^{visc} = 0 \quad (9.9)$$

and the heat flux will be prescribed on the whole boundary  $\Phi = \partial(\Omega_x \times \Omega_y)$ ,  $\Phi = \Phi_1 \cup \Phi_2 \cup \Phi_3 \cup \Phi_4$ , the boundaries being  $\Phi_1 = (x = -\frac{1}{2}L, y \in \Omega_y)$ ,  $\Phi_2 = (x \in \Omega_x, y = 0)$ ,  $\Phi_3 = (x = \frac{1}{2}L, y \in \Omega_y)$ ,  $\Phi_4 = (x \in \Omega_x, y = H)$ . The boundary conditions of the problem are: isolation at  $\Phi_1$ ,  $\Phi_2$  and  $\Phi_3$  and conduction with the sonotrode/convection with the air (depending on the value of the  $x$  coordinate) at  $\Phi_4$ . These conditions can be expressed as:

$$\begin{aligned} \left. \frac{\partial T}{\partial x} \right|_{x,y \in \Phi_1} &= 0 \\ \left. \frac{\partial T}{\partial y} \right|_{x,y \in \Phi_2} &= 0 \\ \left. \frac{\partial T}{\partial x} \right|_{x,y \in \Phi_3} &= 0 \\ -k_y \left. \frac{\partial T}{\partial y} \right|_{x,y \in \Phi_4} &= \begin{cases} h \cdot (T(x, y = H) - T_{amb}) & x \in \Phi_4 - \Phi_4^s \\ h_s \cdot (T(x, y = H) - T_{amb}) & x \in \Phi_4^s \end{cases} \end{aligned} \quad (9.10)$$

where  $\Phi_4^s$  is the area of  $\Phi_4$  located under the sonotrode,  $h$  is the convection coefficient and  $h_s$  is a coefficient that determines the heat transfer with the sonotrode (this coefficient depends on the conductivity and the geometry of the sonotrode and has been calibrated experimentally).

The weighted residual form of equation (9.9) writes:

$$\int_{\Omega} T^* \left( v \frac{\partial T}{\partial x} - k_x \frac{\partial^2 T}{\partial x^2} - k_y \frac{\partial^2 T}{\partial y^2} - \mathbf{Q}^{visc} \right) d\Omega = 0 \quad (9.11)$$

with the test function  $T^*$  being defined in an appropriate functional space.

To introduce the boundary conditions into the formulation, the equation will be solved integrating by parts the term that involves second order derivatives. Note that in all boundaries the integral is equal to zero, except in the upper boundary. In this zone conduction exists with the sonotrode, in  $\Phi_4^s$ , and convection exists with the air in the zones that are not located under the sonotrode, in  $\Phi_4 - \Phi_4^s$ .

$$\begin{aligned}
& \int_{\Omega} T^* v \frac{\partial T}{\partial x} d\Omega + \int_{\Phi_4 - \Phi_4^s} T^* h (T(x, y = H) - T_{amb}) dx dy + \\
& + \int_{\Phi_4^s} T^* h_s (T(x, y = H) - T_{amb}) dx dy + \int_{\Omega} k_x \frac{\partial T^*}{\partial x} \frac{\partial T}{\partial x} d\Omega + \quad (9.12) \\
& + \int_{\Omega} k_y \frac{\partial T^*}{\partial y} \frac{\partial T}{\partial y} d\Omega - \int_{\Omega} T^* \mathbf{Q}_j^{visc} d\Omega = 0
\end{aligned}$$

The solution  $T(x, y)$  is searched under the separated form:

$$T(x, y) \approx \sum_{l=1}^{l=M} X_l(x) \cdot Y_l(y) \quad (9.13)$$

where  $X_l(x)$  and  $Y_l(y)$  are enrichment functions to be determined iteratively during the solution of the problem.

In what follows, the construction of one of such enrichment functions is illustrated. For this purpose, we assume that, at iteration  $m < M$ , the solution is already known:

$$T^m(x, y) \approx \sum_{l=1}^{l=m} X_l(x) \cdot Y_l(y) \quad (9.14)$$

and that at the present iteration we look for the solution enrichment:

$$T^{m+1}(x, y) = T^m(x, y) + R(x) \cdot W(y) \quad (9.15)$$

The test function involved in the weak form of the thermal equation, (9.12), is searched under the form:

$$T^*(x, y) = R^*(x) \cdot W(y) + R(x) \cdot W^*(y) \quad (9.16)$$

As the enrichment process is non-linear, the functions  $R(x)$  and  $W(y)$  are proposed to be searched by applying an alternating direction fixed point algorithm:

Step 1: assuming  $W(y)$  to be known,  $R(x)$  is computed.

Step 2:  $W(y)$  is calculated with the obtained  $R(x)$ .

The process continues until reaching convergence.

The converged solutions allow the next term in the finite sums decomposition to be defined:  $R(x) \rightarrow X_{n+1}(x)$  and  $W(y) \rightarrow Y_{i+1}(y)$ .

In the following subsections, the operations implied on each one of the just referred steps are illustrated.

### 9.3.1 Computing $R(x)$ from $W(y)$

When  $W(y)$  is known, the test function (9.16) reduces to:

$$T^*(x, y) = R^*(x) \cdot W(y) \quad (9.17)$$

and the weak form (9.12) reduces to:

$$\begin{aligned}
& \int_{\Omega} R^* W \nu \frac{dR}{dx} W d\Omega + \int_{\Omega_x} R^* W(H) h (RW(H) - T_{amb}) dx + \\
& + \int_{\Omega_x} R^* W(H) h_s (RW(H) - T_{amb}) dx + \int_{\Omega} k_x \frac{dR^*}{dx} W \frac{dR}{dx} W d\Omega + \\
& + \int_{\Omega} k_y R^* \frac{dW}{dy} R \frac{dW}{dy} d\Omega = - \int_{\Omega} R^* W \nu \zeta^m d\Omega - \int_{\Omega} \left( \frac{dR^*}{dx} W \quad R^* \frac{dW}{dy} \right) \xi^m d\Omega - \\
& - \int_{\Phi_4 - \Phi_4^i} R^* W(H) h \psi^m dx - \int_{\Phi_4^i} R^* W(H) h_s \psi^m dx
\end{aligned} \tag{9.18}$$

where  $\zeta^m$  and  $\xi^m$  are the residuals at enrichment step  $m$  :

$$\begin{aligned}
\zeta^m &= \sum_{l=1}^{l=m} \frac{dX_l(x)}{dx} Y_l(y) - \mathbf{Q}^{visc} \\
\xi^m &= \mathbf{K} \sum_{l=1}^{l=m} \begin{pmatrix} \frac{dX_l(x)}{dx} Y_l(y) \\ X_l(x) \frac{dY_l(y)}{dy} \end{pmatrix} \\
\psi^m &= \sum_{l=1}^{l=n} X_l(x) Y_l(H)
\end{aligned} \tag{9.19}$$

As all the functions involving coordinate  $y$  are known, they could be integrated in  $\Omega_y = [0, H]$ . These integrations are presented next. Note that, in order to simplify the number of equations, (9.20) includes integrals in  $R$  that cannot be integrated at this moment, but will be used in subsequent computations (section 3.1.2).

$$\begin{aligned}
w_1 &= \int_{\Omega_y} W^2 dy & r_1 &= \int_{\Omega_x} R^2 dx \\
w_2^l &= \int_{\Omega_y} W Y_l dy & r_2^l &= \int_{\Omega_x} R \cdot X_l dx \\
w_3 &= \int_{\Omega_y} W dy & r_3 &= \int_{\Omega_x} R dx \\
w_4 &= \int_{\Omega_y} W \frac{dW}{dy} dy & r_4 &= \int_{\Omega_x} R \frac{dR}{dx} dx
\end{aligned} \tag{9.20}$$

Then, we can define:

$$\mathbf{K}_x = \begin{pmatrix} \int_{\Omega_y} k_x W^2 dy & 0 \\ 0 & \int_{\Omega_y} k_y \left( \frac{dW}{dy} \right)^2 dy \end{pmatrix} \tag{9.21}$$

and

$$\begin{aligned}
\zeta_x^m &= \sum_{l=1}^{l=n} \left( \int_{\Omega_y} W v Y_l dy \frac{dX_l(x)}{dx} \right) \\
\zeta_x^m &= \sum_{l=1}^{l=n} \left( \begin{pmatrix} \int_{\Omega_y} k_x W Y_l dy & 0 \\ 0 & \int_{\Omega_y} k_y \frac{dW}{dy} \frac{dY_l}{dy} dy \end{pmatrix} \begin{pmatrix} \frac{dX_l(x)}{dx} \\ X_l(x) \end{pmatrix} \right) \\
\psi_x^m &= \sum_{l=1}^{l=n} W(H) Y_l(H) (X_l(x))
\end{aligned} \tag{9.22}$$

Then, Eq. (9.18) reduces to:

$$\begin{aligned}
& \int_{\Omega_x} R^* w_1 v \frac{dR}{dx} dx + \int_{\Omega_x - \Omega_s} R^* (W(H))^2 h R dx + \int_{\Omega_s} R^* (W(H))^2 h_s R dx + \\
& + \int_{\Omega_x - \Omega_s} R^* W(H) h (-T_{amb}) dx + \int_{\Omega_s} R^* W(H) h_s (-T_{amb}) dx + \\
& + \int_{\Omega_x} \left( \frac{dR^*}{dx} \quad R^* \right) \mathbf{K}_x \left( \frac{dR}{dx} \quad R \right) dx = - \int_{\Omega_x} R^* \zeta_x^m dx - \int_{\Omega_x} R^* w_3 \mathbf{Q}^{visc} dx + \\
& + \int_{\Omega_x} \left( \frac{dR^*}{dx} \quad R^* \right) \zeta_x^m dx - \int_{\Omega_x - \Omega_s} R^* h \psi_x^m dx - \int_{\Omega_s} R^* h_s \psi_x^m dx
\end{aligned} \tag{9.23}$$

that defines an elliptic steady-state boundary value problem (BVP) for the unknown function  $R$  that can be solved by using a FEM model with a 1D smooth mesh.

### 9.3.2 Computing $W(y)$ from $R(x)$

When  $R(x)$  is known, the test function (9.16) reduces to:

$$T^*(x, y) = R(x) \cdot W^*(y) \tag{9.24}$$

and the weak form (9.12) reduces to:

$$\begin{aligned}
& \int_{\Omega} RW^* v \frac{dR}{dx} W d\Omega + \int_{\Omega_x} RW^* (H) h (RW(H) - T_{amb}) dx + \\
& + \int_{\Omega_x} RW^* (H) h_s (RW(H) - T_{amb}) dx + \int_{\Omega} k_x \frac{dR}{dx} W^* \frac{dR}{dx} W d\Omega + \\
& + \int_{\Omega} k_y R \frac{dW^*}{dy} R \frac{dW}{dy} d\Omega = - \int_{\Omega} RW^* v \zeta^n d\Omega - \int_{\Omega} \left( \frac{dR}{dx} W^* \quad R \frac{dW^*}{dy} \right) \xi^n d\Omega - \\
& - \int_{\Phi_4 - \Phi_4^i} RW^* (H) h \psi^n dx - \int_{\Phi_4^i} RW^* (H) h_s \psi^n dx
\end{aligned} \tag{9.25}$$

Now, as all the functions involving the coordinate  $x$  are known, they could be integrated in  $\Omega_x = [-\frac{1}{2}L, \frac{1}{2}L]$ . Thus, using the previous notation, we can define:

$$\mathbf{K}_y = \begin{pmatrix} \int_{\Omega_x} k_x \left( \frac{dR}{dx} \right)^2 dx & 0 \\ 0 & \int_{\Omega_x} k_y R^2 dx \end{pmatrix} \tag{9.26}$$

$$\begin{aligned}
\zeta_y^m &= \sum_{l=1}^{l=m} \left( \int_{\Omega_x} R v \frac{dX_l}{dx} dx Y_l(y) \right) \\
\xi_y^m &= \sum_{l=1}^{l=m} \left( \begin{pmatrix} \int_{\Omega_x} k_x \frac{dR}{dx} \frac{dX_l}{dx} dx & 0 \\ 0 & \int_{\Omega_x} k_y R X_l dx \end{pmatrix} \begin{pmatrix} Y_l(y) \\ \frac{dY_l(y)}{dy} \end{pmatrix} \right)
\end{aligned} \tag{9.27}$$

$$\psi_y^m = h \sum_{l=1}^{l=m} \int_{\Omega_x} R X_l(x) dx (Y_l(H))$$

$$\psi_{ys}^m = h_s \sum_{l=1}^{l=m} \int_{\Omega_s} R X_l(x) dx (Y_l(H))$$

Then, Eq. (9.25) reduces to:

$$\begin{aligned}
& \int_{\Omega_y} W^* r_4 v W dy + W^*(H) r_1|_{\Omega_x-\Omega_s} h W(H) + W^*(H) r_1|_{\Omega_s} h_s W(H) + \\
& + W^*(H) r_3|_{\Omega_x-\Omega_s} h(-T_{amb}) + W^*(H) r_3|_{\Omega_s} h_s(-T_{amb}) + \\
& + \int_{\Omega_y} \left( W^* \frac{dW^*}{dy} \right) \mathbf{K}_y \left( \frac{W}{dy} \right) dy = - \int_{\Omega_y} W^* \zeta_y^m dy - \int_{\Omega_y} W^* w_3 \mathbf{Q}^{visc} dy - \\
& - \int_{\Omega_y} \left( W^* \frac{dW^*}{dy} \right) \xi_y^m dy - W^*(H) (\psi_y^m + \psi_{ys}^m)
\end{aligned} \tag{9.28}$$

that defines a one-dimensional BVP that can be solved with FEM using a 1D smooth mesh.

## 9.4 Results

The problem has been solved for a laminate consisting on 8 uncured plies and for a value of the horizontal velocity of the sonotrode of 0.0075 m/s.

The problem has been solved with the PGD using the formulation presented in Section 9.3, where the applied boundary conditions were also specified.

The mesh used consists on 10000 nodes for the length of the laminate, along the  $x$  axis (where  $L = 3000$  mm ) and 321 nodes for the thickness of the laminate, along the  $y$  axis (where  $H = 1.04$  mm). The length of the sonotrode is, again,  $L_s = 20$  mm. Finally, the distance between the centre of the laminate and the centre of the sonotrode is  $L_c = 1480$  mm (at 20 mm of the right boundary). The value of  $L$  has been selected to leave the laminate to cool down completely. In order to show

the solution properly, it has been depicted from a reference distance, at  $x_{ref} = 1180$  mm, leaving a study zone of 320 mm.

The convergence of the solution of the problem has been achieved with 11 sums of products  $X_l(x)Y_l(y)$ . The evolution of the functions  $X_l(x)$  and  $Y_l(y)$  with their respective coordinates can be seen in Appendix II. In order to check how the solution is approximated when adding several products of functions  $X_l(x)Y_l(y)$ , the evolutions of the temperature along the  $x$  axis and along the  $y$  axis are shown next, respectively.

The curve shown in Figure 9.1 represents the evolution of the temperature along the  $x$  axis. The line of nodes for which the curve is obtained is located at the bottom of the laminate. The curves represent the solution given by (9.13) from  $M=1$  to  $M=11$ . In this case, the sonotrode is located at the position marked as sonotrode in the picture (it is supposed to be moving along the positive direction of the  $x$  axis, that implies an opposite velocity of the laminate). The space between the vertical dotted lines indicates the width of the sonotrode.

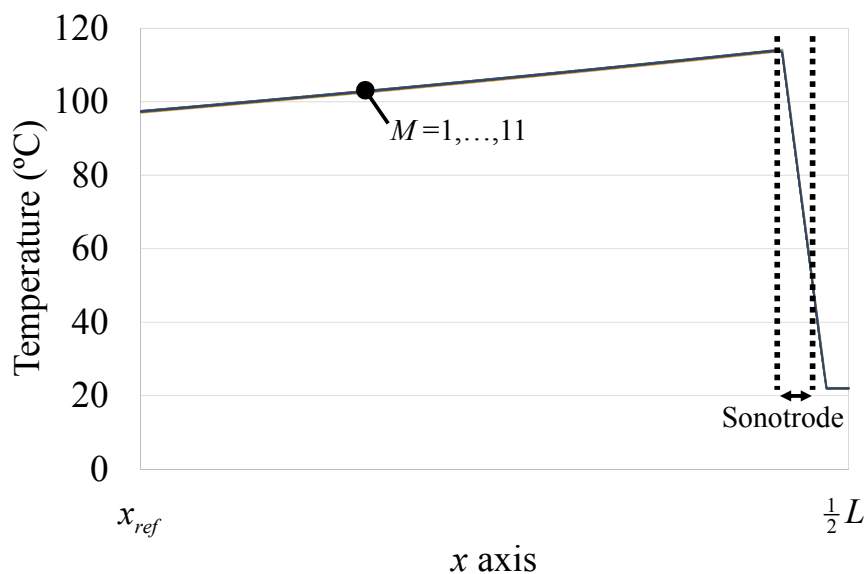


**Figure 9.1. Evolution of the temperature along the  $x$  axis for  $y=0$ , from  $M=1$  to  $M=11$**

As all the approximations are very close, in order to show the evolution of the solution more properly, an enlarged view of the curve of Figure 9.1, extracted from the zone where the maximum temperature is obtained, is shown in Figure 9.2.

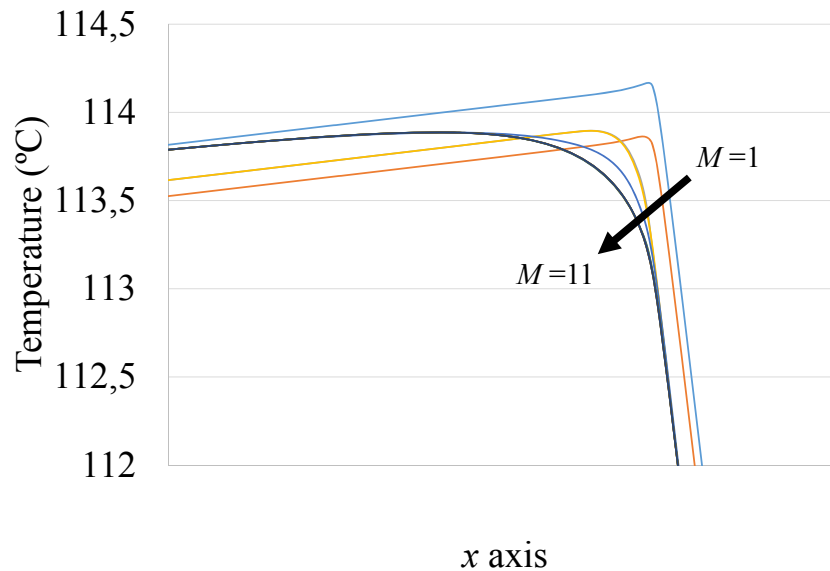


**Figure 9.2. Extended view of the evolution of the temperature along the  $x$  axis for  $y=0$ , from  $M=1$  to  $M=11$**

Four zones can be appreciated in the evolution shown in Figure 9.1, studying the curves from  $x = x_{ref}$  to  $x = \frac{1}{2}L$ : a first zone, where the sonotrode has passed and the laminate has been heated and is cooling down due to the convection with the air and the conduction inside itself. A second zone, just below the sonotrode, where the laminate is heating up due to the heat generation produced by the ultrasonic vibration. After that, a third zone, where the laminate is not located under the sonotrode but is already affected by the temperature increment of the adjacent zone. Finally, at the top right of the picture a fourth zone can be observed, where the laminate is at room temperature and has not noticed the arrival of the sonotrode yet.

The curve shown in Figure 9.3 represents the evolution of the temperature along the  $y$  axis. The line of nodes for which the curve is obtained is located at the

left of the sonotrode ( $x = L_c - \frac{1}{2}L_s$ ). The curves represent the solution given by (37) from  $M=1$  to  $M=11$ .

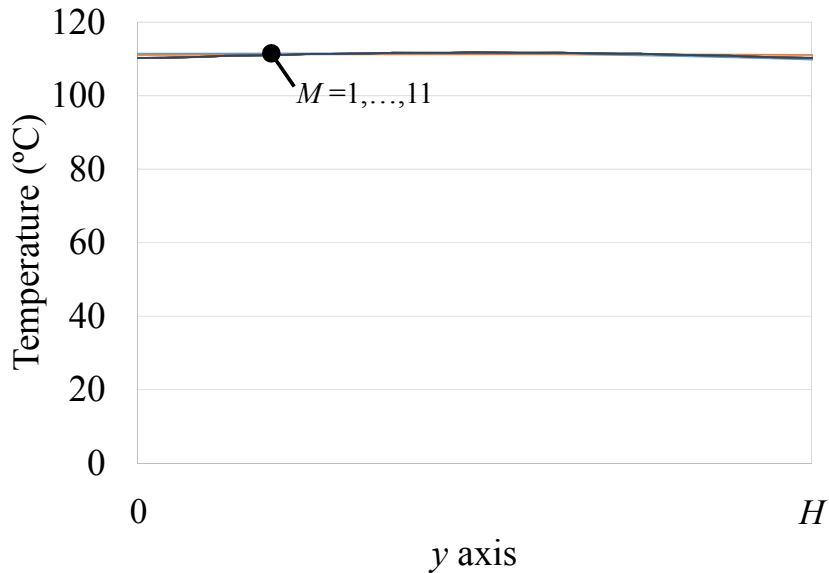


**Figure 9.3. Evolution of the temperature along the  $y$  axis at  $x = L_c - \frac{1}{2}L_s$  from  $M=1$  to  $M=11$**

As all the approximations are very close, in order to show the evolution of the solution more properly, an enlarged view of the curve of Figure 9.3 is shown in Figure 9.4.

The evolution of the temperature along the thickness direction can be appreciated in Figure 9.5, where a graphic  $T(x, y)$  has been depicted. Note that it is not at a real scale ( $L \gg H$ ), in order to obtain a better view of the result.

As can be seen, there is almost no variation of the temperature with the  $y$  direction at the zone located under the sonotrode. At the cooling zone, the temperature is decreased faster at the top zone of the laminate, due to the convection with the air that takes place in this area.

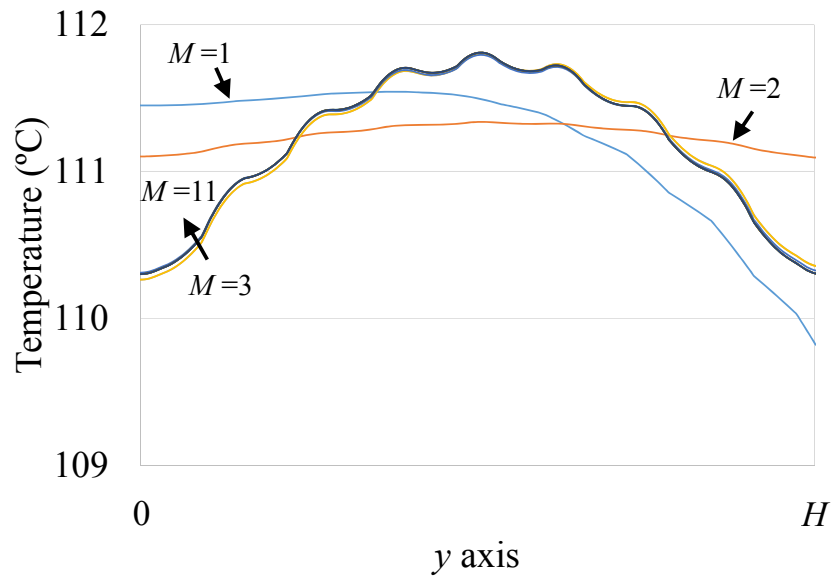


**Figure 9.4.** Enlarged view of the evolution of the temperature along the  $y$  axis at  $x = L_c - \frac{1}{2}L_s$  from  $M=1$  to  $M=11$

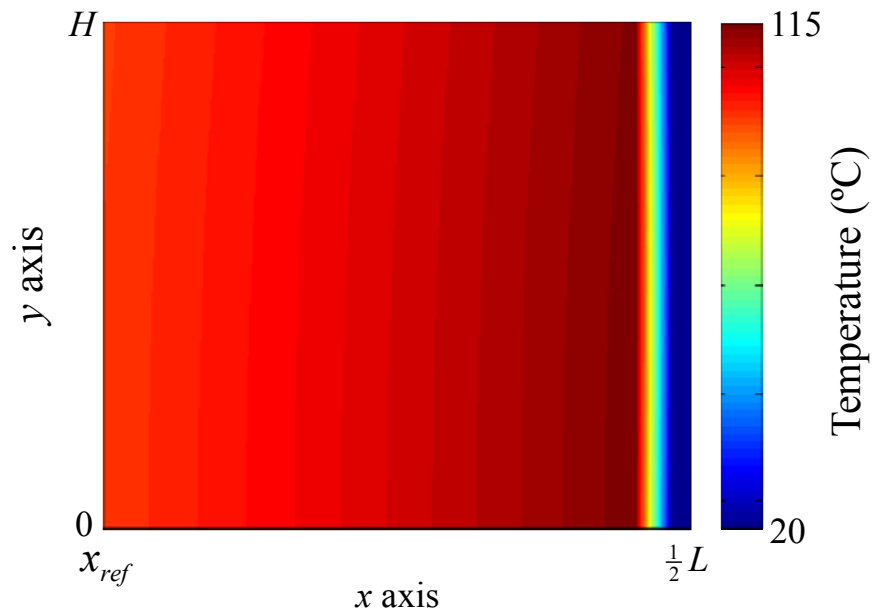


**Figure 9.5.** Temperature field inside the laminate during a pass of the sonotrode

## 9.5 Parametric study of the influence of the compaction parameters

The effect of several parameters that can influence the compaction procedure will be studied next. The parameters chosen are the horizontal displacement velocity of the sonotrode, the amplitude of the ultrasounds and the frequency of the ultrasounds. Another parameter that has been studied is the angle of the sonotrode. Note that, in this case, the variation of the parameter should imply the modification of the geometry of the sonotrode tip.

In order to see the influence of each parameter in the solution of the process clearly, during the study of a parameter, the others will remain constant.

### 9.5.1 Horizontal displacement velocity of the sonotrode

In order to study the influence of the horizontal velocity of the sonotrode, equation (36) has been solved for the following values:  $v = 0.0025$  m/s,  $v = 0.005$  m/s,  $v = 0.0075$  m/s and  $v = 0.01$  m/s.

Once the problem has been solved for each velocity, the evolution of the temperature inside the laminate has been determined in each case. Figure 9.6 shows the evolution of the temperature inside the laminate (at the bottom resin layer) during a pass of the sonotrode for the abovementioned horizontal speeds.

As could be expected, the faster the velocity of the sonotrode, the lower the maximum temperature reached inside the laminate and also the lower the slope of the heating and cooling curves. It can be seen that an increment of the 33.33% in the horizontal velocity produces a decrement of the maximum temperature of 4.6%. On the contrary, a decrement of 33.33% of the horizontal speed produces an increment of the maximum temperature of 3.9%. When increasing the difference, a decrement

in the horizontal velocity of 66.66% produces an increment of the maximum temperature of 18.4%. The non-linear variation of the maximum temperature with the horizontal velocity is explained in the non-linear behavior of the temperature along the time, as can be seen, for example, in Figure 8.5 in Chapter 8.

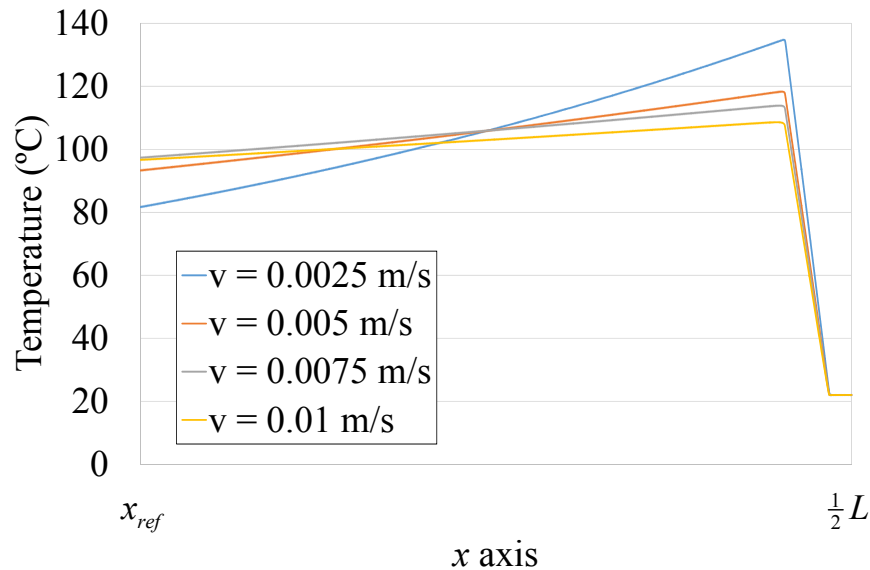


**Figure 9.6. Evolution of the temperature inside the laminate along the  $x$  axis at  $y=0$  during a pass of the sonotrode for several velocities**

### 9.5.2 Amplitude of the ultrasonic vibration

In order to study the influence of the amplitude of the ultrasonic vibration applied to the laminate, the problem has been solved for the original amplitude (0.024 mm) and incrementing the amplitude in a 30% (0.0312 mm) and decreasing the amplitude in a 30% (0.0168 mm).

The evolution of the temperature at the bottom of the laminate for each value of the amplitude is shown in Figure 9.7.

It can be seen that, when increasing the amplitude of the ultrasonic vibration, the temperature raised in the laminate is increased. Anyway, an increment of the 30% in the frequency only increments the temperature (the maximum difference) in a 3.31%. The same difference is obtained when decreasing the amplitude a 30%.

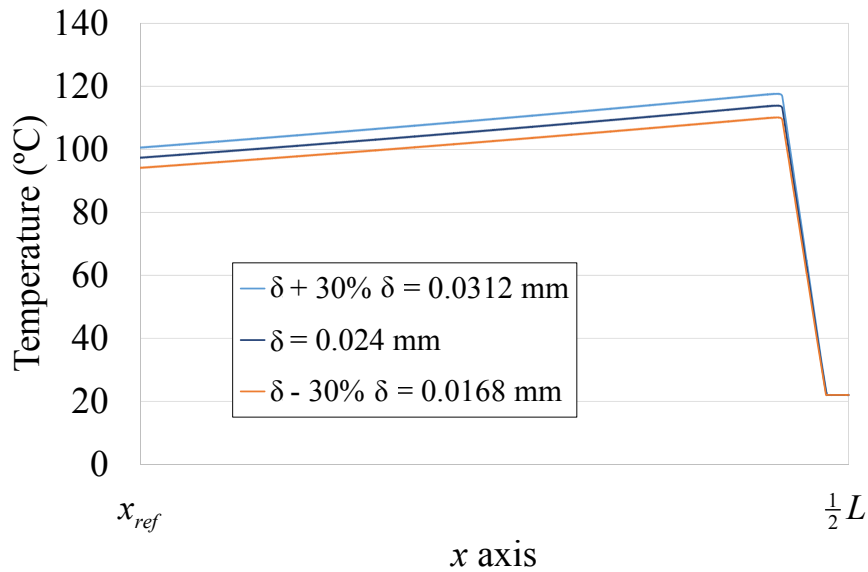


**Figure 9.7. Evolution of the temperature inside the laminate along the  $x$  axis at  $y=0$  during a pass of the sonotrode for several amplitudes of the vibration**

### 9.5.3 Frequency of the ultrasonic vibration

As done in Section 9.5.2, in order to study the influence of the frequency of the ultrasonic vibration applied to the laminate, the problem has been solved for the original frequency (20 KHz) and incrementing the frequency in a 30% (26 KHz) and decreasing the frequency in a 30% (14 KHz).

The evolution of the temperature at the bottom of the laminate for each value of the frequency is shown in Figure 9.8.

It can be seen that, when increasing the frequency of the ultrasonic vibration, the temperature raised in the laminate is increased. In this case, an increment of the 30% in the frequency increments the temperature (the maximum difference) in a 3.4% and, when decreasing the frequency in a 30%, the maximum difference obtained is a 4.6%.

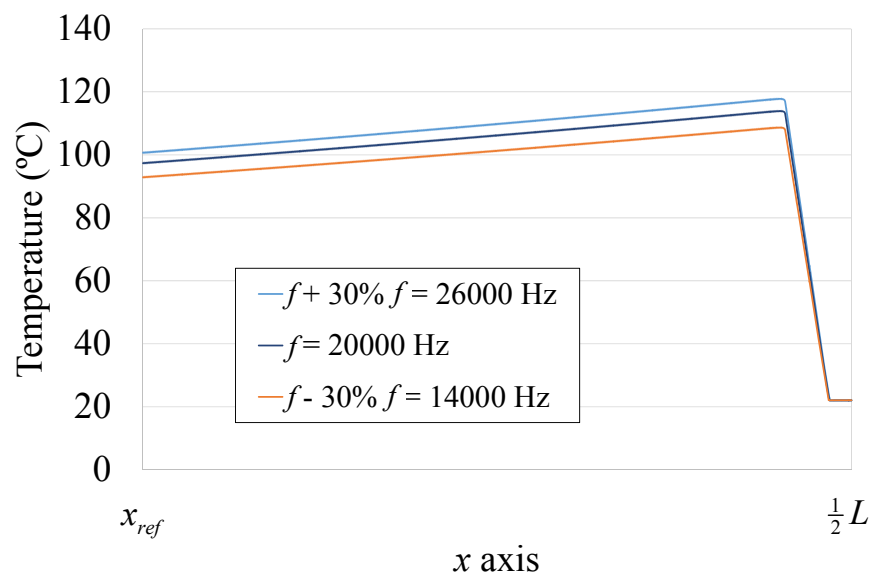


**Figure 9.8.** Evolution of the temperature inside the laminate along the  $x$  axis at  $y=0$  during a pass of the sonotrode for several frequencies of the vibration

### 9.5.4 Angle of the sonotrode

The way of measuring the angle of the sonotrode with respect to the laminate is shown in Figure 9.9. The previous studies have been carried out for an angle of the sonotrode of value  $\varphi = 45^\circ$ .

In order to study the influence of the angle of the sonotrode, the problem has been solved for three angles:  $45^\circ$  (the one used in this work),  $30^\circ$  and  $60^\circ$ .

The evolution of the temperature at the bottom of the laminate for each value of the angle of the sonotrode is shown in Figure 9.10.

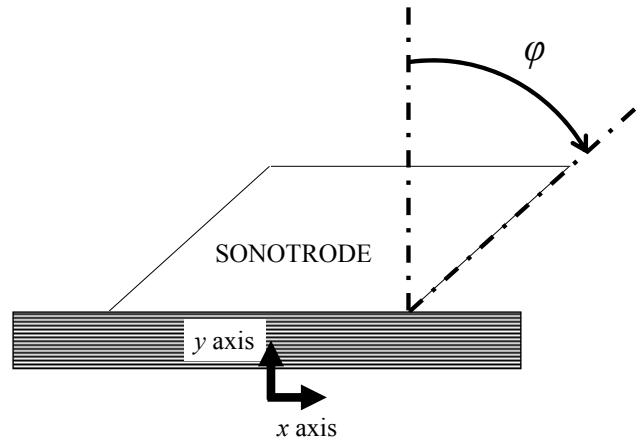


**Figure 9.9. Angle of the sonotrode**

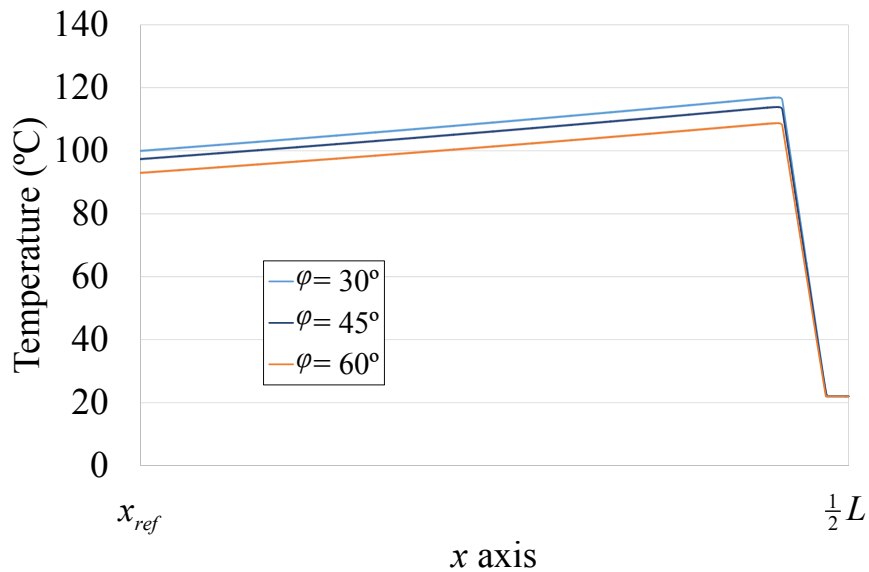


**Figure 9.10. Evolution of the temperature inside the laminate along the x axis at  $y=0$  for several angles of the sonotrode**

It can be seen that, when decreasing the angle of the sonotrode, the temperature raised in the laminate is increased. In this case, from  $45^\circ$  to  $30^\circ$ , the maximum difference in the temperature is 2.67%. On the contrary, when the angle

of the sonotrode is increased, the temperature raised is decreased, obtaining a 4.5% of decrement in the maximum temperature when modifying the angle from 45° to 60°.

## 9.6 Conclusions

The study of the heat generation and distribution during ultrasonic compaction process when the sonotrode is moving along the laminate has been studied.

Several considerations have been done concerning the approach of the problem, letting to treat the study as steady-state.

The development of the equations that allow the problem to be solved with the PGD has been presented. As shown in Chapter 8, these PGD equations solve the heat distribution but not the heat generation. An algorithm that solves the coupled resolution of the heat generation and the heat distribution has been developed.

The result obtained by the model is the temperature field of the composite plies when the sonotrode is moving at a certain horizontal displacement velocity. Then, a parametric study of several variables of the problem has been done.

First, the evolution of the temperature with the horizontal displacement velocity of the sonotrode has been obtained. It shows that, when the velocity is lower, the temperature obtained is higher, modifying the behavior of the curves due to the different cooling times.

Second, the amplitude of the ultrasonic vibration has been modified, obtaining little variations in the result for a variation of 30%.

Third, the frequency of the ultrasounds have been modified, obtaining values similar to those obtained when the amplitude is modified.

Finally, the angle of the sonotrode has been modified also, obtaining the higher temperature at an angle of  $30^\circ$  (just an increment of 2.67% from  $45^\circ$ ). Angles lower than  $30^\circ$  have not been tried due to the impossibility to compact the laminate with these angles (with angles lower than  $30^\circ$ , the sonotrode tip damages the laminate).

The variations of all the parameters have shown that little effect can be appreciated on the temperature field of the laminate.

The next step with this model should be to develop a test campaign in order to validate the steady-state results.

## Bibliography

- [9.1] Chinesta, F., Leygue, A., Bognet, B., Ghnatios, Ch., Poulhaon, F., Bordeu, F., Barasinski, A., Poitou, A., Chatel, S., Maison-Le-Poec, S.: *First steps towards an advanced simulation of composites manufacturing by automated tape placement*. International Journal of Material Forming. Vol 7, Issue 1, pp 81-92 (2014).

# *Chapter 10*

## *Conclusions and future developments*

The main conclusions of the Thesis and some possible future developments related with the work developed are presented next.

## 10.1 Conclusions

Usual composite manufacturing systems, especially those employed in the aeronautic industry, entail a large number of processes, most of them not being automated. For this reason, along with the long curing times usually required, the total time of the process becomes too long and the parts manufactured very expensive. As an example, an autoclave manufacturing process (which is the most employed when high mechanical properties are needed) requires cutting the plies, lying up the plies (including intermediate compaction phases with removable vacuum bags), making a definitive vacuum bag over the mould and curing of the laminate. The industry is always looking for new processes able to circumvent these problems. Several out-of-autoclave systems are also widely employed, for example hand lay-up or liquid resin infusion, but they do not achieve the mechanical properties obtained with the autoclave and are not completely automated.

The best way to reduce the costs and the process times would be to implement and automate all the steps in a single process, reducing also the curing time by using resins, e.g. acrylate resins, which can be cured almost instantaneously. This is what some new out-of-autoclave systems are seeking for, like the prototype studied in this work, developed by AIRBUS in the E-BEAM project, that implements automatic placement and curing of the layers. This prototype intends to integrate an automatic tape placement machine with a new technology curing device, which can be either the use of microwaves or an electron beam. In this way, after the process ends, the part is completely laminated and cured. To achieve a good quality in the final parts, a compaction phase subsequent to the placement of the composite plies, and previous to the curing phase, is needed, in order to substitute the vacuum bag used in the autoclave manufacturing.

An ultrasonic compactor makes the compaction phase, in this prototype. This compaction system vibrates over the laminate, transmitting the oscillatory movement to the composite plies and making them to heat up. The heating helps to

eliminate the air trapped between the plies, achieving the compaction of the laminate.

After describing the most common composite manufacturing techniques that can be found in the industry, the prototype object of this study has been described deeply.

Prior to describe the models developed, the possible compaction procedures (related to the number of uncured plies that conforms the laminate) and some experiments that have been carried out in AIRBUS related to the ultrasonic compaction are described.

The different compaction situations (related to the movements of the sonotrode) and the parameters that define these problems were posed. The main differences in these cases were the possibility of moving (dynamic compaction) or not (static compaction) the sonotrode along the laminate, in the direction where the tape is laid-up. Both compaction situations have been solved in the subsequent chapters.

In order to understand the compaction problem better, three preliminary models have been developed. The models are: a thermal model capable to obtain the thermal field when the temperature evolution is known at any part of the laminate, a curing model capable to predict the evolution of the degree of cure during the ultrasonic compaction procedure and a model to study the evolution of the viscosity with the temperature. The models have shown that the thermal properties given in the literature are good enough to solve the thermal distribution problem and that the laminate is not cured during the ultrasonic compaction. This last fact allows the heat generation problem considering the resin as a viscous fluid and neglecting possible viscoelastic behaviors to be studied.

After the compaction problem has been posed, a model capable to determine the viscous heat generation of the resin in a laminate during the ultrasonic compaction has been developed. The main hypotheses used in the development of

this heat generation model have been the plane behavior and the hydrodynamic lubrication. The first hypothesis has been assumed due to the directionality the fibres impose to the flow of the liquid resin and the second hypothesis due to the difference between the thickness of the resin layers and its length. The heat generated has been obtained as a function of the viscosity and the vertical velocities at the extremes of the resin layers (i. e., the vertical velocities of the resin layers).

In order to validate the heat generation model and to obtain the thermal field inside the laminate during the static ultrasonic compaction process, a semi-analytical model capable to estimate the heat generation and distribution during the compaction process has been developed. Prior to pose the model and to solve it, two possible assumptions of the composition of the pre-preg (difference in the number of resin and fibre layers) have been discussed. The results have shown that there is almost no difference in the election of the pre-preg model, letting to assume in next models the simplest one, i. e., the pre-preg model defined by one fibre layer and two resin layers. The evolution of the temperature given by the model has been compared with experimental results, showing that the approximation is very poor, due to the simplicity of this model.

As the semi-analytical model did not allow to validate the heat generation model, a 2D FEM model capable to solve the problem more accurately was developed. In this case, the FEM program solves the calculation of the heat distribution and the total heat. Due to the incremental nature of the solution proposed and the small time steps required to follow the ultrasonic oscillations, the resolution of the problem has been very expensive in time and computational resources, making it impossible to obtain the solution of the problem with the finest mesh and time step for a sufficiently long time of the ultrasonic excitation.

A new approach to study the heat generation and distribution during ultrasonic compaction process has been proposed. The Proper Generalized Decomposition has been chosen in order to avoid the computational difficulties. The formulation to solve the static ultrasonic compaction problem, treated as a

transient problem, with the PGD has been presented. The solution of the model has been compared with experimental values, showing a good agreement in the predictions. This comparison has also lead to validate the heat generation model.

After having validated the static ultrasonic compaction model with the PGD resolution, the solution of the dynamic ultrasonic compaction procedure has been posed. In this case, a steady-state solution has been assumed. The problem has been solved initially for one horizontal displacement velocity of the sonotrode. Then, a parametric analysis to study the influence of the compaction parameters has been carried out. The variables of the compaction that have been modified are: the horizontal displacement velocity, the amplitude of the ultrasonic wave, the frequency of the ultrasonic wave and the angle of the sonotrode with respect to the laminate. In all cases, except in the velocity, the solution has shown a low sensitivity to the parameters (it has to be noticed that, in the case of the velocity, the increment in the parameters are higher than in the other cases). In this way, the thermal field for the dynamic ultrasonic compaction has been obtained.

## 10.2 Future developments

Several possible future developments that can be done from the models and results obtained in this work are presented next.

First, a test campaign that obtains the temperature in the laminate during the dynamic ultrasonic compaction ought to be done, in order to validate this resolution.

Second, in order to achieve a solution with the FEM model, a different approach in the estimation of the heat generated could be done. It could be to study the heat generation during a cycle of the vibration (obtaining in this way the heat per time unit) and then, extending this heat along the process time (or splitting the process time in several sections in which this procedure were carried out). In this

way, the cost in time would be smaller. The result could be verified with the PGD resolution.

Finally, an interesting line of study could be to relate the models presented in this Thesis with the possibility of eliminating the air bubbles. The mechanism by which the air bubbles tend to move outside the laminate in this case is supposed to be the thermocapilarity. In this mechanism, the air bubbles immersed in a fluid with a temperature gradient tend to move to the hottest zone. An appropriate modelling of the movement the bubbles could be related with the thermal resolutions presented in this work, allowing the best configuration of the ultrasonic compaction parameters that achieves the faster air bubbles elimination to be obtained.

# *Annex I*

## *PGD transient model*

### *functions*

The evolution of the functions  $X_l(x)$ ,  $Y_l(y)$  and  $\Theta_l(t)$  with their respective coordinates obtained with the transient PGD model are shown in Figures AI.1, AI.2 and AI.3, respectively.

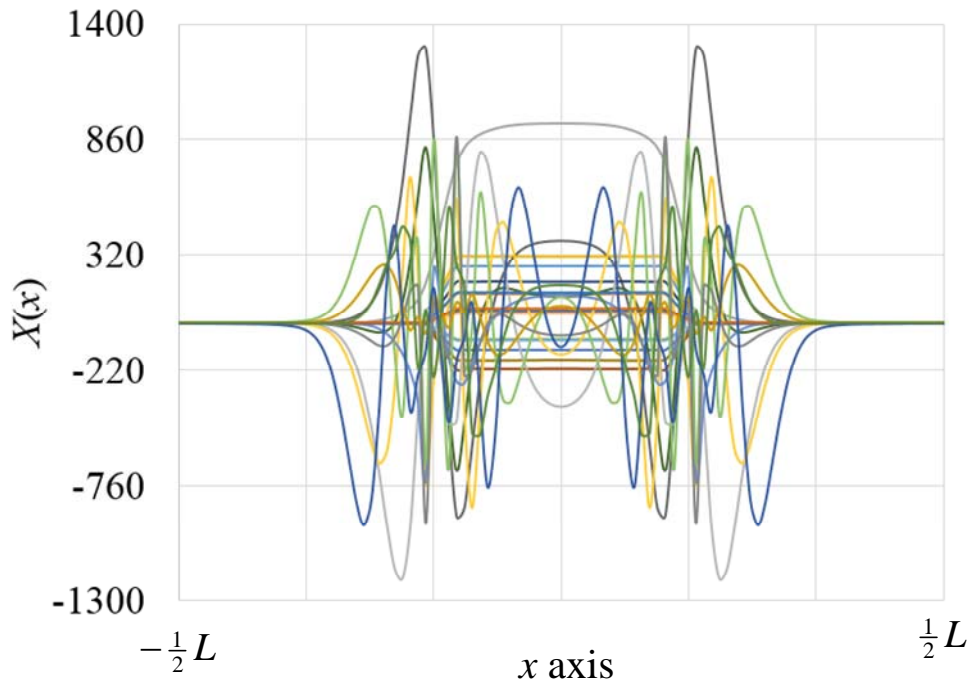


Figure AI.1. Evolution of the  $X_l(x)$  functions along the  $x$  axis

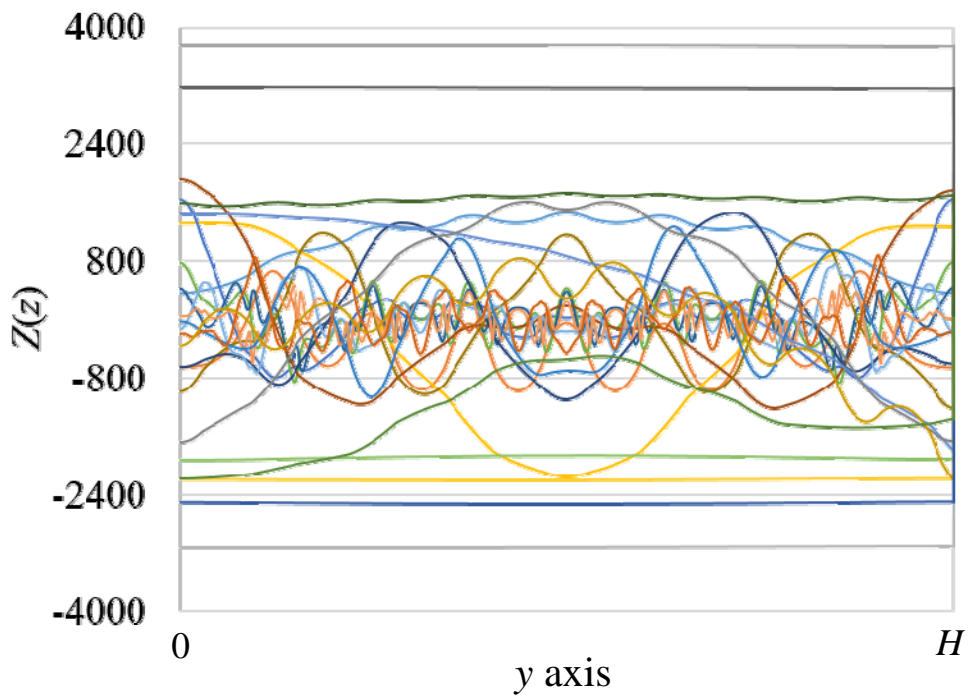
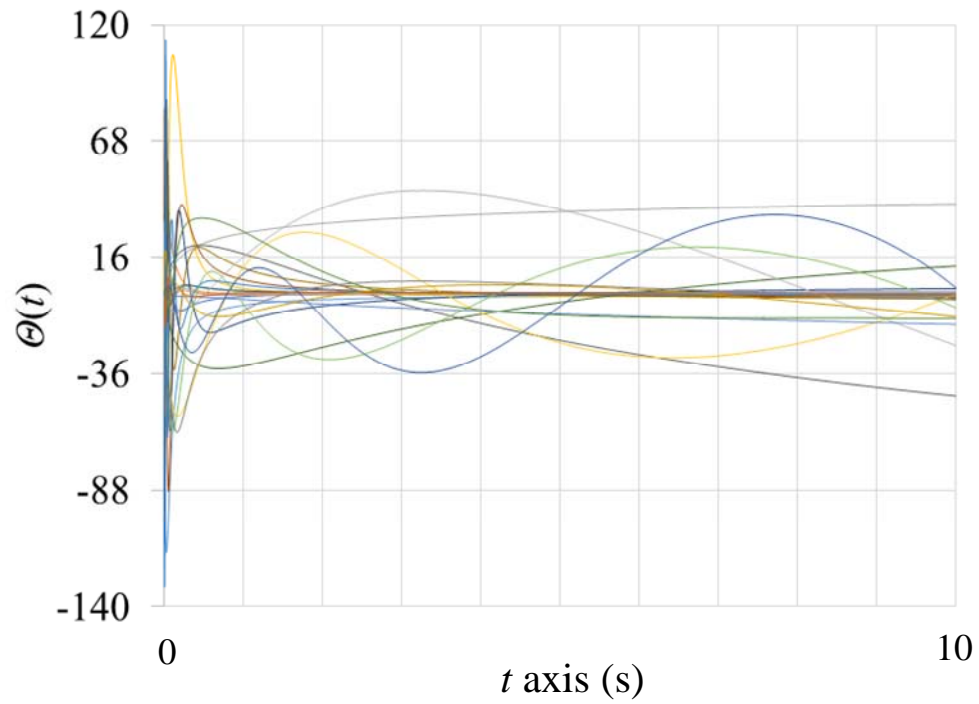


Figure AI.2. Evolution of the  $Y_l(y)$  functions along the  $y$  axis



**Figure AI.3. Evolution of the  $\Theta_i(t)$  functions along the  $t$  axis**



# *Annex II*

## *PGD steady-state model*

### *functions*

The evolution of the functions  $X_l(x)$ , and  $Y_l(y)$  with their respective coordinates obtained with the transient PGD model are shown in Figures AII.1, and AII.2, respectively.

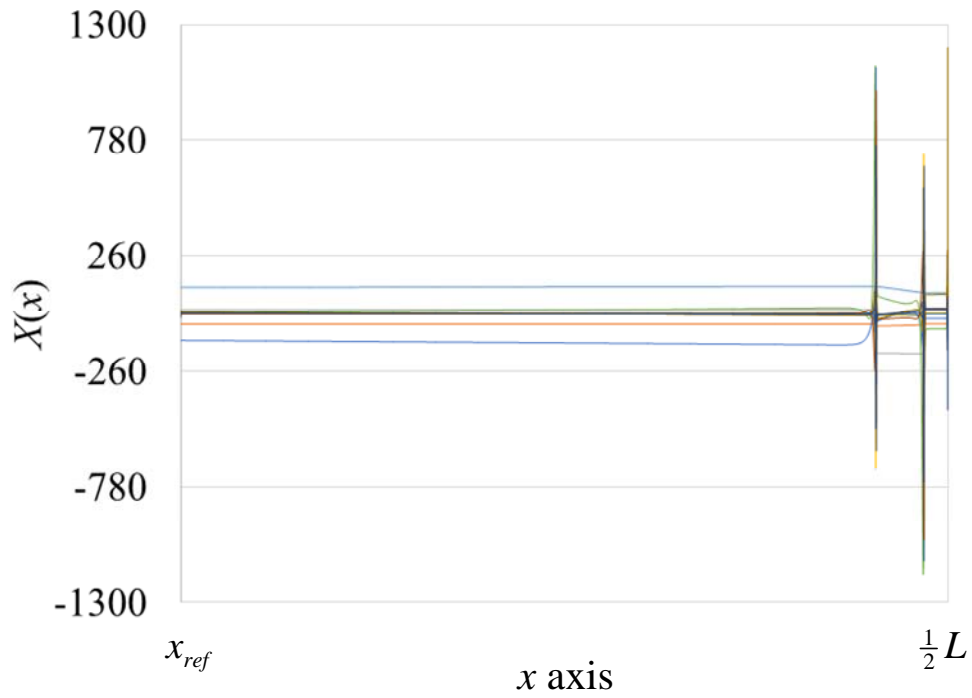


**Figure AII.1. Evolution of the  $X_l(x)$  functions along the  $x$  axis**

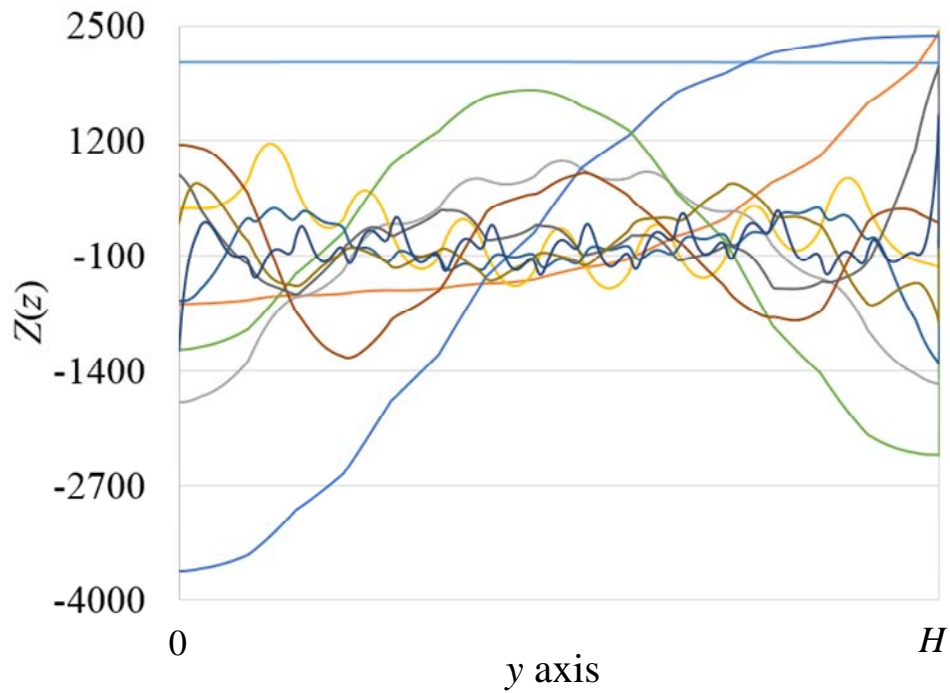


**Figure AII.2. Evolution of the  $Y_l(y)$  functions along the  $y$  axis**

# *Publications*

## **International Journal Papers**

Justo J., Graciani E., París F., Chinesta F., Ávila R.: *Study of the ultrasonic compaction process of composite laminates - Part I: Process modeling*. International Journal of Material Forming. Sent for publication.

Justo J., Chinesta F., Graciani E., Ghnatios, Ch., París F.: *Study of the ultrasonic compaction process of composite laminates - Part II: Advanced numerical simulation*. International Journal of Material Forming. Sent for publication.

## **Monograph**

Justo, J.: *Curing out of autoclave: development and modelling of an ultrasonic debulking technique*. EADS Chair of Aeronautical Studies, 2011.

## **Conference papers**

### **International**

Justo, J., Graciani, E., París, F., Ávila, R.: *Modeling of ultrasonic tape lamination*. 14th European Conference on Composite Materials, Budapest, Hungary, 2010.

Justo J., Chinesta F., Graciani E., Ghnatios, Ch., París F.: *Modeling the heat distribution of a composite laminate during ultrasonic compaction with the PGD*. 16TH EUROPEAN CONFERENCE ON COMPOSITE MATERIALS, Seville, Spain, 2014.

## **National**

Justo, J., Graciani, E., París, F., Ávila, R.: *Modeling ultrasonic debulking of tape lamination*. COMATCOMP 09, San Sebastián, Spain, 2009.

Justo, J., Graciani, E., París, F., Chinesta, F.: *Study of the heating of pre-preg layers subjected to ultrasonic vibrations*. IX Congreso Nacional de Materiales Compuestos, Gerona, Spain, 2011.

Justo J., Graciani E., París F., Ghnatios, Ch., Chinesta F.: *PGD analysis of the heating of a composite laminate during ultrasonic compaction*. X Congreso Nacional de Materiales Compuestos, Algeciras, Spain, 2013.

